The Little Galaxies That Could *Reionize the Universe*

Lauren Anderson

A dissertation
submitted in partial fulfillment of the
requirements for the degree of

Doctor of Philosophy

University of Washington

2016

Reading Committee:

Thomas R. Quinn, Chair

Matthew McQuinn

Brian Siana

Program Authorized to Offer Degree:
Astronomy

University of Washington

Abstract

The Little Galaxies That Could *Reionize the Universe*

Lauren Anderson

Chair of the Supervisory Committee:
Professor Thomas R. Quinn
Astronomy

The sources that reionized the universe are still unknown, but likely candidates are faint but numerous galaxies. In this paper we present results from running a high resolution, uniform volume simulation, the VULCAN , to predict the number densities of undetectable, faint galaxies and their escape fractions of ionizing radiation, $f_{\rm esc}$, during reionization. Our approach combines a high spatial resolution, a realistic treatment of feedback and hydro processes, a strict threshold for minimum number of resolution elements per galaxy, and a converged measurement of $f_{\rm esc}$. We calibrate our physical model using a novel approach to create realistic galaxies at $z = 0$, so the simulation is predictive at high redshifts. With this approach we can (1) robustly predict the evolution of the galaxy UV luminosity function at faint magnitudes down to $M_{\rm UV} \sim -15$, two magnitudes fainter than observations, and (2) estimate $f_{\rm esc}$ over a large range of galaxy masses based on the detailed stellar and gas distributions in resolved galaxies. We find steep faint end slopes, implying high number densities of faint galaxies, and the dependence of $f_{\rm esc}$ on the UV magnitude of a galaxy, given by the power-law: $\log f_{\rm esc} = (0.51 \pm 0.04) M_{\rm UV} + 7.3 \pm 0.8$, with the faint population having $f_{\rm esc} \sim 35\%$. The steep faint end slope is robust to realistic but significant variations in feedback, but the escape fraction measurement is more sensitive. Convolving the UV luminosity function with $f_{\rm esc}(M_{\rm UV})$, we find an ionizing emissivity that is (1) dominated by the faintest galaxies and (2) reionizes the universe at the appropriate rate, consistent with observational constraints of the ionizing emissivity and the optical depth to the decoupling

surface τ_{es}, without the need for additional sources of ionizing radiation.

TABLE OF CONTENTS

LIST OF FIGURES

Figure Number Page

LIST OF TABLES

Table Number Page

ACKNOWLEDGMENTS

It takes a village to create an Astronomy PhD and I am very grateful for my village. First, thank you to my committee Tom Quinn, Fabio Governato, Matt McQuinn, and Brian Siana for your guidance and support during my (long) journey to becoming a doctor of the stars. In particular, I would like to thank Tom for being a gentle advisor with an open door and understanding ear for any concern or issue. Thank you to the astronomy grad students for all your support and smiles in the hallway every day. Especially Yusra and Yumi for inviting me into your office for my last year. It might be the best decision I made in grad school. You guys were my rock. Thank you to all my friends for your unwavering support and confidence in me, even when I was wavering. You guys kept me smiling and were the perfect distraction when I needed it, but were also so supportive of me keeping my head down when I needed that too. Thank you to my housemates for inviting me into their comforting, warm home during my last few months in Seattle. It was a very supportive environment filled with kittens and chickens where I could comfortably give up a social life and still feel loved. Finally, thank you to my family, Dad, Kyle, Mom and Jay, for supporting me being a student my whole life.

Support for this work was partially provided by NSF award AST-1311956 and HST award AR-13264. This research is part of the Blue Waters sustained-petascale computing project, which is supported by the National Science Foundation (awards OCI-0725070 and ACI-1238993) and the state of Illinois. Blue Waters is a joint effort of the University of Illinois at Urbana-Champaign and its National Center for Supercomputing Applications. This work is also part of a PRAC allocation support by the National Science Foundation (award number OCI-1144357).

DEDICATION

To my family, near and far, for your unconditional love and support

Chapter 1

INTRODUCTION

We have a picture of the universe when it was just 400,000 years old, the residual light from recombination and what we now call the cosmic microwave background (CMB), and we have images of individual galaxies that are a billion years old, but we have very little observational evidence of the period between. The period when stars were first forming and coalescing to form the first galaxies. This high redshift frontier has been one of the most exciting areas of astronomy in the last decade due to the increasing power of our observatories. Large ground based telescopes as well as the Hubble Space Telescope have pushed this frontier beyond $z \sim 6$ to the formation of the first stars and galaxies, the objects responsible for reionizing the universe. The installation of Wide-Field Camera 3 on HST was a game changer for observing beyond $z \sim 6$ and the James Webb Space Telescope will push the frontier even farther, to observe objects forming even earlier in the universe.

The emergence of these first light sources ended the dark ages, where the universe lacked any discrete light sources, and also began the age of classical astronomy. The dark ages were initiated from the epoch of recombination, when the expansion of the universe cooled photons from the big bang to the point that they no longer interacted with the matter in the universe. Prior to recombination, the universe was a hot, dense plasma created during the big bang. The first light sources turned on when the universe was only ~ 250 Million years old, so a very long time ago. But this is also the timeframe, or redshift, that current observatories are now being able to probe.

This is also the timeframe when the intergalactic medium (IGM) became reionized. Reionization is a universal event of ionizing all the neutral hydrogen in the IGM, a global phase transition in the universe. It is an energetic event, and interesting that it happened when the universe was so young. Reionization of cosmic hydrogen between $z \sim 6-15$ (23; 11;

71) was likely caused by the first galaxies, with a significant contribution of ionizing photons coming from the faint, low mass population. Although a likely source, their contribution is difficult to quantify. The largest uncertainties in quantifying their contribution are their photon budget and the efficiency that their photons make it to the intergalactic medium (IGM). The photon budget of faint galaxies is quantified observationally through the slope of the UV luminosity function (UVLF), and the efficiency of escape is quantified by the escape fraction $f_{\rm esc}$.

Observations are starting to shed light on these uncertainties. HST surveys have constrained the faint end of the UVLF down to $M_{UV} \sim -17(-19)$ at z $\sim 4(8)$ (25; 13), but $f_{\rm esc}$ at high redshifts is a more difficult measurement. Intervening neutral hydrogen between us and a high redshift galaxy absorbs any ionizing radiation that may have escaped the host halo. In the local universe, low metallicity, high star forming galaxies are the most likely candidate for a significant $f_{\rm esc}$, but there are very few galaxies with these characteristics, so lower redshift measurements of $f_{\rm esc}$ are also difficult. Measurements have been attempted on a handful of these local galaxies and show very few ionizing photons escape their host halos (55).

Even with this progress from observations, uncertainties remain in our understanding of reionization. The faint end slope of the UVLF is a crucial parameter for quantifying the photon budget of faint galaxies. UVLFs that increase steeply at faint magnitudes (38) imply a larger role played by these numerous dwarf galaxies as a source of ionizing photons. Indeed, recent surveys point to slopes steeper than -2 at $z > 6$ and to steeper slopes at higher and higher redshifts (25). [1] Steeper UVLFs imply a large number of galaxies below the current detection limit of high redshift surveys, but it is uncertain how faint these steep UVLF can be physically extrapolated. A natural turn over in the UVLF is expected due to star formation being inefficient in low mass halos, but the UV magnitude this occurs at has not been observed and is still unknown. So extrapolating the observed faint end slope of the UVLF to magnitudes fainter than observations probe might over predict number of faint galaxies and their ionizing photon budget.

[1] At slopes steeper than -2, the galaxy number density formally diverges, however, galaxies fainter than $M_{\rm UV} > -6$ are not observed in the Local Universe.

In addition to the uncertainty in the number density of high redshift galaxies, we have very little understanding of their escape fractions as well. Our constraints on $f_{\rm esc}$ are limited by our understanding of the 3D distribution of gas and stars in high-z star forming regions. Progress is further hampered by a lack of numerical studies of high-z galaxy formation where the baryon distribution is resolved to sub-kpc scales (92; 24; 52). Resolving the gas and stellar morphology is particularly important since the distribution of gas with respect to stars affects $f_{\rm esc}$. In particular, more massive systems with disk-like configurations may have low escape fractions (93), while lower mass dwarfs, with bursty SF suggested both by observations and theoretical models (88; 48; 35; 94), drive galactic-scale outflows of gas, decreasing the cold gas covering factor and therefore possibly facilitating a higher $f_{\rm esc}$ (22).

Substantial progress could then be achieved by simulating a significant number of high-z cosmological systems spanning a range of masses, dynamical states and environments to measure $f_{\rm esc}$ and determine the faint end slope of the UVLF. These simulations would need to resolve the 3D distribution of stars and gas down to sub-kpc scales, where the properties of the ISM become important. To achieve this, we applied a SF model to a uniform volume cosmological simulation, where the morphology of galaxies down to 10^6 $M_\odot$ in stellar mass are resolved down to a nominal force resolution of ~ 350 pc. Given that the typical size of such low mass, high-z galaxies is smaller than a few kpc, this is a significant improvement compared to other recent simulations of uniform volumes (89; 77). By resolving the spatial distribution of the gas and stars on this scale, our simulation robustly captures $f_{\rm esc}$ in smaller, higher redshift galaxies than previous work. An important novelty in our approach is that the SF and feedback parameters were optimized to result in realistic z=0 galaxy models over a wide range of masses, and is described further in Tremmel+16. In addition, we studied in detail the convergence of the escape fraction calculation for our resolved systems.

1.1 Outline

Our approach combines a high spatial resolution, a realistic treatment of feedback and hydro processes, a strict threshold for minimum number of resolution elements per galaxy, and a converged measurement of $f_{\rm esc}$. With this approach we (1) *robustly predict the evolution*

of the galaxy UVLF at faint magnitudes down to $M_{\rm UV} \sim -15$ on a sample of galaxies comparable in number to HST data samples and (2) *estimate the escape fractions over a large range of galaxy masses based on the detailed spatial distribution of both the stellar and gas components.* Together, this will quantify the photon budget of faint galaxies and their contribution to reionization. The simulations methodology is described in Chapter 2, the simulated UVLF and $f_{\rm esc}$ results are presented in Chapters 3 and 4, and the consequences for reionization are discussed in Chapter 5. The effects of varying our feedback prescription on our results is described in Chapter 6. We summarize our conclusions in Chapter 7.

Chapter 2

THE SIMULATIONS

2.1 Introduction to the Vulcan

To quantify the contribution of faint galaxies to reionization we ran the Vulcan , a high resolution, uniform volume simulation in a full cosmological context to a redshift of 3.4 using the N-body Treecode + Smoothed Particle Hydrodynamics (SPH) code ChaNGa (45; 74; 62)[1]. ChaNGa includes standard physics modules previously used in Gasoline (90; 80) including a treatment of metal line cooling, self shielding, cosmic UV background (40), star formation, turbulent diffusion of metals and thermal energy, and "blastwave" Supernovae (SN) feedback (85). For self shielding, we use the method from (72) where the ionization state of the hydrogen and helium gas is determined from the cosmic UV backround using an equilibrium solver algorithm based on (47). With the ionization state determined, the attenuation of the UV field due to the H I, He I and He II ions is then calculated. This process is crude compared with radiative transfer techniques, but still important in dense environments.

[1]ChaNGa is part of the AGORA group, a research collaboration with the goal of comparing the implementation of hydrodynamics in various cosmological codes (51) on the Blue Waters machine. ChaNGa is available at http://www-hpcc.astro.washington.edu/tools/changa.html

Table 2.1: The Vulcan Simulation Numerical Parameters

N Dark	N SPH	M_{dm} [$M_\odot$]	M_{gas} [$M_\odot$]	M_* [$M_\odot$] *	Softening †	Run Time
1152^3	768^3	1.22×10^5	2.12×10^5	6.36×10^4	311 pc	10^7 CPU Hours
∗ Mass of the star particles at time of formation.						
† Gravitational softening; defined as the half-width of the spline density kernel.						

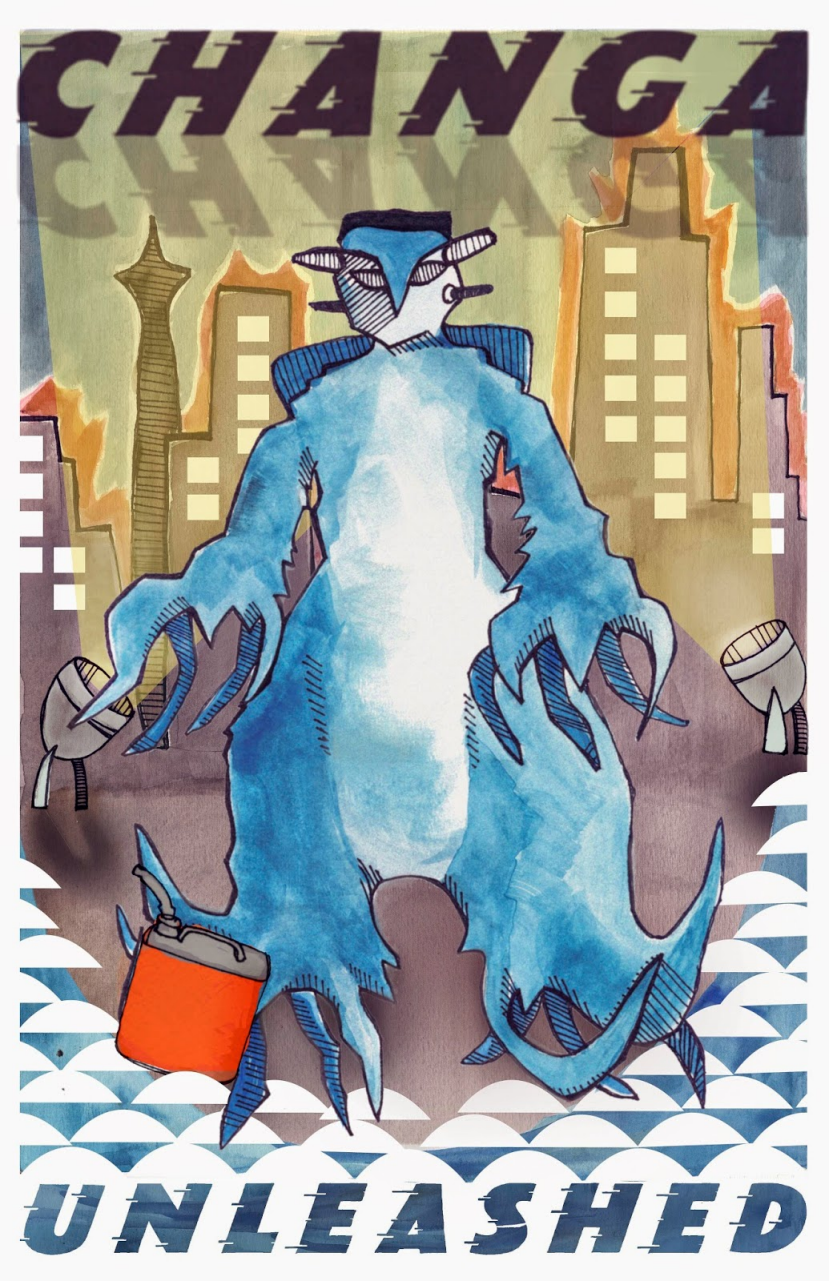

Figure 2.1: **ChaNGa: Charm Nbody Gravity Solver**: ChaNGa is a parallel N-body and Smooth Particle Hydrodynamics solver. The SPH algorithms are the same as those from Gasoline but implemented in the parallel language Charm++. This allows for large cosmological simulations to scale efficiently to over 100,000 cores on large supercomputers. Part of the power of the charm run-time system is its ability to automatically balance the load among processors by moving parts of the computation around, as visualized in Figure 2.4. ChaNGa's infrastructure enabled us to simulate a 25 Mpc box at this resolution, a challenging, highly clustered dataset.

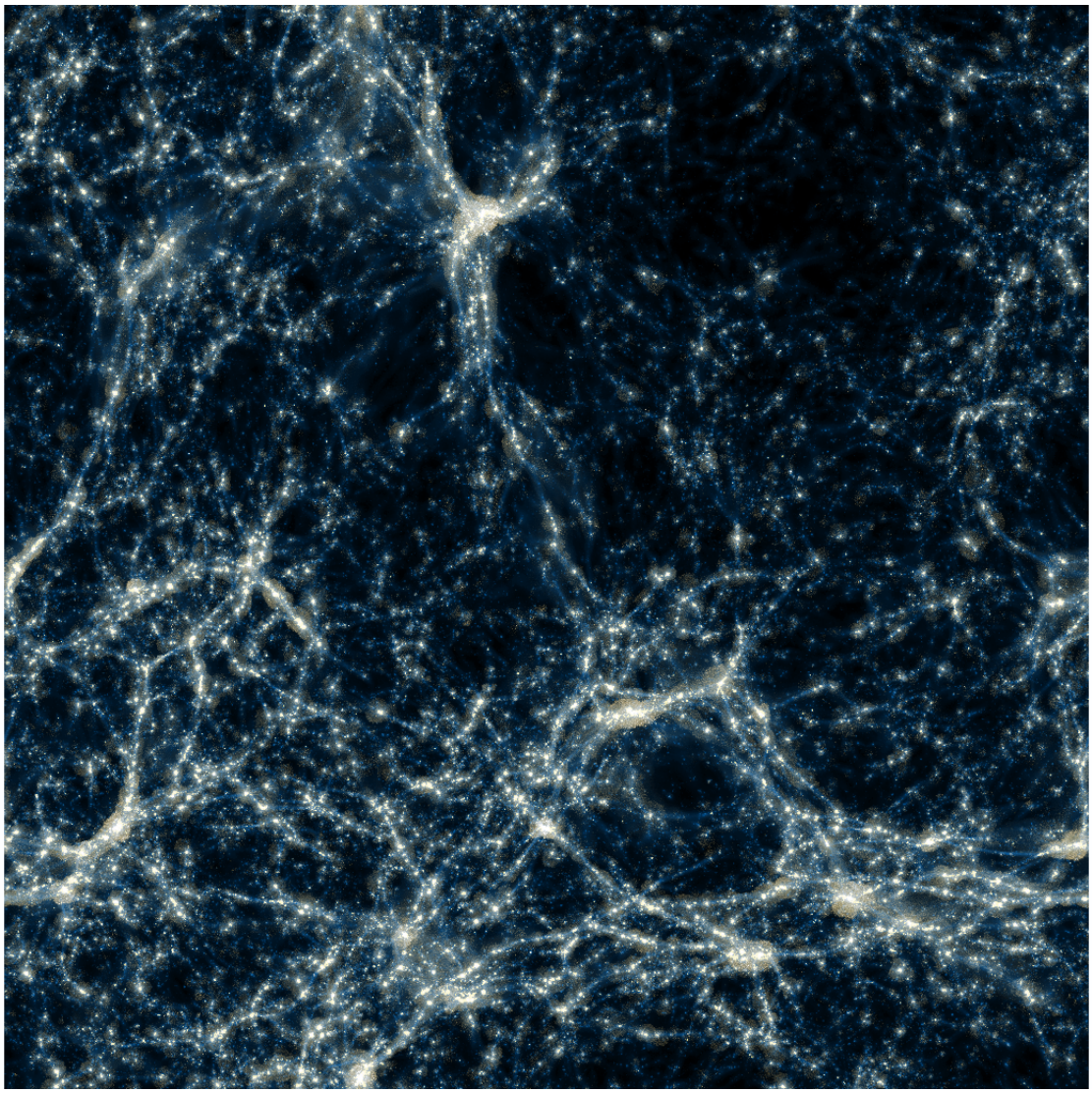

Figure 2.2: A slice of the VULCAN simulation, 25x25x10 Mpc showing the high dynamic range of the simulation at $z \sim 4$, where the blue hues are gas density, the yellow hues are gas temperature, and the white hues are young stars, less than 50 Myrs old. The gas density traces the filamentary structure of the cosmic web, and the gas temperature traces gas being heated from stellar feedback. With 350 pc resolution in a 25 Mpc box, we resolve the morphologies of ~ 100 systems down to 5×10^9 $M_\odot$ in stellar mass, of order the Large Magellanic Cloud, throughout the volume. This gives a statistical sample of lower mass halos with established escape fractions and star formation histories.

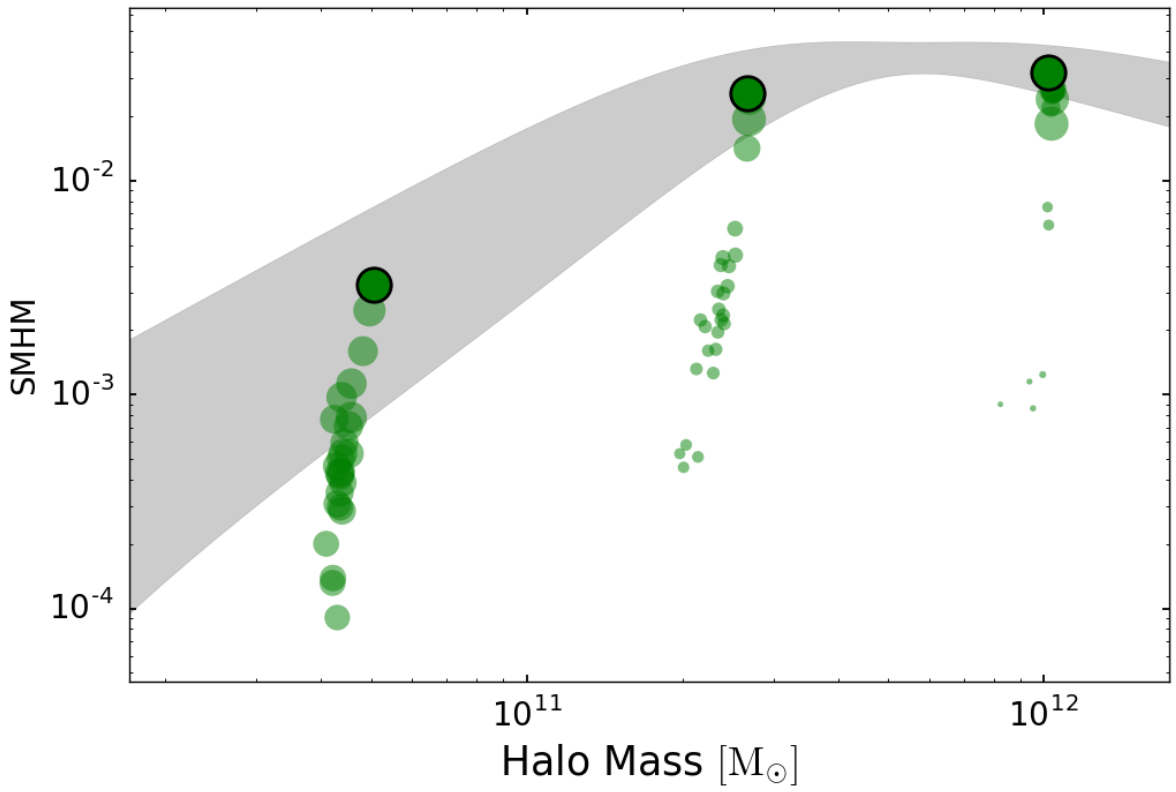

Figure 2.3: **The parameter search**: A comparison of the the observed stellar mass-halo mass (SMHM) relation with the SMHM ratio measured from zoomed-in simulations, all at z=0. The grey region represents the observed SMHM relation with its uncertainties. Each green point represents a realization of a parameter set applied to 3 zoomed in simulations of varying halo masses. The size of the point represents how well it fits **all** of our observational criteria, described further in the text. The best set is outlined in black. This parameter set simulates galaxies that match the SMHM relationship at all mass scales, as shown in this figure, and simulates galaxies that match the other observational criteria as well. We adopt this parameter set for the VULCAN simulation, which optimizes the subgrid SF parameters to create realistic galaxies at $z \sim 0$ so we are predictive at $z \sim 4 - 10$.

2.2 The Star Formation Parameter Search

We calibrated our subgrid star formation parameters to create realistic galaxies at $z = 0$. While the parameter space related to SF and feedback in Semi Analytical Models (SAM) can be rapidly explored using Bayesian techniques (9; 15), large, uniform volume simulations are limited by the small number of experiments possible. In this work we adopted a novel approach to validate our model at $z = 0$ so we can be predictive at $z \sim 4 - 10$, during reionization. We use Gaussian process regression to map out the suitability of the subgrid parameter space for our star formation prescription (Tremmel+16). In our tests we focused on three parameters:

(1) the normalization of the SF efficiency, c*, which dictates the fraction of gas that turns into stars in a dynamical time, given by the equation

$$p = \frac{m_{\rm gas}}{m_{\rm star}}(1 - e^{-c^* \delta t / t_{\rm form}}) \tag{2.1}$$

(2) the amount of energy per SN that is coupled to the ISM, dESN, and

(3) the density threshold at which cold gas is allowed to form stars, ρ_{crit}.

Each set of parameters was applied to three "zoomed-in" simulations with masses $\sim 10^{10}$, 10^{11} and 10^{12} $M_\odot$ at $z = 0$. Each run uses the same cosmology, particle mass, force softening and all numerical parameters as the VULCAN simulation described below. We then measured a number of observable properties for each galaxy and compared each set of three "zoomed-in" simulations with the observed real-world scaling relations. We used the cold gas vs stellar mass ratios, the specific stellar angular momentum vs stellar mass (5; 66), and the stellar mass/halo mass ratios (8) with the corrections to stellar and halo mass described in (64), as shown in Figure 2.3, left. The figure shows the realization of the SMHM relation in green for each simulated galaxy at $z = 0$ for all of the parameter options chosen, 20 for each halo mass. The grey band is the observed relationship and its uncertainties from (39). The black circled points represent the realization for the parameters we chose to use in the VULCAN simulation. This underlying parameter choice not only matches the observed SMHM well, as shown in Figure 2.3, left, but also matches the other observed constraints as well. Each simulated galaxy at $z = 0$ received a "grade" based on its distance from

the observed relation, and the Gaussian process algorithm penalizes parameter values that lead to simulations that deviate from the properties of real, local galaxies. It interpolates between the tested values to give robust estimates of uncertainty around parameter values we have not yet simulated. At each step we then choose our next parameter values to test based on how likely it is to turn out better than our best values so far. We then repeat the runs with the same galaxy set, but with the updated parameters, for a number of times until the parameters converge to a set of values that form the most realistic galaxies. Each galaxy was equally weighted, but we explore different choices in Tremmel+16, where dwarfs were more heavily weighted. This approach maximizes the "goodness" of our adopted star formation and feedback implementation. In practice, this approach is relatively free of human biases and superior to a standard random-walk Markov chain when only a limited number of experiments can be carried out. For example, we ran 20 sets of three simulations each.

The following parameters created the most realistic galaxies across the three mass ranges, and are the values used for the VULCAN simulation:

(1) $c^* = 0.1$,

(2) dESN= 10^{51} ergs, and

(3) $\rho_{crit} = 0.1$ amu/cc.

By using constraints from $z = 0$, rather than from high redshift, our simulations are *predictive* at high redshift, and therefore able to predict the faint end of the UVLF at high z. In addition, our simulated UVLF independently matching the observed high-z UVLF, see §3 and Figure 3.4, suggests that this method successfully maps out parameter space to find parameters that simulate realistic SFRs and metallicities of galaxies.

2.3 The Simulation Parameters

After optimizing the SF parameters, we then ran our main simulation: a uniform volume, high resolution cosmological simulation. We chose a box of 25 comoving Mpc (cMpc) to sample the smaller k modes of the matter power spectrum and get a maximally diverse sample of environments. We also wanted a high enough resolution to resolve the morphologies of low mass galaxies, and to separate the disk and spheroidal kinematic components.

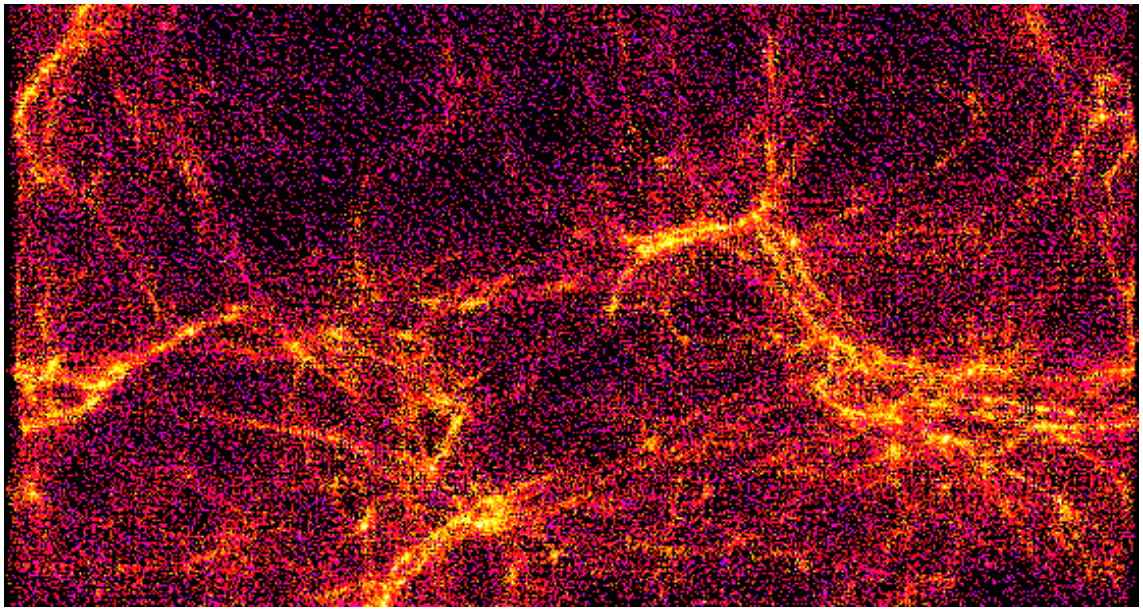

Figure 2.4: **Computational load of the Vulcan simulation**: A visualization of a 25x12x4 Mpc slice of the VULCAN simulation at $z = 3.4$, where each point shows the centroid of a virtual processor. One million virtual processors are used, each containing ~ 2000 particles. The coloring indicates the computational load associated with each virtual processor, where bright, golden pieces have an individually large load and dark, purple pieces have a small load. The load varies by a factor of 8 across the volume and is generally higher within collapsed structure, which is visualized by their bright, gold appearance. The Charm++ runtime system maps these virtual processors onto the real processors of the Blue Waters machine so that the sum of the computational load is approximately equal across all real processors, allowing this highly clustered data set to scale efficiently. With this scaling efficiency for clustered data, we can run a large, uniform cosmological simulation with a high spatial resolution to resolve the internal 3D structure of a statistical sample of faint galaxies.

With this choice of box size, however, we do not resolve the knee of the UVLF at $z > 5$, so to fit the UVLF we take the observed values as a prior to our UVLF parameter search (25), which we'll discuss more in §3.1. The starting z was 109, and we ran the simulation to $z = 3.4$. Simulating a 25 cMpc box with a spline kernel resolution of 350 pc was made possible due to the strong scaling of ChaNGa, with 50% parallel efficiency up to *128K cores*. The strong scaling is due in part to the adaptive load balancing strategies of the Charm++ run time system, visualized in Figure 2.4. In the visualization, each "particle" is a tree piece representing $\sim$ 2000 particles. The coloring indicates the computational load associated with each virtual processor, where bright, golden pieces have an individually large load and dark, purple pieces have a small load. The load varies by a factor of 8 across the volume and is generally higher within collapsed structures, which is visualized by their bright, gold appearance. The Charm++ runtime system maps these virtual processors onto the real processors of the Blue Waters machine so that the sum of the computational load is approximately equal across all real processors, allowing this highly clustered data set to scale efficiently.

We make various optimal parameter choices for the physical modules within the simulation. We assume a Kroupa 2001 IMF (53), which sets the stellar feedback and SN rates, and the density threshold for star formation (ρ_{crit} above) is 0.1 amu/cm^3. Limiting star formation to dense gas regions is a realistic approach and concentrates feedback energy to effectively regulate star formation (31; 16; 1; 50). For each SN event, 10^{51} ergs of energy ($dESN$ above) couples to the surrounding gas. This accounts for energy injected by high mass stars and the subsequent SN. Cooling shuts off in gas receiving SNe energy according to the "blastwave" approximation (85). ChaNGa uses a spline kernel gravitational softening (42) so gravity becomes Newtonian at two softening lengths. Periodic boundary conditions are handled by an Ewald summation of the 4th order multipole expansion of the mass distribution in the volume (84). The SPH implementation includes thermal and metal diffusion (80) and eliminates artificial gas surface tension through the use of a geometric density mean in the SPH force expression (76; 35; 50). The simulation took 10 million CPU hours (see Table 2.1) on Blue Waters. Halos are identified using `ROCKSTAR` (7), a phase space halo finder. Galaxy magnitudes are computed using SSP model magnitudes assum-

ing a Kroupa 2001 IMF, and reddening is estimated following observational prescriptions described in §3.1. Finally the escape fractions of individual galaxies are calculated for each system by measuring the covering fraction of HI at resolved scales, described in §3.3.

2.4 Star Formation History

The cosmic star formation rate (CSFR) is a census of stars created over time in an average patch of the universe. High redshift estimates of the CSFR are based on the integration of the observed UVLF down the faint end slope to the limiting magnitude of the survey, usually $M_{\rm UV} \sim -17$, but not to the turn over in the luminosity function where star formation becomes inefficient. The UV energy density can be converted to a SFR density because the UV light is dominated by young, recently formed stars. Dust absorbs some of the UV light and re-emits the energy in the infrared, a difficult rest wavelength to observe at high redshifts due to a lack of observatories, and therefore hard to correct for. Previous measurements assumed a fixed dust extinction at $z > 2.5$ (43). This over corrected for dust (14; 75) and therefore over predicted the UV luminosity density and CSFR. Similarly, current measurements may under predict the steepness of the faint end slope of the UVLF, or the limiting magnitude may be too shallow, and therefore miss a large population of faint galaxies. This would imply a smaller UV luminosity density and therefore under predict the CSFR. For comparison, the CSFR for the VULCAN is shown in Figure 2.5, right, represented by the black histogram, and is a census of *all* stars formed in the volume. An analytical fit to all observed measurements of the CSFR up to 2013 (6) is shown in red, with error bars representing the scatter in the accumulated measurements from the literature. The grey region represents where the fit is just an extrapolation and not constrained by any observed values, so discrepancies between theory and observations in this region are not confirmed. The additional individual, colored points represent the CSFR measured more recently than 2013, so not included in the comprehensive literature search represented by the red line. These more recent measurements include star formation from fainter galaxies as surveys probe to fainter magnitudes. In particular, (2) (the blue point) is the inferred CSFR from measuring the $z \sim 2$ UVLF to 100x dimmer galaxies than previous surveys, increasing the measured CSFR. Although not directly comparable to our simulation since it is at $z \sim 2$, it

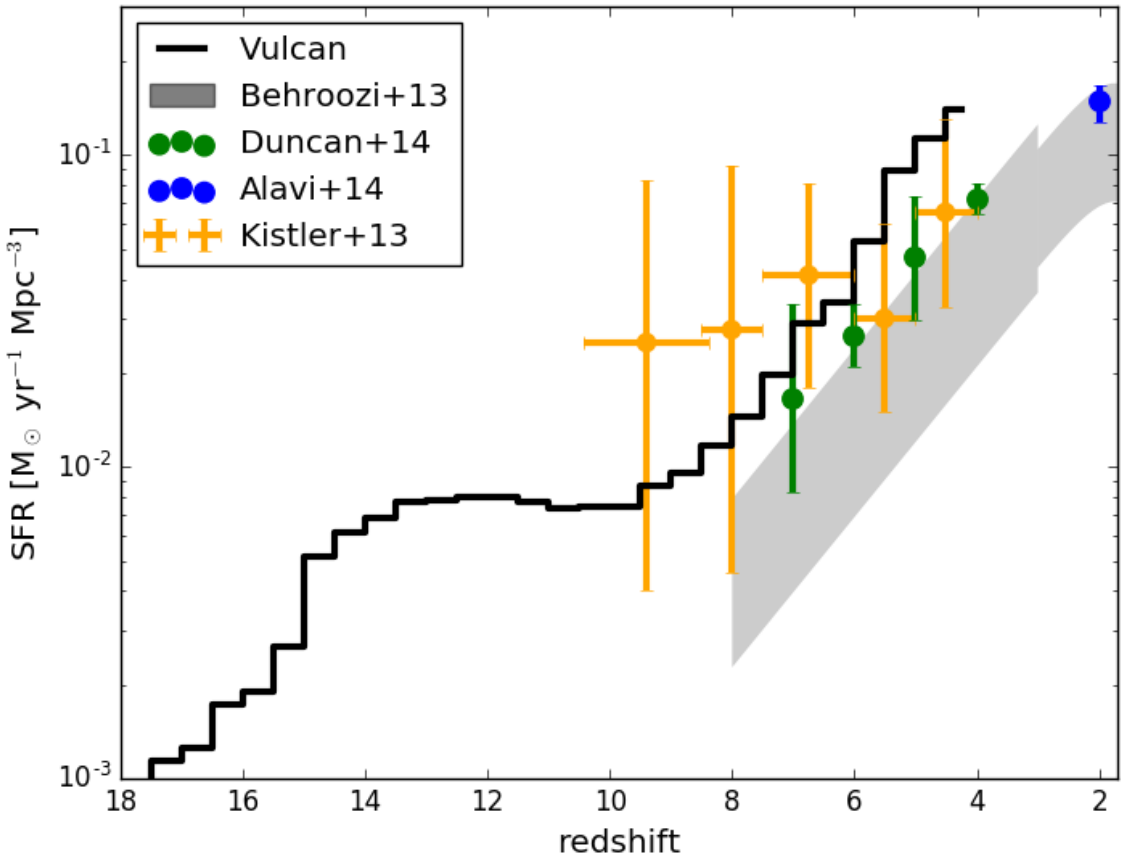

Figure 2.5: **The Vulcan Cosmic Star Formation Rate** compared with observational probes: The black line represents all stars formed in the VULCAN over cosmic time. The grey band represents an analytic fit to previous measurements of the CSFR using various observed, rest wavelengths spanning the 6 years up to 2013 (6). The width represent the intrinsic scatter in the set of measurements they extracted from the literature. The addition of more recent measurements, shown as individual colored data points, shows a trend of increasing the measured CSFR due to surveys probing to fainter galaxies. And by getting a more complete census of the CSFR, it approaches the VULCAN results, confirming that we have realistic SFRs in our simulated galaxy population.

shows the trend that having deeper photometry, and integrating farther down the UVLF, creates a more detailed picture of a higher CSFR. By including fainter galaxies and getting a better census of star formation, these measurements of the CSFR are larger than the older analytic fit, and are approaching the CSFR of the VULCAN , which includes all the stars formed, even in the faintest halos. This is initial evidence of realistic star formation rates with in each halo, and therefore realistic UVLFs. The galaxies at $z \sim 4$ in the VULCAN are also shown to match the observed sSFRs and gas metallicities of high redshift galaxies, as shown in Figure 2.6.

2.5 Romulus and HighSN

We simulated two more uniform, cosmological volumes with the same volume and resolution as the VULCAN , but with a variation of the subgrid parameters and one with the addition of black hole feedback. HighSN used the same subgrid parameters as the VULCAN , except for the SNe energy that couples to the gas: we doubled that for HighSN relative to the VULCAN . The rigorously chosen subgrid parameters for the VULCAN created the most realistic galaxies at $z = 0$ across the whole mass range explored, but the volume still over produced stars in the most massive halos. The deep potential wells of the most massive systems had an over cooling problem, where the dense gas cooled too efficiently creating more stars than we see in real galaxies. This both created unrealistic galaxies as well as significantly slowing down our code. So we did an experiment of increasing the energy deposited from supernova to see if this could solve the problem; we ran the HighSN volume.

Romulus was also the same box size and resolution as the VULCAN but included black hole physics. This is a new mechanism for feedback not implemented in previous volumes. For Romulus, the other star formation subgrid parameters were altered using the same parameter search as described above, but searching parameter space for a longer period of time. A comparison of all the simulation parameters in shown in Table 2.2. Michael Tremmel did substantial work implementing a realistic black hole physics module into ChaNGa. His implementation creates black holes in realistic locations and evolves their dynamics and feedback in a more realistic way. The model has been shown to reproduce observed star formation and black hole accretion histories, star formation efficiencies, and SMBH masses.

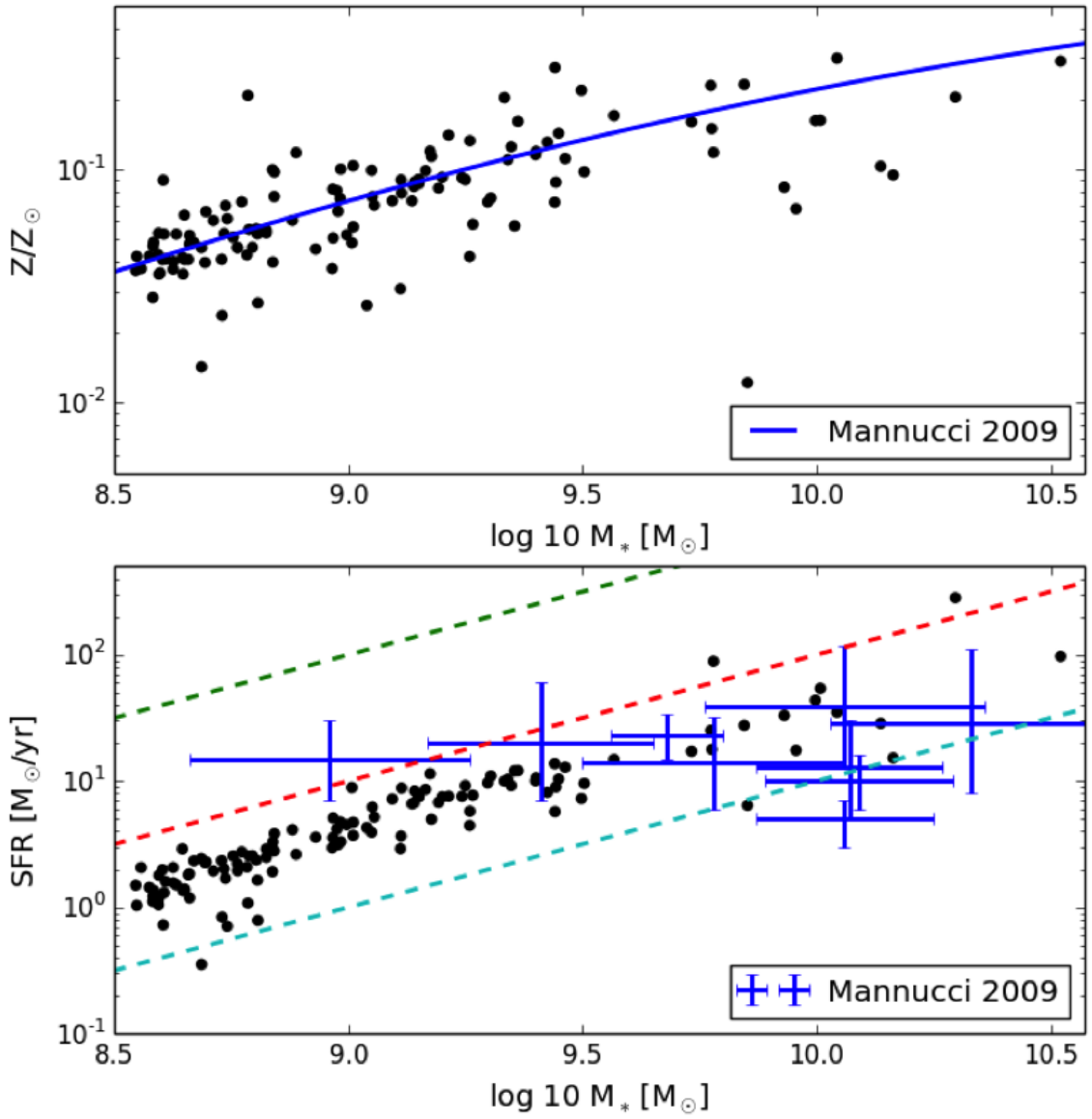

Figure 2.6: **Gas Metallicity and SFR at** $z \sim 4$: The measured gas metallicities and SFRs for the more massive systems in the Vulcan simulation to $z \sim 4$, shown as black points, compared with observed values and relations from (59) shown in blue. The gas metallicities scatter about the observed relationship, and the SFRs of the most massive systems lie within in the scatter of the observed values. The lower mass systems lie below the few observed points at these masses, possibly due to an observational bias of detecting the star bursting galaxies. The good match between observations of the gas metallicity and SFR from real galaxies and our simulation, in addition to the good match of the observed and simulated CSFR, tells us we our underlying SF prescription is forming and evolving realistic galaxies.

Table 2.2: Comparison of Simulation Numerical Parameters

Simulation	c^*	ρ_{crit} [amu/cc]	dESN [$\times 10^{51}$ ergs]	BH	Softening [pc] †	z_{final}	Run Time [CPU Hours]
Vulcan	0.1	0.1	1.0	No	311	4	10 million
HighSN	0.1	0.1	2.0	No	311	3.4	10 million
Romulus	0.15	0.2	0.75	Yes	311	1	100 million

∗ Mass of the star particles at time of formation.

† Gravitational softening; defined as the half-width of the spline density kernel.

By varying the subgrid parameters, the star formation histories of halos will change. A comparison of the volumes through their CSFR and SMHM relationship is shown in Figure 2.7 and Figure 2.8. The CSFR comparison highlights global changes in the star formation efficiencies throughout the volume, while the SMHM relationship compares the star formation efficiencies of halos as a function of their halo mass. The simulated CSFR all have similar shapes. There is an initial build up of star formation, which then drives the first galactic outflows, dampening the CSFR at $z \sim 14$, but then becomes a more regulated process with an increase in the CSFR up to $z \sim 4$ for the HighSN and Vulcan , and to $z \sim 2.5$ for Romulus, since the simulation evolved for a longer cosmic time. Where observations are available, between $z \sim 0 - 9$, there is general agreement between all the volumes and observations, shown as the colored values, and are the same as those shown in Figure 2.5. The CSFR for the HighSN volume is consistently below the CSFR for both the Vulcan and Romulus

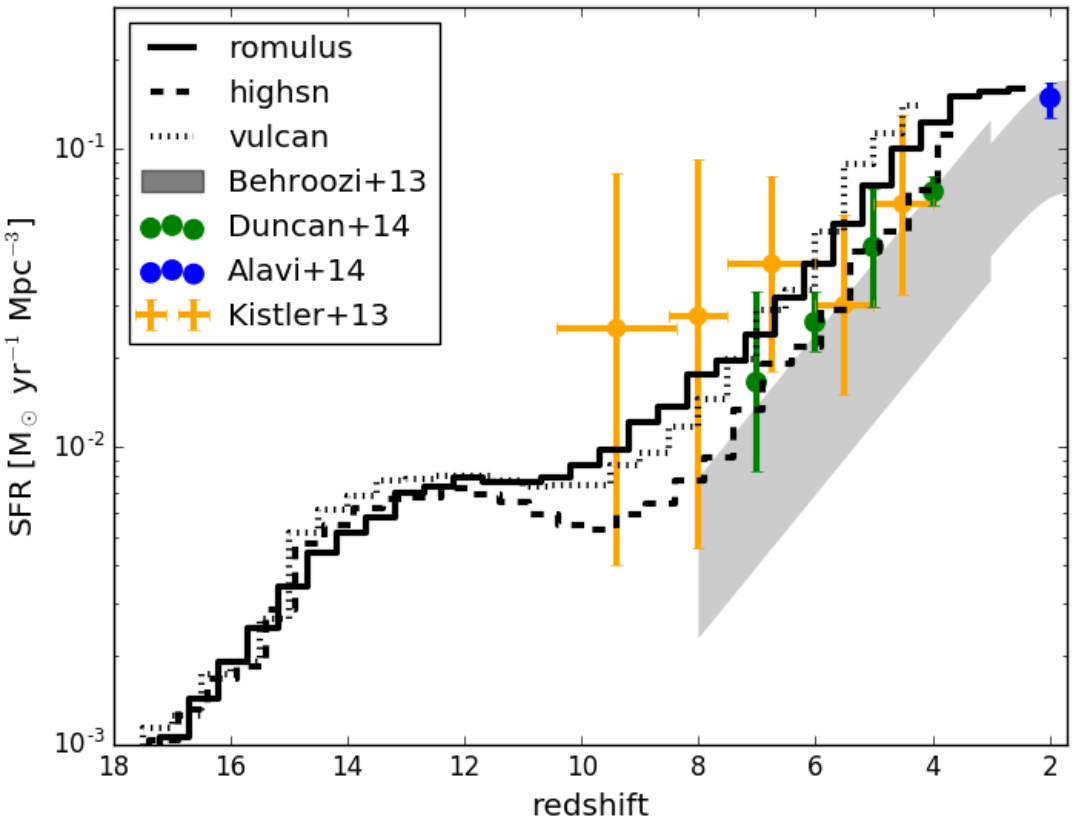

Figure 2.7: **A Comparison of the CSFR** for three similar uniform volume simulations, with the same box size and resolution, but varying the subgrid parameter choices. The Vulcan is the main simulation of my thesis, and shown as the dotted line. HighSN, shown as the dashed line, is the similar to the Vulcan but stellar feedback dumps twice as much energy into the surrounding gas. Romulus, shown as the solid line, includes black hole feedback. They all show a similar bump of star formation at $z \sim 14$ when feedback from initial stars halts star formation, but then the sfh of individual galaxies become more regulated as more stars accumulate and stochastically feedback into the surrounding gas. The effect is most severe in HighSN due to the large amount of energy dumped into the gas. Then all three simulations have a growing CSFR that is consistent with observations. The grey band is the analytic fit to the CSFR from (6) which is a fit to an accumulation of the observed CSFR from the literature up to 2013. The colored points represent measurements of the CSFR since then, and they consistently lie above the or towards the upper error bars of previous measurements, and match our simulated CSFR. HighSN lies below the Vulcan over cosmic time due to more energy from stellar feedback heating the gas in the star forming region and preventing more stars from forming.

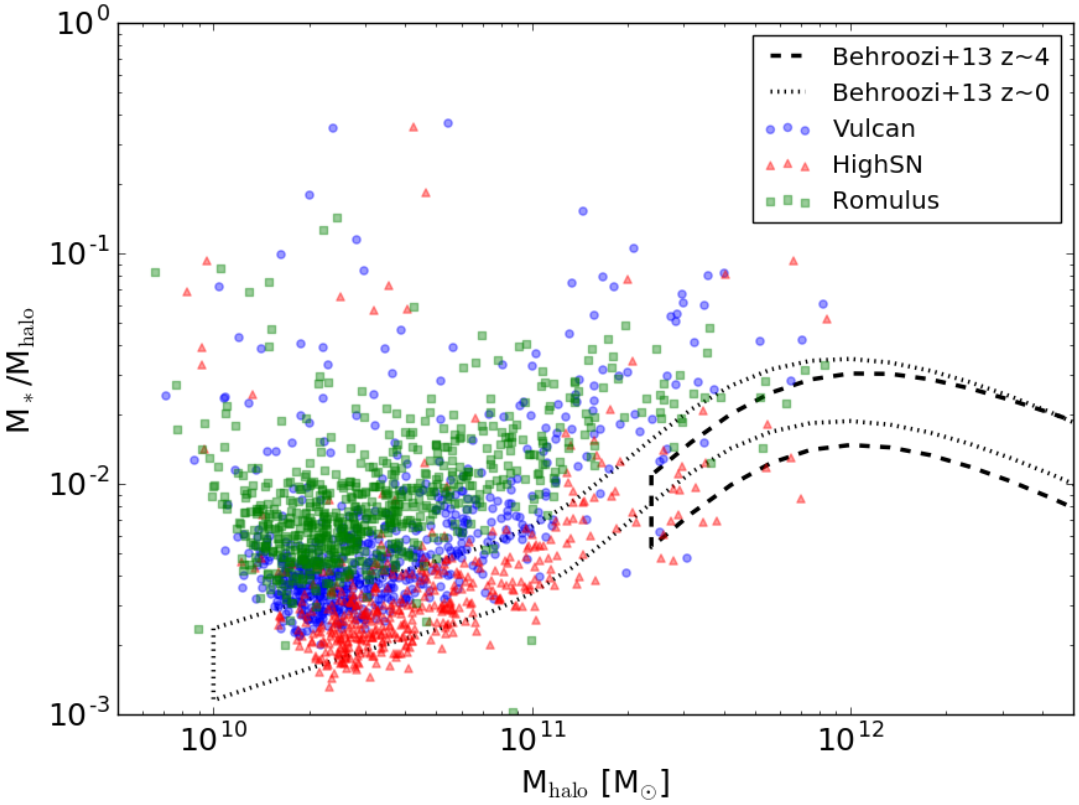

Figure 2.8: **A Comparison of the $z \sim 4$ SMHM Relationship** for the three similar uniform volume simulations. The VULCAN is the main simulation of my thesis, shown as blue circles. HighSN is similar to the VULCAN but with higher stellar feedback, and Romulus includes blackhole feedback. Comparing the VULCAN and HighSN, for a given halo mass, HighSN has a lower stellar mass. HighSN also quenches bursts of star formation creating fewer galaxies that scatter up towards high stellar masses. This quenching is seen most dramatically in the lower mass haloes, but a similar trend can be seen in the higher mass halos as well. Comparing the VULCAN and Romulus, for a given halo mass at low masses, Romulus has a higher stellar mass, though it suppresses the bursts of star formation in the higher mass halos, and of the three volumes, is the only one that consistently quenches the highest mass halos such that they agree with observations.

Chapter 3

GALAXY UVLF

3.1 Analysis of the Vulcan *Simulation*

In this section we analyze the VULCAN simulation to quantify (1) the shape of the UVLF; (2) the conversion between the UV magnitude $M_{\rm UV}$ and the ionizing photon production rate, γ_{ion}; and (3) $f_{\rm esc}$ as a function of $M_{\rm UV}$. We then use these results to quantify the contribution of faint galaxies to reionization. In section 3.1 we find the Schecter function parameters that best fit the simulated luminosity function including the effects of completeness and dust; in 3.2 we calculate the conversion of $M_{\rm UV}$ to γ_{ion} including the full SFH and stellar metallicities of a halo; and then in 3.3 we measure the escape fractions of the resolved halos, and fit a relation for $f_{\rm esc}$ as a function of $M_{\rm UV}$.

3.2 Galaxy Magnitude Calculation

To make direct comparisons with observations, we measure the rest frame magnitude of our simulated, high redshift galaxies at 1500Å, in the FUV. To calculate the intrinsic UV magnitude of each galaxy we use `Pynbody` (73), a lightweight analysis framework for N-body and hydrodynamic astrophysical simulations. The magnitude of each galaxy was calculated using the Padova Simple stellar populations (SSP) from (60; 29) [1]. The SSP model is convolved with the Galex FUV filter, centered on 1525Å with a width of 255Å, to calculate the 1500Å magnitude. Pynbody then linearly interpolates between a grid of SSP model magnitudes for various stellar ages and metallicities to the desired value for each individual star particle, and sums up the contribution of each star to the total magnitude of the galaxy. We assumed a Kroupa 2001 IMF, consistent with the assumed IMF in the VULCAN Simulation.

[1] http://stev.oapd.inaf.it/cgi-bin/cmd

3.3 Dust Attenuation

Dust is important when considering the intrinsic versus the observed amount of UV light a galaxy emits. Dust absorbs UV light, processes it, and re-emits it in the infrared. This process dims the observed UV magnitudes of galaxies. Fits to observed luminosity functions do not take this into account when the best Schecter functional fit is modeled. Observers fit directly to the observed data and correct for dust afterwards when quantifying physical quantities, such as the SFR density (82). So to do a proper comparison with observations we dim the modeled $M_{\rm UV}$ of our simulated galaxies. The effects of dust on low mass galaxies is expected to be minimal, especially at high redshift due to less accumulated metal contamination in the interstellar medium from SNe; however, an attenuation of ~ 1 magnitude is expected for the brightest systems (82). To take this into account we use observational estimates of attenuation following the formalism in (82). We direct the reader there for a more thorough description, but summarize their approach here. They use the IRX-β relation, which is the correlation of dust extinction with the UV-continuum slope, β, from (63). This is a measurement of the correlation from local starburst galaxies. They connect the UV slope β to the UVLF using the observed correlation of β with $M_{\rm UV}$ in high redshifts samples found in (14); for example, at $z = 4$, $\beta = -0.11(M_{UV,AB} + 19.5) - 2.00$. Convolving these two correlations together, they calculate an average attenuation as a function of $M_{\rm UV}$ and redshift. In future work, we will compare the observed attenuation at $z \sim 2$ to the predicted attenuation from our simulations to test if (63) at lower redshifts can be physically applied to higher redshifts.

3.4 Completeness

The uniform volume simulation is a complete sample of halos down to the resolution limit, at which point we must quantify the completeness due to resolution effects. Previous work by (19) investigated the resolution sufficient to establish galactic SFRs, SFHs, stellar feedback, and the distribution of gas and stars. They show that there is a minimum number of particles required to create realistic star formation histories (SFH), and a higher threshold for realistic morphologies. The effects of insufficient resolution can be largely grouped as

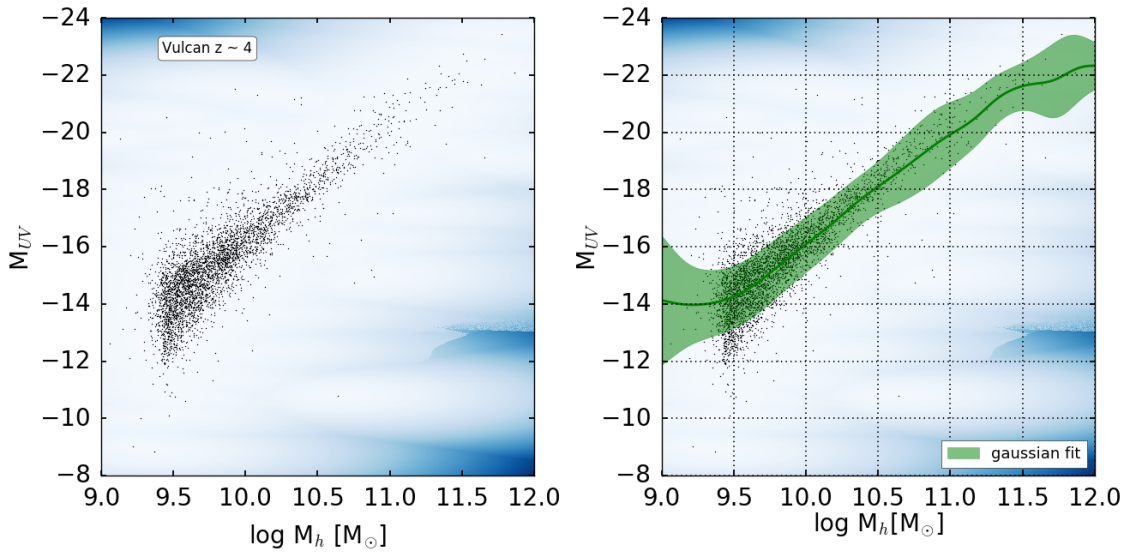

Figure 3.1: **Kernel Density Estimation at z=4**: **Left:** To calculate the completeness of our UVLF at the faint end we modeled the distribution of UV magnitudes as a function of halo mass. The individual halos are shown as black points, and the blue shading is the KDE assuming a gaussian kernel and optimizing the kernel width using the leave-one-out optimization technique. **Right:** The same underlying plot as shown on the right with the best fit gaussian in constant mass space shown in green. The gaussians are well behaved at the massive end but then diverge from the relation at low masses where our sample is incomplete due to resolution effects.

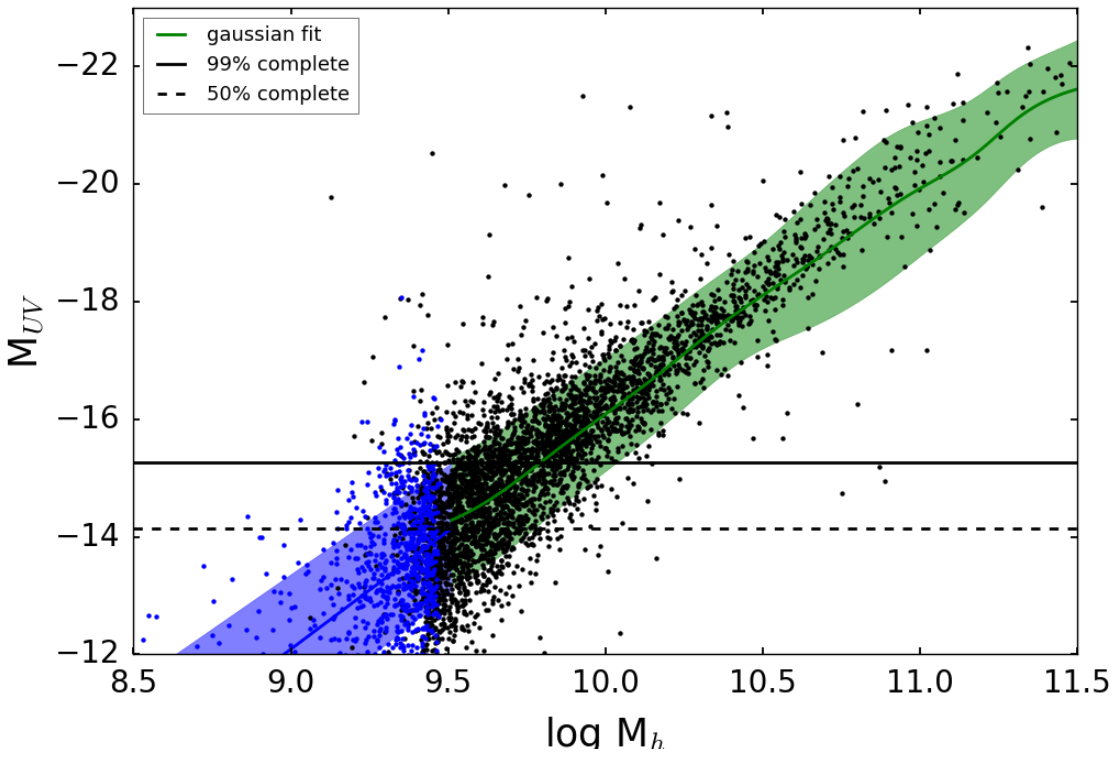

Figure 3.2: **Quantifying completeness at z=4:** The projection of the KDE to lower masses and therefore fainter galaxies to quantify the completeness of our UVLF at faint magnitudes. We fit the simulated halo masses and UV magnitudes, shown in as the black data points, with a KDE, and then fit the KDE with a series of gaussians in constant mass space, shown in green. We then project the mean and variance of the gaussians to lower masses, shown in blue, and sample those gaussians with the mass function of the simulation. The samples are shown as the blue data points. Here I only sample the mass function with galaxies that have at least 100 star particles to better visualize the projection and where the sampled data lies. The solid black line shows our 99% completeness limit, and the dashed line shows our 50% completeness limit.

those relating to overcooling (44; 83; 33), two-body heating (65; 36; 61), artificial viscosity (49; 80), and small-scale gravitational support (3). All of these contribute to unphysically altering positions of the particles and the SFR of the galaxy. Correctly determining the amount and location of SF is vital in simulated galaxies because SF produces and distributes metals throughout the galaxy, affects the distribution of matter in the galaxy through feedback, and enables us to relate simulations to observations.

In (19), they studied in detail the minimum particle count necessary to simulate realistic SFHs, important for modeling $M_{\rm UV}$. They also studied the minimum particle count necessary to simulate a realistic morphology, important for modeling $f_{\rm esc}$, which we will return to in §3.3. They showed that to simulate realistic galactic SFRs, SFHs, and stellar feedback, a galaxy needs at a minimum 10^4 dark matter particles and 10^4 SPH particles. Below this limit, global SFRs and SNe feedback are not accurate, and SFHs, gas loss and accretion are not converged. These galaxy properties are critical to simulating realistic SFH, and therefore $M_{\rm UV}$ of a galaxy, so we only calculate $M_{\rm UV}$ for halos passing this strict resolution threshold.

The shape of the faint end of the simulated UVLF is resolution dependent, and by using a strict resolution threshold our UVLF artificially turns over due to this incompleteness. To quantify the completeness of our sample we use the correlation between $M_{\rm UV}$ and halo mass. Brighter galaxies tend live in more massive halos, and the scatter in this relationship grows with decreasing mass. We fit the full distribution of $M_{\rm UV}$ of as a function of halo mass using a kernel density estimator (KDE), as shown in left panel of Figure 3.1. We sample the KDE in constant total mass space at 100 masses down to the 10^4 particle limit we set, and fit each sample with a Gaussian, shown in the right panel of Figure 3.1. The minimum particle number for a realistic SFH is high, but we trust the mass accretion of a galaxy, and therefore its halo mass, down to ~ 256 particles. We extrapolate the $\langle M_{\rm UV} \rangle$ and $\sigma_{M_{\rm UV}}$ of the Gaussians to lower halo masses, sampling the extrapolated Gaussians with the simulated halo mass function, for halos with at least 10 star particles, as shown in Figure 3.2. This cut on the number of star particles ensures we were not including dark halos with no star formation in our UVLF calculation, halos that naturally don't have any star formation. Extrapolating down the mass function is important because the spread in

magnitudes at a given mass grows with decreasing mass, so brighter, low mass halos can scatter to magnitudes brighter than $M_{\rm UV} \sim -15$, above our 50% completeness magnitude. We calculate the completeness of our sample by comparing the halos with reliable SFH to those populated by the projection, as a function of UV magnitude. For the luminosity functions presented below, we fit down to the 50% completeness level.

3.5 UVLF

Given our modeled UV magnitudes, we characterize the shape and evolution of the simulated UVLF from $z \sim 4-10$. We fit the UVLF with a Schechter function (78), which matches the observed UVLF from $z \sim 0-8$, and is therefore a well motivated functional form to fit. It is characterized by a power-law faint end slope, α, an exponential cut-off at the bright end, M^*, and a normalization ϕ^*. Specifically, ϕ^* is the Schecter function value at the magnitude M^*. The number density of galaxies at a given $M_{\rm UV}$ is given by:

$$\Phi(M_{\rm UV}) = 0.4\ln(10)\phi^* 10^{0.4(M^*-M_{\rm UV})(1+\alpha)} \exp\left[-10^{0.4(M^*-M_{\rm UV})}\right]. \tag{3.1}$$

To constrain the free parameters α, M^*, and ϕ^* we use a Bayesian probabilistic method to calculate the posterior probability distribution. We calculate the probabilities for each parameter by comparing possible Schechter models to the statistical sample of simulated UV magnitudes, and use a Markov chain Monte Carlo (MCMC) sampling algorithm (27) to sample the α and M^* parameter space. The prior on α is a top hat spanning (0, -4). The prior on M^* is the observed value since the volume does not sample the bright end to constrain this quantity; without this prior the best fit function is a power-law at higher redshifts. The posterior distributions from the MCMC sampling algorithm at $z \sim 6$ are shown in Figure 3.3. Finally, ϕ^* is then the normalization that constrains the modeled UVLF to create the same number of galaxies as the simulation. This approach allows us to determine the parameters of the UVLF without binning up the data, and therefore captures as much information as possible from each data point.

The evolution of the simulated UVLF is shown in Figure 3.4, and the evolution of the best fit Schecter parameters is shown in Figure 3.5. In Figure 3.4, the colored bands represent the simulated UVLF from $z \sim 4-10$ and the grey bands are observations (25;

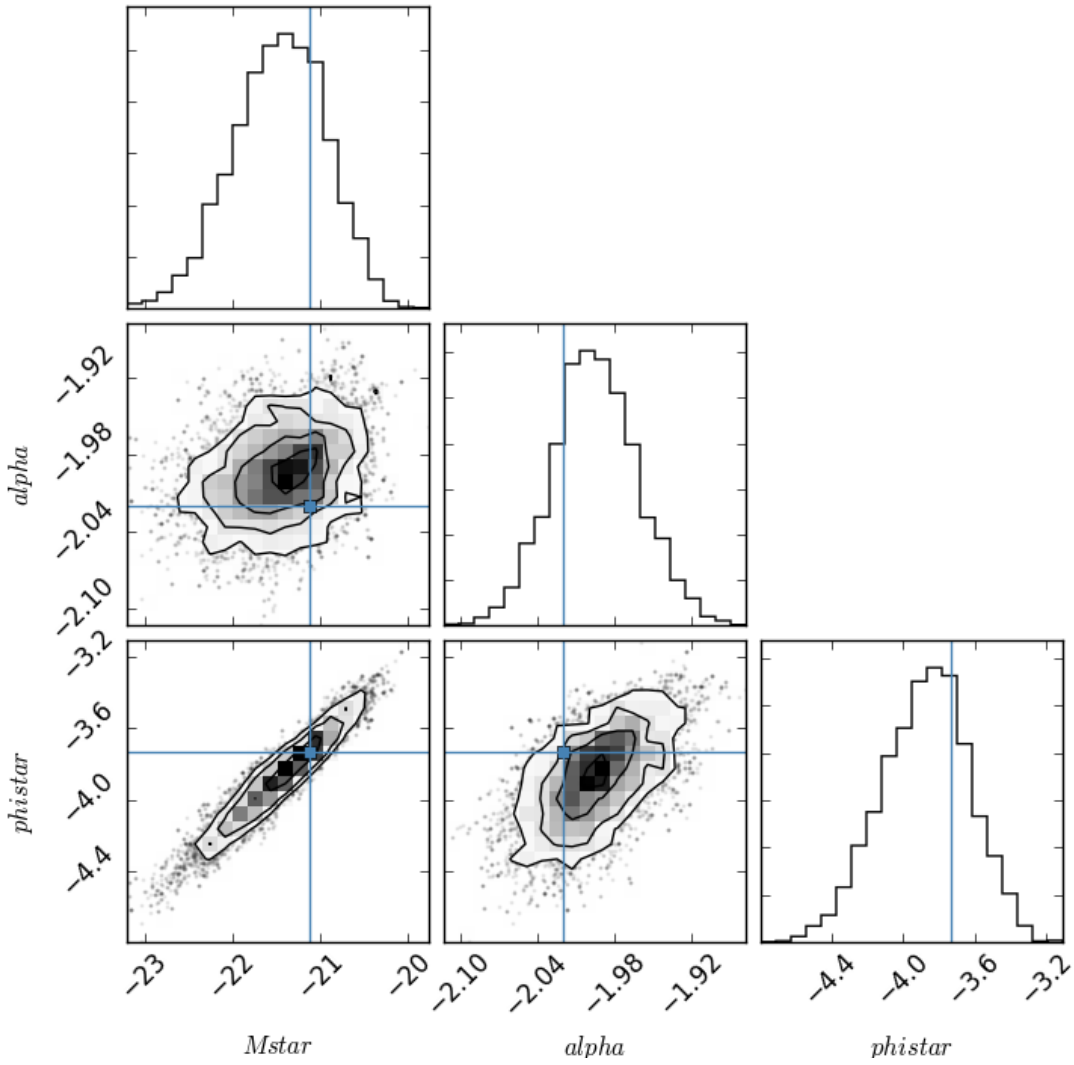

Figure 3.3: **Posteriors of UVLF parameters** from the MCMC algorithm. The contours show the distribution of the posteriors in 2D, and the histograms show the flattened mean and variance for a parameter. The blue cross represents the observed value from Finkelstein+15. The simulate parameters are consistent with the observed values.

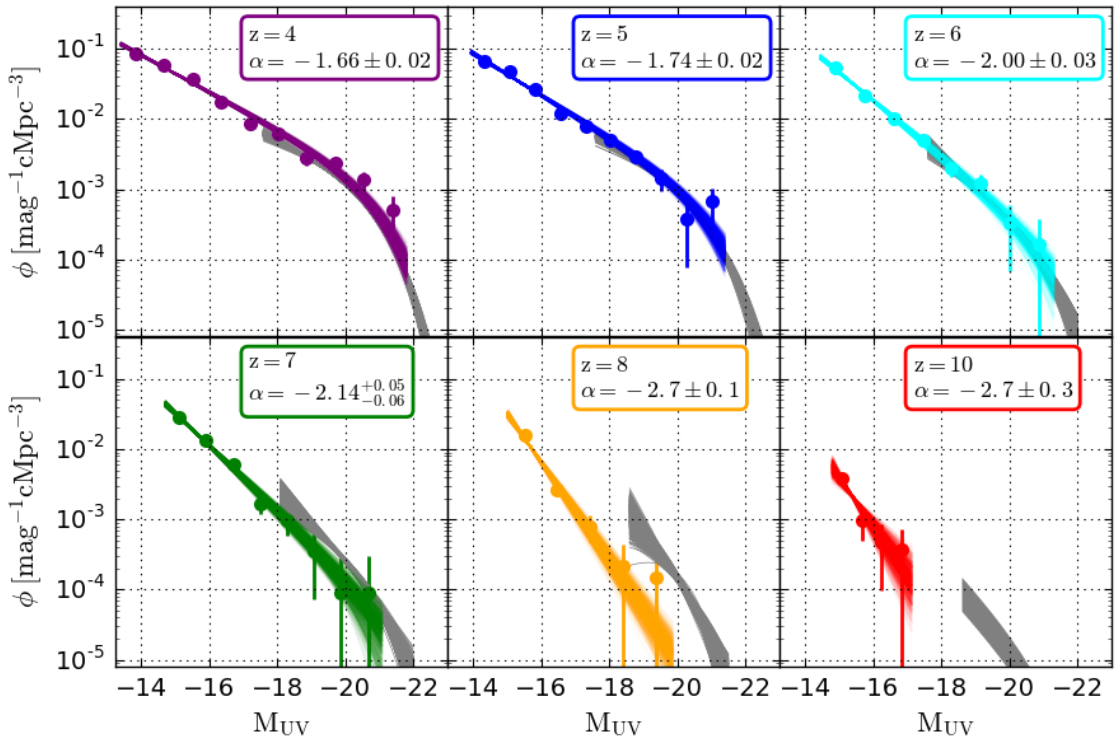

Figure 3.4: **The evolution of the Vulcan simulated UVLF** (colored data) from $z \sim 4 - 10$ compared to observations (grey bands, (25; 13)). Individual colored data points represent the binned simulated UV magnitudes with error bars representing the 1σ Poisson errors for the number of galaxies in each bin. The colored bands represent the best fit Schecter function to the simulated UV magnitudes using Bayesian inference and sampling the Schecter parameter posteriors. The simulated UVLFs match observations well at the bright end where observations are complete, and constrain the faint end ~ 2 magnitudes fainter than observations and predict steeper faint end slopes. The steeper faint end slopes are due to a higher density of faint galaxies below the current detection limits of high redshift surveys.

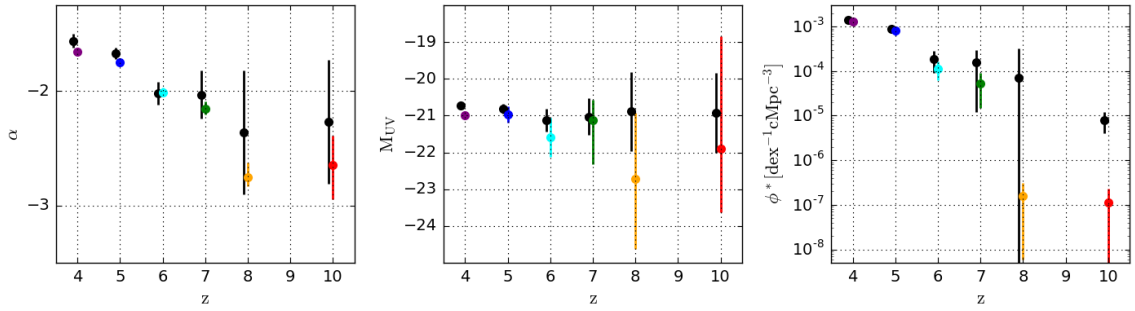

Figure 3.5: **Evolution of the Schechter parameters α, M_* and ϕ^***, in color, compared with observations, in black (25; 13), from $z \sim 4-10$. The error bars represent 1σ confidence ranges from the Bayesian inference posteriors. The faint end slope, α, is consistently steeper than observations, but within the observational uncertainties. The exponential cut off, M_*, is pushing to the brighter variance of the observations, with large uncertainties. Our large uncertainties in M_* are a reflection of our box size which does not fully sample the bright end of the luminosity function at high redshifts, and therefore also coinciding with the brightest observed value. A brighter M_* then drives the discrepancy in ϕ^*, the normalization of the UVLF. The simulated ϕ^*, agrees well with the observations except at the highest redshifts, though is still within the uncertainties at $z \sim 8$. Overall the simulation is a good match to the data, with the simulated box size dominating the errors at the bright end. The steepening of α is due to a relatively higher density of low luminosity galaxies at high redshifts.

13). Individual colored data points represent the binned simulated UV magnitudes with error bars representing the 1σ Poisson errors for the number of galaxies in each bin. The colored bands represent the best fit Schecter function to the simulated UV magnitudes using Bayesian inference and sampling the Schecter parameter posteriors. The simulated UVLFs match observations well at the bright end where observations are complete, and constrain the faint end ~ 2 magnitudes fainter than observations and predict steeper faint end slopes. The steeper faint end slopes are due to a higher density of faint galaxies below the current detection limits of high redshift surveys.

The faint end slope of the UVLF is steep at high redshift, and is steeper at earlier times, implying a population of galaxies that is dominated by the faint population at high redshifts. This is demonstrated in Figure 3.5, which shows the evolution from $z \sim 4-10$ of the Schechter parameters α, M_* and ϕ^* as the colored points, compared with observations, in black (25; 13). The error bars represent 1σ confidence ranges from the Bayesian inference posteriors. The faint end slope, α, is consistently steeper than observations, but within the observational uncertainties. The exponential cut off, M_*, is pushing to the brighter variance of the observations, with large uncertainties. Our large uncertainties in M_* are a reflection of our box size which does not fully sample the bright end of the luminosity function at high redshifts, and therefore also coinciding with the brightest observed value. A brighter M_* then drives the discrepancy in ϕ^*, since ϕ^* is the value of the Schecter function at M_*. The simulated ϕ^*, agrees well with the observations except at the highest redshifts, though is still within the uncertainties at $z \sim 8$. Overall the simulation is a good match to the data, with the simulated box size dominating the errors at the bright end. The steepening of α is due to a relatively higher density of low luminosity galaxies at high redshifts.

3.6 Conversion from $M_{\rm UV}$ to Ionizing Luminosity

Measuring the rest frame FUV magnitude of distant galaxies is significantly easier than ionizing emissivity, but the ionizing emissivity is the interesting quantity for reionization. The FUV and ionizing emissivity are both being generated by young, massive stars with well studied spectral energy disrtributions, so we can convert the FUV magnitude of a galaxy to ionizing emissivity. To calculate this conversion factor, γ_{ion}, most studies have to take

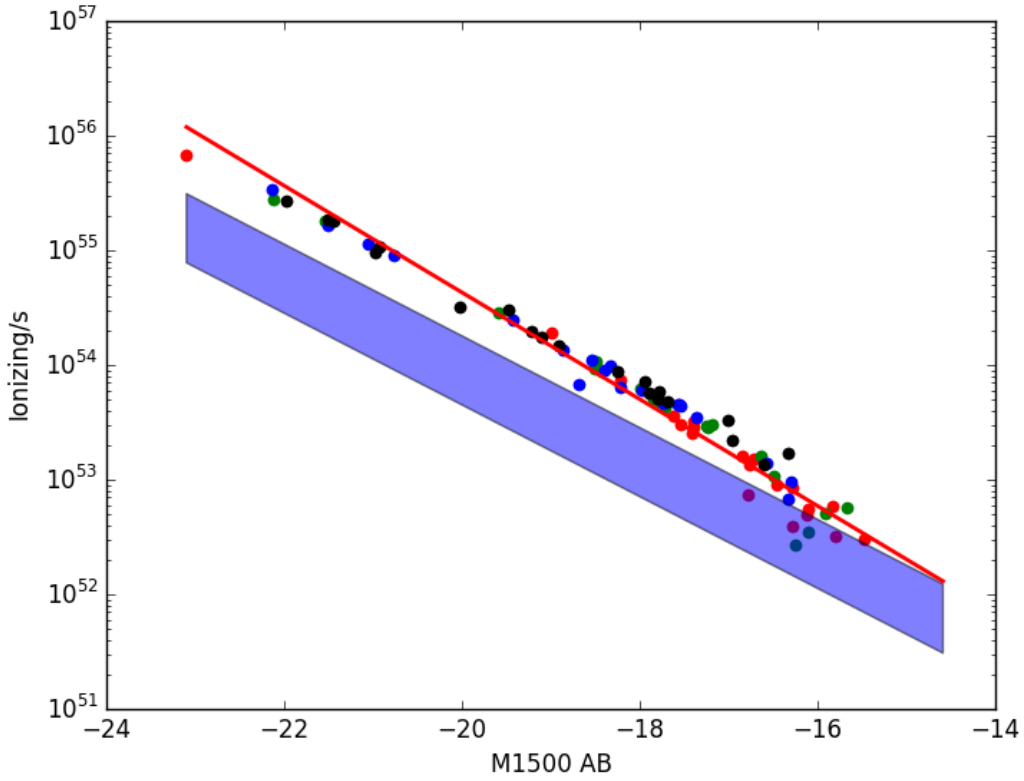

Figure 3.6: **Conversion from UV magnitude to ionizing emissivity:** The simulated conversion from a galaxies UV magnitude to an ionizing emissivity using FSPS. Individual data points resprensent galaxies from the Vulcan, with the red line being the best fit straight line. The blue shaded region represents the conversion from Kuhlen+12. We calculate the conversion using the full sfh of the galaxy and each individual metallicity of a star particle. We generate SPS models using FSPS then integrate the ionizing emissivity from 1 to 4 Ryd. There is a tight correlation due to both wavelengths of light being dominated by young, massive stars. Our relation lies slightly above previous conversions due to our full treatment of the sfh and metallicities.

the average metallicity of the galaxy and assume some shape for its SFH. Our conversion uses the mass, age and metallicity of each star in a galaxy, and therefore the true SFH of the galaxy. We calculated γ_{ion} by modeling the SEDs of a random subset of the simulated galaxies using `FSPS` (21; 20) to sum up the FUV and ionizing component from each star. From the SED, we calculated the number of ionizing photons and fit a power-law relation of ionizing emissivity as a function of $M_{\rm UV}$,

$$\log \gamma_{ion} = 45.3247 - 0.4654 M_{\rm UV}. \tag{3.2}$$

With the updated SSP models from `FSPS`, and taking the true SFH of each galaxy into account, brighter galaxies have higher ionizing emissivities compared with previous conversions which use a simple power-law SED model (54). Our ionizing emissivity is dominated by dimmer galaxies, so this does not have a significant effect for this study, but taking the full SFH and metallicity into account is important.

Chapter 4

ESCAPE FRACTION

4.1 Introduction

Escape fractions of high redshift galaxies, which possibly drive reionization, are still very unknown. High redshift measurements of $f_{\rm esc}$ are impossible due to the high optical depth of intergalactic neutral hydrogen between us and the sources, so any escaping ionizing radiation would be absorbed before reaching us. Measurements of $f_{\rm esc}$ for lower redshift galaxies are small, ranging from 1%-10%, and most observations are just upper limits. (56; 10; 41; 37). Low $f_{\rm esc}$ values are troubling for models trying to form a consistent view of reionization since the UV luminosity density, and therefore intrinsic ionizing emissivity, decreases at high redshifts. In order for the decreasing galaxy ionizing emissivity to have enough escaping radiation to reionize the universe, galaxies at high redshift must have had higher $f_{\rm esc}$ values. So even though local, observed values for escape fractions are low and high redshift values are uncertain, most reionization models must paint high escape fractions uniformly onto all galaxies, a common value being ($\sim 30\%$) at high redshifts (25; 40). Some models also allow for a variation in redshift(40), where higher redshift galaxies have higher $f_{\rm esc}$.

Reionization models with high escape fractions for all galaxies might seem ambitious, but there are very few constraints on $f_{\rm esc}$ for fainter galaxies. These galaxies do not have much star formation individually, but as a population they can contribute significantly to reionization, especially if they have higher escape fractions. One line of reasoning for them having a higher $f_{\rm esc}$ than their local, more massive counterparts is that fainter, low mass halos are characterized by bursty SFHs (87; 48; 91; 34) and shallower potential wells. Star formation events, and its proceeding SN ejecta, are contained within bursts and can therefore disrupt the gas distributions in fainter galaxies more easily and create a smaller covering fraction of neutral hydrogen. So it is encouraging that faint galaxies may have a higher $f_{\rm esc}$ because the faint end slope of the luminosity function is steeper in the early

universe, implying a higher density of these faint, but possibly potent, galaxies at higher redshifts.

To help constrain the contribution of galaxies to reionization, we measure $f_{\rm esc}$ for the resolved galaxies in our simulation. Modeling $f_{\rm esc}$ in simulations is highly dependent on the distribution of gas relative to stars, as well as a the SFH. To properly model these properties we use the resolution threshold of 10^5 dark matter and 10^5 sph particles to determine that a galaxy has a realistic 3D distribution of gas and stars, as studied in detail in (19) and discussed previously in §3.1. For our SFHs, we have a realistic star formation + feedback model (28) where bursts are regulated by feedback and accretion rates, and create the observed fraction of stars in bursts. This results in galaxies with photometric and kinematic properties comparable with real galaxies (32; 68; 18; 46; 17), where (32) and (17) analyzed simulations at the same resolution as the VULCAN . These physical properties all contribute to simulating realistic SFH and therefore escape fractions.

4.2 The Calculation

To calculate the escape fraction of ionizing photons from each galaxy, we project the neutral hydrogen column density out to the virial radius and onto the 2D sky of each star particle younger than 50 Myr old in a given halo. Previous results have used radiative transfer post processing to simulate the effect of ionizing emission on the neutral hydrogen within a galaxy. To account for local radiative transfer effects that our simulation does not include, we cut out 350 pc HII regions around each star particle that is younger than 10 Myr old. Including HII regions accounts for the radiation effects at a given time but does not self consistently evolve the ionizing radiation field. To calculate the size of an HII region around a star particle, we accumulated the sizes of individual HII regions around the O and B stars contained in a star particle, or stellar population. Each star particle can be thought of as a stellar population because we apply an IMF to each star particle to determine physical characteristics, such as SN rates or HII region size. The initial mass of a star particle is $6.46 \times 10^4\ M_\odot$, and assuming a Kroupa 2001 IMF, each star particle represents ~ 40 O stars and ~ 150 B stars. In comparison, a Salpeter IMF would create ~ 25 O stars and ~ 100 B stars. Assuming an O star has an HII region of ~ 100 pc and B stars have HII

regions of $\sim$ 10 pc (86), this averages to a star particle HII region of $\sim$ 350 pc, just at our resolution limit. Assuming a Salpeter IMF, with fewer O and B stars, would lead to smaller HII regions.

Our tests show that the escape fraction is not sensitive to HII region size. We measured $f_{\rm esc}$ varying the HII region size from 0-750 pc and saw very little difference in $f_{\rm esc}$ across this range. The HII regions make very little difference in $f_{\rm esc}$ because HII regions are most potent in central, dense parts of the galaxy where many star particles are forming, and therefore the HII regions accumulate. In these dense regions the escape fraction is so low, due to the high column densities of neutral hydrogen, that the escape fractions of star particles change from $\sim 10^{-8}$ to $\sim 10^{-5}$, and therefore have no measurable effect of increasing the escape fraction. For young stellar populations closer to the edges of the faint galaxies, where stellar and gas densities are low, HII regions are not very effective either because there is not a clustering of stellar particles for HII regions to accumulate. For stellar populations closer to the edges of faint galaxies, after $\sim$ 10 Myrs, when SNe have gone off, the stellar populations blister to the surface and dramatically increase the escape fraction, regardless of HII region size.

In contrast, the escape fraction is more sensitive to the stellar age threshold for stars included in the $f_{\rm esc}$ calculation. We measured $f_{\rm esc}$ varying the age threshold for stars included in the calculation from 10-50 Myrs old and saw a more noticeable difference in $f_{\rm esc}$. Only including stars younger than 10 Myrs old decreases $f_{\rm esc}$ by more than an order of magnitude, compared with including 25 Myr old or 50 Myr old populations, similar to results seen in (58). The youngest stellar populations have very high ionizing emissivities, but very low $f_{\rm esc}$ because they are still embedded in their birth cloud. In comparison, a 25 Myr old stellar populations has an ionizing emissivity that is 10x lower compared with a 10 Myr old stellar population, but in our simulations, on average, the 25 Myr old stellar populations have a escape fraction that are $\sim$ 30 times higher, especially at high redshifts, making them a more potent contributor to escaping ionizing radiation. Similarly, a 50 Myr old stellar population has an escape fraction comparable to the 25 Myr old stellar population, on average, but an ionizing emissivity that is 10x lower than the 25 Myr old population. So, for our calculation, we chose a threshold of 50 Myrs old.

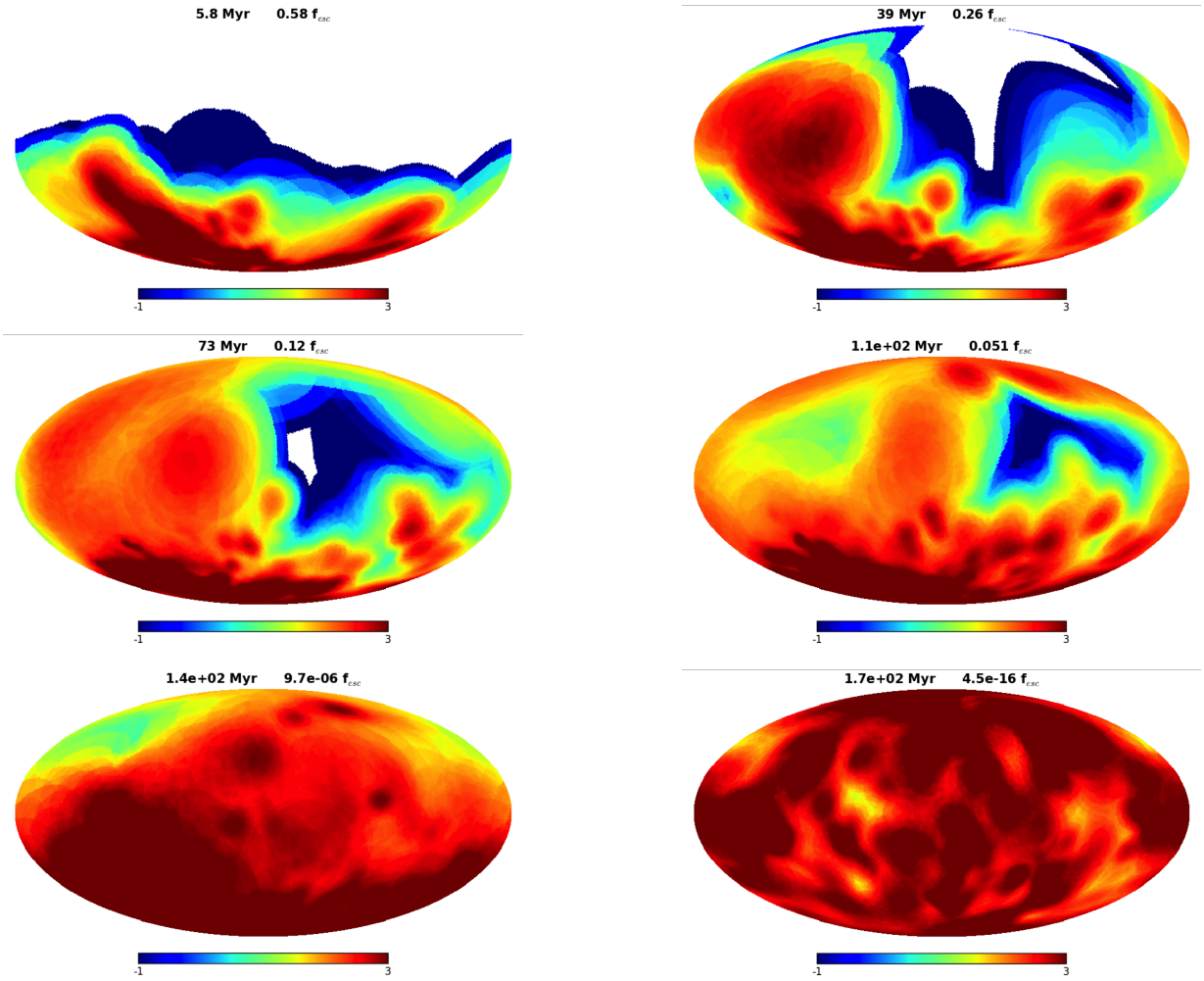

Figure 4.1: **The sky of a star particle over time**: The optical depth integrated out to the virial radius from the position of a star particle in a galaxy. The color represents the logarithm of the optical depth, with red having a very high optical depth, so no ionizing photons propagating in that direction reach the IGM, and white having an optical depth of zero, so all ionizing photons propagating in that direction reach the IGM. The age and $f_{\rm esc}$ of the stellar population is shown as well. This star particle has a particularly high $f_{\rm esc}$ due it's location within the galaxy; it is lying towards the edge of the HI distribution. After 6 Myrs supernova from the stellar population deposit energy into the surrounding gas blowing a hole in the neutral hydrogen distribution and significantly increasing $f_{\rm esc}$, then after 10s Myrs the star particle is dynamically enshrouded by neighboring neutral hydrogen again.

The measured escape fraction for our simulated galaxies is the average open sky fraction of all young star particles in a halo, given by

$$\tau(\theta,\phi) = \int_0^R n_H(r,\theta,\phi)\sigma_{H,912\mathring{A}} dr \tag{4.1a}$$

$$f_{\rm esc} = \left\langle \frac{1}{4\pi} \int e^{-\tau(\theta,\phi)} d\Omega \right\rangle_{N_*} \tag{4.1b}$$

where τ is the optical depth to ionizing radiation, $n_H(r,\theta,\phi)$ is the neutral hydrogen number density within a halo, and $\sigma_{H,912\mathring{A}}$ is the cross section for hydrogen absorption at 912 Å where absorption is strongest. Equation 4.1a, the integral for τ, is the neutral hydrogen column density out to R, the virial radius, for a stellar particle. In equation 4.1b, the $\exp[-\tau]$ is the probability of an ionizing photon reaching the IGM along a given line of sight. Integrating this probability over the sky, $d\Omega$, gives the average open sky fraction for an individual young star particle. This is visualized in Figure 4.1 which shows the projected optical depth to the virial radius for 2 different star particles in the simulation. We then take the average open sky fraction of all young stars in the halo, N_*, represented by the average brackets. This represents $f_{\rm esc}$ for a halo, and our simulated measurements are shown in Figure 4.3 as a function of $M_{\rm UV}$.

A significant deficiency in this calculation, and something to include in future work, is that all star particles younger than 50 Myrs old are equally weighted in the escape fraction calculation. However, as Figure 4.5 below shows, there is a significant drop in the intrinsic number of ionizing photons a stellar population emits as it ages. So younger stellar populations are emitting more ionizing photons but are likely to have significantly lower escape fractions, as shown in Figure 4.2. Similarly, older stellar populations, greater than 10 Myrs, are likely to have higher escape fractions due to supernova injecting energy into the surrounding gas and changing its environment, but those stellar populations are emitting significantly fewer ionizing photons.

The escape fraction for each halo is dominated by a few star forming regions having very high escape fractions, while most stars are completely opaque to the HI distribution within

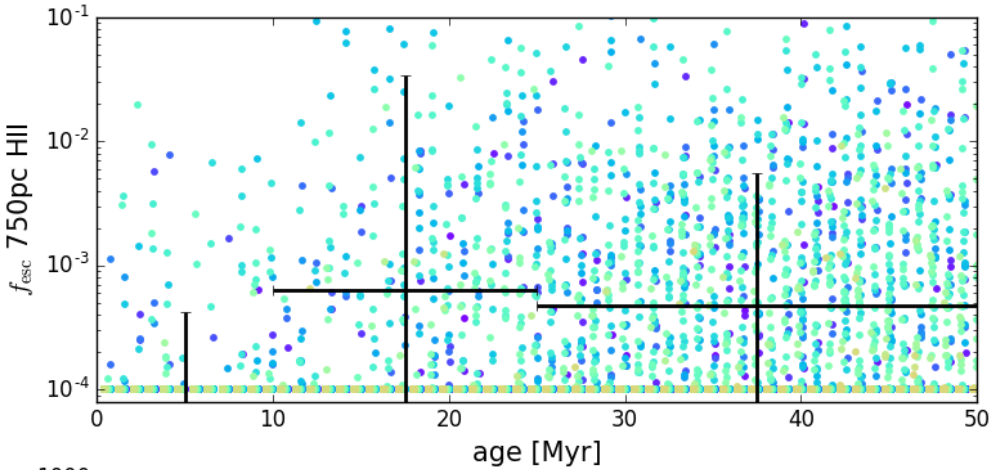

Figure 4.2: $f_{\rm esc}$ **as a function of Age:** The escape fractions of individual stellar populations as a function of age. Each point represents a single stellar population and the black points with error bars is the average for that age bin. Young stellar populations have very low escape fractions, before any supernova have changed their environment, but after 10 Myrs the escape fractions significantly increases, by 3 orders of magnitude, due to the injection of energy by the supernova associated with the stellar population.

a galaxy and have an escape fraction of nearly zero. The high $f_{\rm esc}$ values for individual stellar populations is due to the star particle sitting on the outskirts of the HI distribution of the galaxy. These stellar populations will go through episodes of high $f_{\rm esc}$ after stellar feedback (i.e. SNe) disrupts the surrounding gas distribution and the stellar population blisters to the surface. Then after 10s of millions of years the stellar population becomes dynamically enshrouded by neighboring gas, and $f_{\rm esc}$ for that star particle drops to a low value again. The blistering of stellar populations is more likely in bursts of star formation, so less bursty galaxies, as well as less bursty star formation prescriptions, will have a lower $f_{\rm esc}$. Our star formation prescription has been shown to be bursty, especially in dwarf galaxies (28), consistent with real galaxies (48), and consistent with our fainter galaxies having a higher $f_{\rm esc}$. The central, dense regions of galaxies containing cold, molecular gas is currently difficult to realistically simulate at all resolutions, but we have shown that our star formation prescription creates realistic lower density, warm and hot ISM (36; 67). So we simulate a realistic ISM where the escape fractions are measurable and significant.

4.3 $f_{\rm esc}$ *as a Function of* $M_{\rm UV}$

To encapsulate the escape fractions in the total ionizing budget from galaxies, we fit the trend of our simulated $f_{\rm esc}$ as a function of $M_{\rm UV}$ for each halo. In this form we can convolve it with the UVLF to calculate the ionizing photon budget from galaxies. Figure 4.3 shows our measured values of both $f_{\rm esc}$ and $M_{\rm UV}$ for the resolved halos in our simulation, spanning $z \sim 4-8$. At $z \sim 10$, none of the halos have passed our resolution threshold. Faint galaxies tend to have higher escape fractions, $f_{\rm esc} > 1\%$, than brighter galaxies, though the brighter galaxies have more scatter. The smaller scatter for faint galaxies relative to the brighter galaxies may be due to fewer faint galaxies passing our resolution threshold, but not many bright galaxies have $f_{\rm esc} > 0.1\%$. The blue points are observed $f_{\rm esc}$ values from local galaxies, and the red points are observed upper limits from local galaxies (55, and citations therein,Choi+16 in prep). The observed galaxies also show a large scatter in $f_{\rm esc}$. These galaxies with measurable escape fractions were targeted for their high specific SFR and therefore likely to have a measurable, and high, escape fraction. Our simulated, brighter halos scatter up to $\sim 1\%$, but most lie below the observed, upper limit constraints.

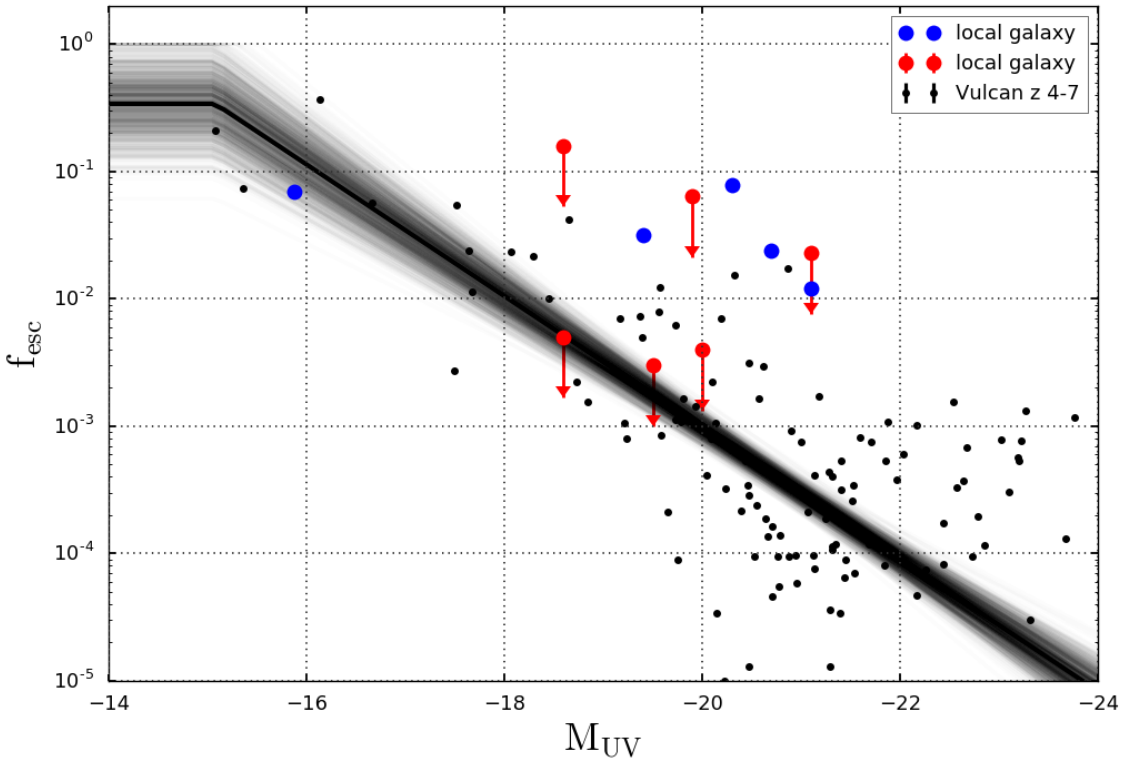

Figure 4.3: Escape fractions of galaxies as a function of their absolute UV magnitudes: **Black points are from our simulation; blue and red points are measurements and upper limits from local galaxies (55, Choi+16 in prep)**. The solid black line represents the best fit line $\log f_{esc} = (0.51 \pm 0.04)M_{UV} + 7.3 \pm 0.8$, and the shaded region shows 1000 samples from the MCMC chain (after the burn in) of the slope and y-intercept from the linear fit. The relationship is capped at the faintest halo that samples the functional fit such that all halos dimmer than $M_{UV} \sim -15$ have an $f_{esc} \sim 35\%$. Fainter, low mass halos tend to have higher escape fractions, and brighter, more massive halos have lower escape fractions. This trend agrees with observations of brighter galaxies having little to no escaping ionizing radiation, and supports the theory that faint, low mass galaxies contribute a significant fraction of the ionizing radiation to reionization.

Here we have fit a power law to the simulated measurements using the maximum likelihood technique, with the equation

$$\log f_{esc} = (0.51 \pm 0.04)M_{UV} + 7.3 \pm 0.8 \tag{4.2}$$

up to a maximum escape fraction of $\sim 35\%$, the maximum f_{esc} that the linear fit is sampled by a measured halo at $M_{UV} \sim -15$. It is difficult to quantify uncertainties in simulations, so here we compute the variance in the relationship via the posterior distribution of the power law fit to the relationship, assuming each individual f_{esc} and M_{UV} value has no error.

This relationship represents *brighter galaxies having little to no escaping ionizing radiation*, and supports the model where *faint, low mass galaxies contribute a significant fraction of their intrinsic ionizing radiation to reionization.* To calculate the total number of ionizing photons in our volume, we integrate down to $M_{UV} \sim -14$ to -15, depending on redshift and completeness level, but not more than a magnitude past the constrained portion of our fit.

4.4 Convergence Test

We used the criteria from (19) to define when a galaxies morphology is resolved and therefore the escape fraction is believable. (19) investigated the resolution sufficient to establish galactic SFRs, SFHs, stellar feedback, and the distribution of gas and stars. They show that there is a minimum number of particles required to create realistic star formation histories (SFH), and a higher threshold for realistic morphologies. Insufficient resolution contributes to the unphysical altering of positions of the particles and the SFR of the galaxy. Correctly determining the amount and location of SF is vital in simulated galaxies because SF produces and distributes metals throughout the galaxy, affects the distribution of matter in the galaxy through feedback, and enables us to relate simulations to observations. In particular, modeling f_{esc} in simulations is sensitive to the SFH and the 3D distribution of gas and stars, or the number of young stars and their positions with respect to neutral hydrogen. (19) found that to properly model the SFH and morphology of a galaxy, a halo must have 10^5 dark matter and 10^5 sph particles. to determine that a galaxy has a realistic 3D distribution of gas and stars, as studied in detail in (19) and discussed previously in

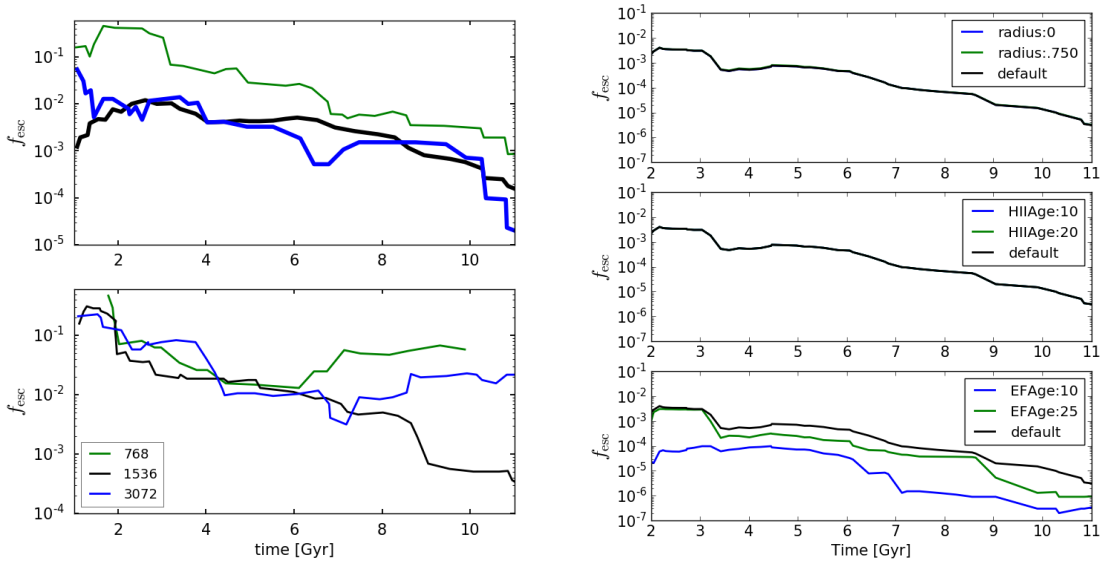

Figure 4.4: LEFT: CONVERGENCE OF $f_{\rm esc}$ The evolving escape fraction, averaged over 10 steps, for a $\sim 10^{11}$ $M_\odot$ halo (top), and it's most massive subhalo (bottom), each ran at 3 resolutions: super-VULCAN (blue), VULCAN (black), and sub-VULCAN (green). The super-VULCAN and VULCAN escape fractions, shown as thicker lines, converge to a similar measurement once both have crossed our resolution threshold at t = 2 Gyr. Here they both have accreted at least 10^5 dark matter particles and 10^5 sph particles. For the subhalo (bottom), the VULCAN and sub-VULCAN simulations never cross our resolution threshold and therefore the measured $f_{\rm esc}$ does not converge. In conclusion, having a strict resolution threshold is important for claiming converged $f_{\rm esc}$ values. RIGHT: $f_{\rm esc}$ PARAMETER TEST: The evolving escape fraction, averaged over 10 steps for a $\sim 10^{11}$ $M_\odot$ halo ran at the VULCAN resolution, varying our parameter choices associated with $f_{\rm esc}$ in each panel. The default parameters are 350 pc HII regions around stellar populations younger than 10 Myr old, and a threshold stellar age of 50 Myrs. Varying parameters associated with the HII regions, their size (top) and age (middle) does not affect $f_{\rm esc}$ significantly. However, varying the stellar age threshold for star particles included in the calculation (bottom) can change $f_{\rm esc}$ by more than an order of magnitude. 10 Myr old stellar populations contribute the most ionizing photons but have very low escape fractions. 25-50 Myr old stellar populations contribute $\sim 10 - 100\times$ fewer ionizing photons, but have $\sim 50\times$ higher $f_{\rm esc}$ making them more potent contributors.

§3.1. Below this limit, the 3D distribution of gas and stars is not accurate and will give erroneous values for $f_{\rm esc}$. This limit is beyond that needed for a realistic SFH, 10^4 dark matter and 10^4 sph particles, so by passing the morphology requirement a galaxy also has a converged SFH.

To show that a resolved morphology leads to a converged $f_{\rm esc}$ measurement, we ran a zoomed in simulation, which creates a sub Milky Way mass galaxy at $z = 0$, at three resolutions: The same as the VULCAN , 8× the resolution of the VULCAN (super-VULCAN), and 1/8 times the resolution of the VULCAN (sub-VULCAN). The super-VULCAN system crosses the resolution threshold at $\sim$ 2 billion years, the VULCAN system crosses at $\sim$ 4 billion years, and the sub-VULCAN system never accreted enough particles to have a resolved morphology. We measure the escape fractions following the same methodology in Section 3.3, including cutting out HII regions around young star particles. The escape fractions are constantly fluctuating, following the stochasticity of the star formation rate, and its subsequent SNe blowing holes in the HI distribution; so for a better comparison of the escape fraction over time, we averaged the escape fraction of the halo over the neighboring 10 steps. For the main halo progenitor, Figure 4.4, left top, after $\sim$ 2-4 billion years, the super-VULCAN and VULCAN escape fractions, shown as the thicker lines, converge on a measurement of the escape fraction, with differences mostly being due to variations in the star formation histories due to stochasticity. The most massive subhalo in the zoomed in simulation also shows that having a strict resolution threshold is important for a converged $f_{\rm esc}$ measurement. For the most massive subhalo Figure 4.4, left bottom, only the super VULCAN simulation reaches our resolution threshold in the age of the universe, after $\sim$ 4 billion years, and the escape fractions do not converge. Also, for the super VULCAN simulation, $f_{\rm esc}$ is higher at higher redshifts, and higher for lower mass systems, in agreement with theory, including our conclusions.

Having a strict resolution threshold of 10^5 dark matter particles and 10^5 sph particles is important for claiming converged results for $f_{\rm esc}$. Our tests show that above this threshold $f_{\rm esc}$ values converge, but below this threshold they do not.

$f_{\rm esc}$ **parameter test:** When we calculate the covering fraction of neutral hydrogen for a halo we chose certain parameters, so here we test if the escape fraction calculation

is sensitive to these choices of parameters using the same VULCAN resolution, zoomed in run for the convergence test. We varied the sizes of the HII regions we cut out around young stars from 0 to 750 pc, the maximum age of an HII region from 10-20 Myrs, and the maximum stellar age that we used in our covering fraction measurement from 10-50 Myrs.

HII Regions: Before we measure the escape fraction we first take the local radiation field of the stars into account and cut out HII regions around stars younger than 10 Myrs old that are 350 pc in size. Increasing the size of the HII region, as well as how long it lives, decreases the amount of neutral hydrogen around young stars, especially in high density regions where many young stars cluster. In high density regions, overlapping HII regions can significantly increase the mean free path of an ionizing photon. However, *our tests show that varying the parameters from the HII regions has very little effect on the escape fraction.* Star particles with low escape fractions live in the very central, dense regions of a galaxy where there is a lot of star formation. Here star particles are fairly clustered and have overlapping HII regions, but they are still deeply embedded in neutral hydrogen. So depleting some neutral hydrogen with the clustered HII regions increases the mean free path of an ionizing photon, but not significantly, and not to the edge of the halo. Here the HII regions are extracting the most neutral gas, but still not bring the escape fraction up significantly for those star particles. For stars that have high escape fractions, they live in lower density regions and tend to be older, greater than 10 Myrs, so they have already dispersed the gas around them to scales larger than the HII regions through SN. In these lower density regions no significant amount of gas is extracted with an HII region, so with or without the HII regions the escape fraction is the same.

Stellar Ages: Our escape fraction measurement is the average sky covering fraction of neutral hydrogen around young stars up to a threshold age. For the paper, we used a threshold age of 50 Myrs. Decreasing the maximum age of the stellar population that is included in the escape fraction calculation decreases the number of stars that are sampled to only the youngest stars. These stars tend to live in denser environments before stellar feedback can disrupt the surrounding gas of the stellar birth cloud. As you increase the threshold age of stars, you increase the sample size but older stars are not contributing as many ionizing photons as their younger counterparts since some of the more massive stars

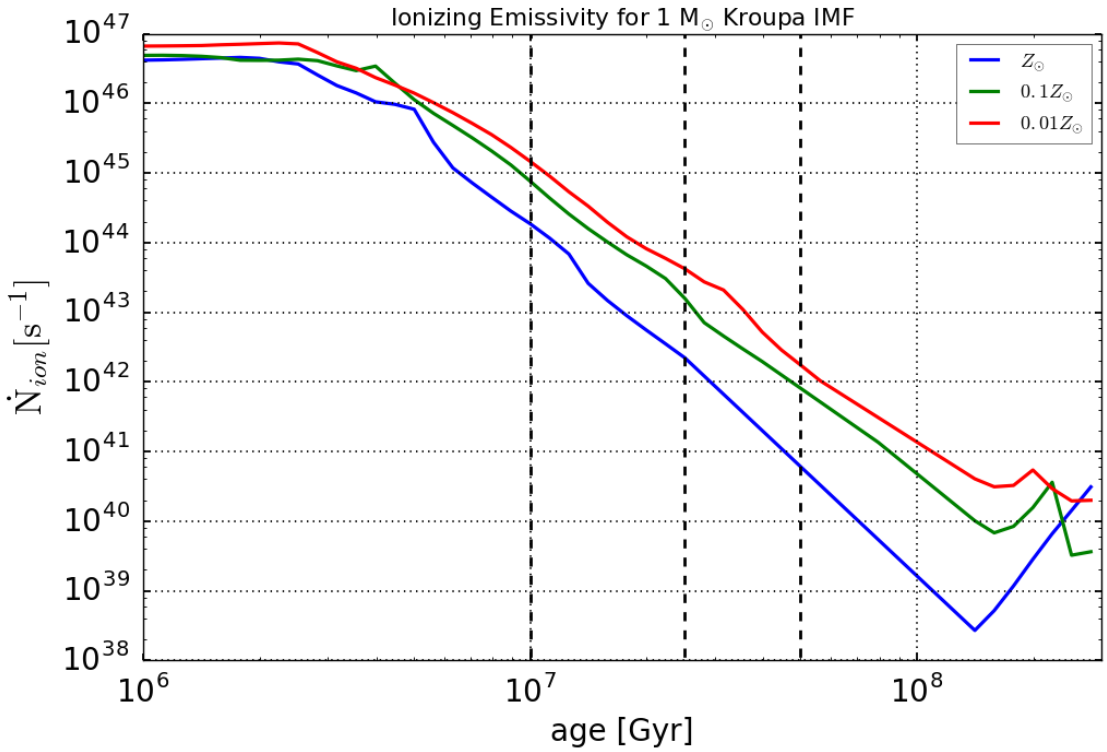

Figure 4.5: **Ionizing emissivity as a function of age** for a stellar population of $1M_\odot$assuming a Kroupa IMF for various metallicities. The ionizing emissivity is initially high when all the stars are still alive, but as time goes on, the most massive stars generating the most ionizing photons die, decreasing the ionizing emissivity of the stellar population. Lower metallicity stellar populations will have higher effective temperatures and therefore have higher emissivities at a given age. The dashed lines represent 10 million years, 25 million years, and 50 million years.

have already turned off the main sequence. Here we tested the change in $f_{\rm esc}$ by varying the threshold age from 10 - 50 Myrs. Using (21) and assuming a Kroupa IMF and a metallicity of $0.01Z_{\odot}$, a 10 Myr stellar population has an ionizing emissivity 10x greater than a 25 Myr stellar population, and 100x greater than a 50 Myr stellar population.

In our test simulation, decreasing the maximum age of a stellar particle included in the escape fraction calculation changes the measured escape fraction by an order of magnitude. Setting the threshold age to 50 Myr or 25 Myr gives similar results at high redshift, but having a strict threshold of 10 Myr drops the measured escape fraction by an order of magnitude. With a threshold of 10 Myrs the calculation is only sampling the stars that are still deeply enveloped by their birth cloud. So they individually have large numbers of ionizing photons but low escape fractions which average out to the halo having a low escape fraction. For this simulation, 25 Myr stellar populations on average have escape fractions that are 25x higher than 10 Myr stellar populations. So although 25 Myr old stellar populations are creating fewer ionizing photons compared with 10 Myr old stellar populations, they have significantly higher escape fractions, and are therefore more potent contributors to the ionizing flux entering the IGM. Their average escape fractions are higher because after 10 Myr SNe feedback is disrupting the birth cloud allowing portions of the sky to have a very small optical depth to ionizing radiation.

Adding HII regions is physically motivated but unnecessary at this resolution. The addition of HII regions, up to 750 pc in size, has a negligible effect on $f_{\rm esc}$. *Dropping the age threshold to 25 Myrs will have a negligible affect on the average measured escape fraction for a halo, but decreasing to 10 Myrs will drop it significantly, and this would exclude some of the more potent contributors to reionization.* So our parameter choices of HII regions that are 350 pc in size for 10 Myrs, and a stellar age threshold of 50 Myrs are well motivated.

Chapter 5

CONSISTENT VIEW OF REIONIZATION

5.1 Results from the Vulcan *Simulation*

The primary uncertainties in the contribution of faint galaxies to reionization are their number densities, quantified by the faint end slope of the luminosity function, and their escape fractions. The number densities of high redshift, low luminosity galaxies are becoming more constrained with deeper surveys that can probe to fainter magnitudes at high redshift. Even though surveys are observing to fainter limits, reionization models must still project the observed luminosity functions to fainter magnitudes than they observe to accumulate enough photons for reionization. So faint galaxies, which may be numerous at high redshift, are difficult to observe, but escape fractions of high redshift galaxies are impossible to observe due to absorption from intergalactic neutral hydrogen between us and the source galaxy. To approach this problem from a theoretical perspective, we use a high resolution, uniform volume simulation to constrain the UVLF to $\sim$ two magnitudes fainter than observations, and use the detailed 3D distribution of gas and stars in resolved high redshift galaxies to calculate $f_{\rm esc}$ as a function of $M_{\rm UV}$. With these findings we now constrain the ionizing emissivity from galaxies during reionization in our simulation, and compare with observed constraints from the lyman alpha forest and cosmic microwave background.

The comoving ionizing emissivity of galaxies in the Vulcan is calculated by integrating the galaxy UVLF, convolved with the conversion from $M_{\rm UV}$ to ionizing emissivity γ_{ion}, and the escape fraction $f_{\rm esc}$ as a function of $M_{\rm UV}$.

$$\dot{N} = \int_{-\infty}^{M_{UV,lim}} dM_{\rm UV} \phi(M_{\rm UV}) \gamma_{ion}(M_{\rm UV}) f_{\rm esc}(M_{\rm UV}) \tag{5.1}$$

where $M_{UV,lim}$ is our 50% completeness limit at a given redshift, varying between $M_{\rm UV} \sim -14$ to -15 depending on redshift. This integral is the ionizing emissivity that escapes galaxy halos and contributes to reionization. The steep slope of the UVLF at the faint

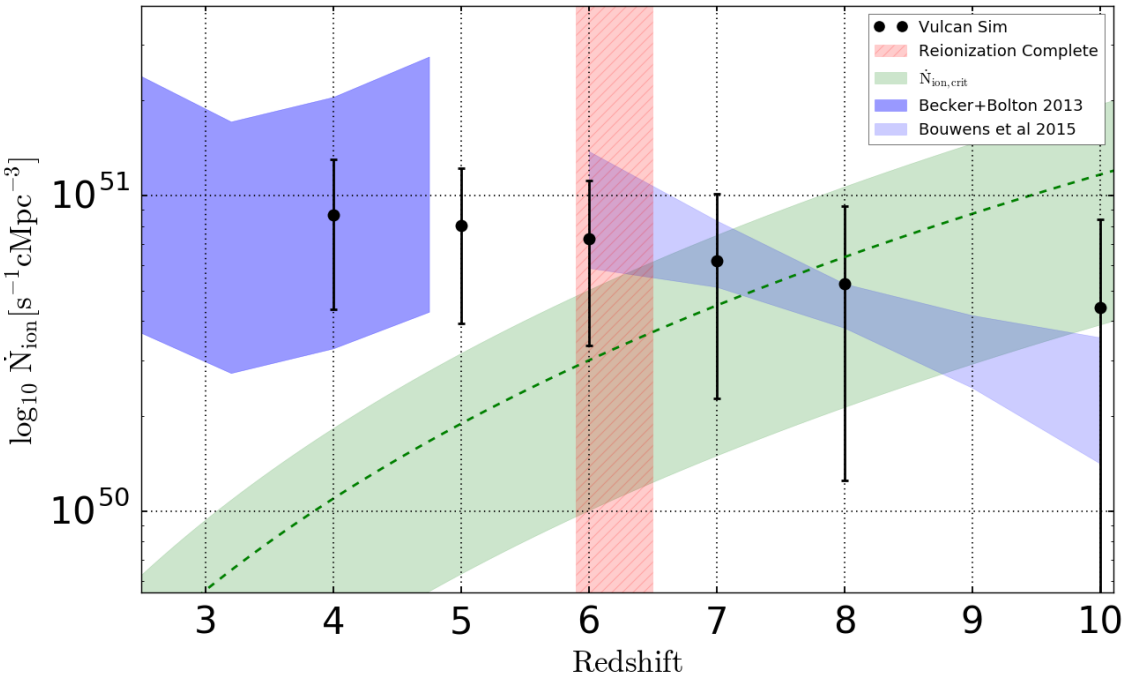

Figure 5.1: Evolution of ionizing emissivity: The black points are the ionizing emissivity calculated by convolving the simulated UVLF with the simulated relationship of $\gamma_{ion}(M_{\rm UV})$ and $f_{\rm esc}(M_{\rm UV})$, and the error bars are the 1σ confidence interval from propagating the simulated distributions for the UVLF parameters and $f_{\rm esc}(M_{\rm UV})$ using a Monte Carlo method. The evolution agrees well with constraints from various observations shown in blue. The red band represents when reionization is complete, and the green band represents the minimum ionizing emissivity required to keep the universe ionized once it has been reionized. The simulated ionizing emissivity agrees with observations, and is above the threshold to keep the universe ionized post reionization. The evolution is very flat because it is dominated by galaxies dimmer than $M_{\rm UV} \sim -17$, whose number density is not evolving significantly, shown both in our simulations and observations. The observed ionizing emissivity can be accounted for during reionization, as well as after up to $z \sim 4$, by our simulated galaxies alone, with high number densities of faint galaxies with high escape fractions.

end convolved with faint galaxies having high escape fractions, $f_{\rm esc} \sim 35\%$, creates a high ionizing emissivity, as shown in Figure 5.1. The black points are from the VULCAN , with the error bars representing the 1σ uncertainties from propagating the uncertainties of the simulated UVLF parameters and $f_{\rm esc}(M_{\rm UV})$ via Monte Carlo sampling of the posteriors.

The comoving ionizing emissivity in the real universe cannot be directly measured, but it can be inferred from various observational measurements of the high redshift universe, shown as the blue regions in Figure 5.1. (4) constrained the ionizing emissivity at $z \sim 2-5$ using measurements of the lyman alpha forest; they combined measurements of the photoionization rate and the mean free path of ionizing photons, shown as the darker blue region. The lighter blue region, from (12), sampled models of the ionizing emissivity and its evolution to determine which models were compatible with various observations: the optical depth to the surface of last scattering from Planck (70), the ionized hydrogen fraction at various redshifts (79), the completion of reionization by z $\sim$ 6 (23), and the inferred ionizing emissivity from (4). The comoving ionizing emissivity of galaxies in the VULCAN , calculated by integrating the galaxy UVLF using equation 5, has large uncertainties but shows excellent agreement with the observationally constrained ionizing emissivity. Our simulated galaxies alone, with a high number density of faint galaxies, and those faint galaxies having high escape fractions, can account for the ionizing emissivity responsible for reionizing the IGM.

Another constraint is that the ionizing emissivity must also keep the universe ionized after reionization. As galaxies spew ionizing radiation into the IGM, reionization continues until $z \sim 5.9-6.5$, when measurements of the Gunn-Peterson optical depth imply that reionization is complete (23), the red hashed region in Figure 5.1. Past this point, once reionization is finished, there is a critical minimum number of ionizing photons required to keep the universe ionized. That is, once the universe is in ionization equilibrium, the ionizing emissivity must balance the recombination rate of the fully ionized IGM given by

$$\dot{N}_{ion}^{crit} = C_{HI}\alpha_A(T_0)n_H(1+Y/4X)(1+z)^3 \tag{5.2}$$

where C_{HI} is the neutral hydrogen clumping factor, α_A is the case A recombination coefficient for hydrogen, and T_0 is the IGM temperature. Given fiducial values, taken from (54),

the critical ionizing emissivity is

$$\dot{N}_{ion}^{crit} = 3 \times 10^{50} s^{-1} cMpc^{-3} \left(\frac{C_{HI}}{3}\right) \left(\frac{T_0}{2 \times 10^4 K}\right)^{-0.7} \left(\frac{1+z}{7}\right)^3 \tag{5.3}$$

This is shown as the green shaded region in Figure 5.1, assuming an IGM temperature of 2×10^4 K, and the width is varying the clumping factor within the uncertainties of 2-5. Early simulations concluded that the clumping factor was high (30), but these early simulations included the clumpiness of neutral hydrogen within halos. The clumpiness within halos is now taken into account using the separate quantity $f_{\rm esc}$, so more recent determinations of the clumping factor in the IGM are lower. More recent simulations have constrained the clumping factor to lie between 1-5 (69; 81; 26), and most groups assume a value of 3. So post reionzation, at $z < 6$, a realistic galaxy ionizing emissivity should be above $\dot{N}_{ion}^{crit}$. Figure 5.1 shows that *our simulated measurements follow the expected evolution of the ionizing emissivity* from (12) and (4), and is above $\dot{N}_{ion,crit}$ at $z > 6.5$, suggesting that *galaxies are the sources that drive the reionization of the universe, with a large number density of faint galaxies that have high* $f_{\rm esc}$.

The evolution of our ionizing emissivity is very flat because it is dominated by faint galaxies at all redshifts, whose number densities are not evolving very much. The faint end slope is becoming shallower with time, but the over all normalization is rising with time, creating a consistent number density of faint galaxies from $z \sim 4 - 10$. This trend is seen in both observations (13) and our simulations. This consistent, high number density of faint galaxies, convolved with their high escape fractions, makes galaxies with $M_{UV} > -17$ dominate the ionizing emissivity, as shown in Figure 5.4, left panel. The left panel of Figure 5.4 shows the fraction of the simulated ionizing emissivity coming from galaxies fainter than $M_{UV} = -17$ as a function of redshift. At $z \sim 10$ they contribute $\sim 99\%$, and at $z \sim 4$ they still contribute $\sim 88\%$. So throughout reionization they are the dominant contributor, but even post reionization they still have a significant contribution to the background ionizing emissivity keeping the IGM ionized. Each faint galaxy individually doesn't have much star formation, but as a population they have a significant budget of escaping ionizing photons.

The evolution of the ionizing emissivity, as well as the expansion of the universe, dictate the evolution of ionized hydrogen during reionization. This is quantified as the volume

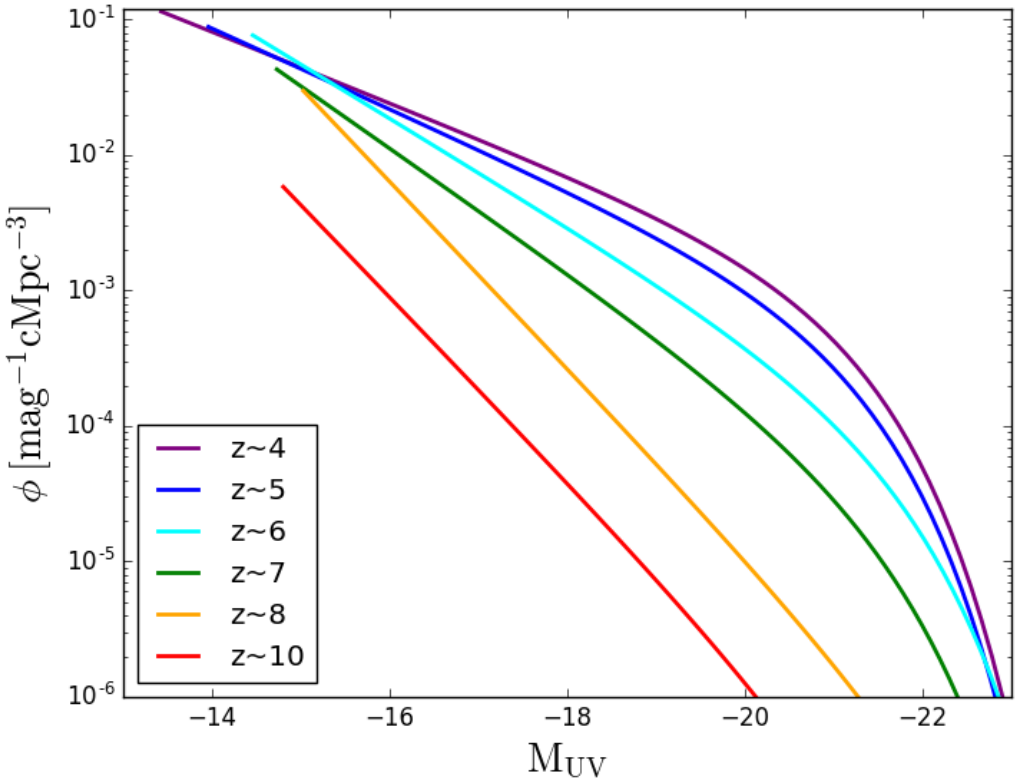

Figure 5.2: **Evolution of the simulated UVLF**: the number densities of faint galaxies $M_{\rm UV} \sim -15$ does not change much with redshift. A similar trend is seen in the observed UVLFs as well (12). The faint end slop is getting shallower with time, but the total number density of galaxies is rising. This creates a number density evolution that is fairly flat for the faint galaxies. Since the ionizing emissivity is dominated by these faint galaxies, and their number densities aren't changing much, the ionizing emissivity doesn't change much either.

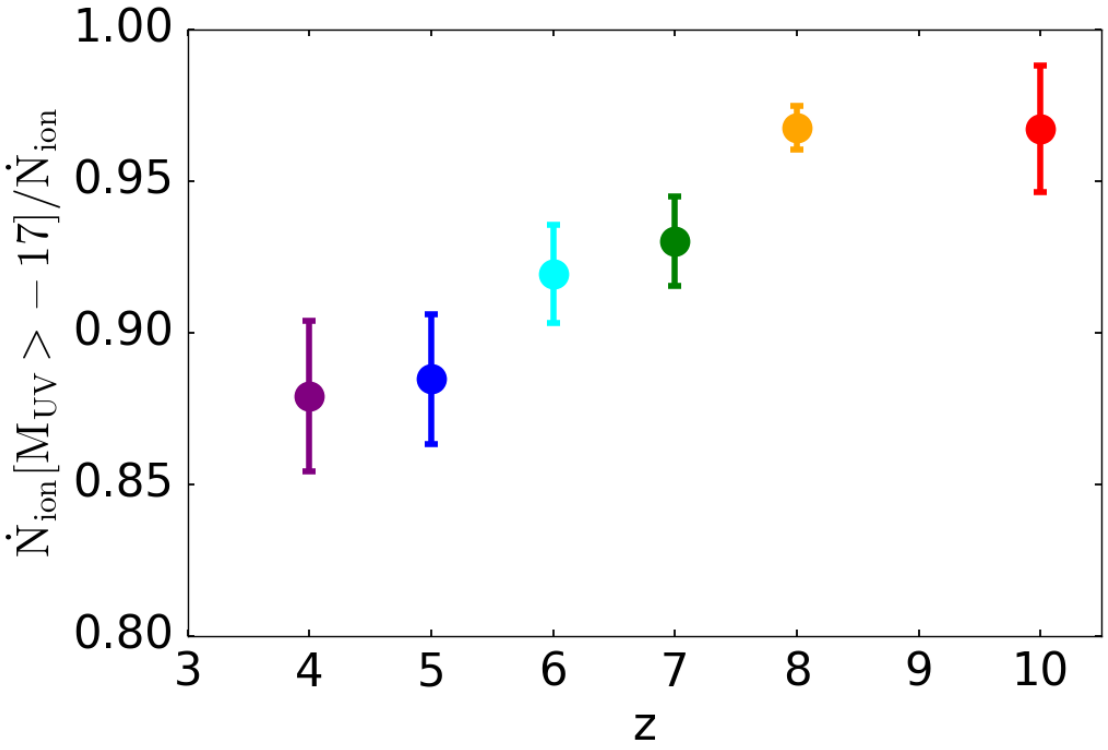

Figure 5.3: Evolution of contribution of faint galaxies to the ionizing emissivity: Faint galaxies, defined as being fainter than $M_{\rm UV} = -17$, the observational limit of HST at high redshifts, dominate the contribution of escaping ionizing photons to the ionizing emissivity. At high redshifts their contribution is 98% and by $z \sim 4$ is still at 88%.

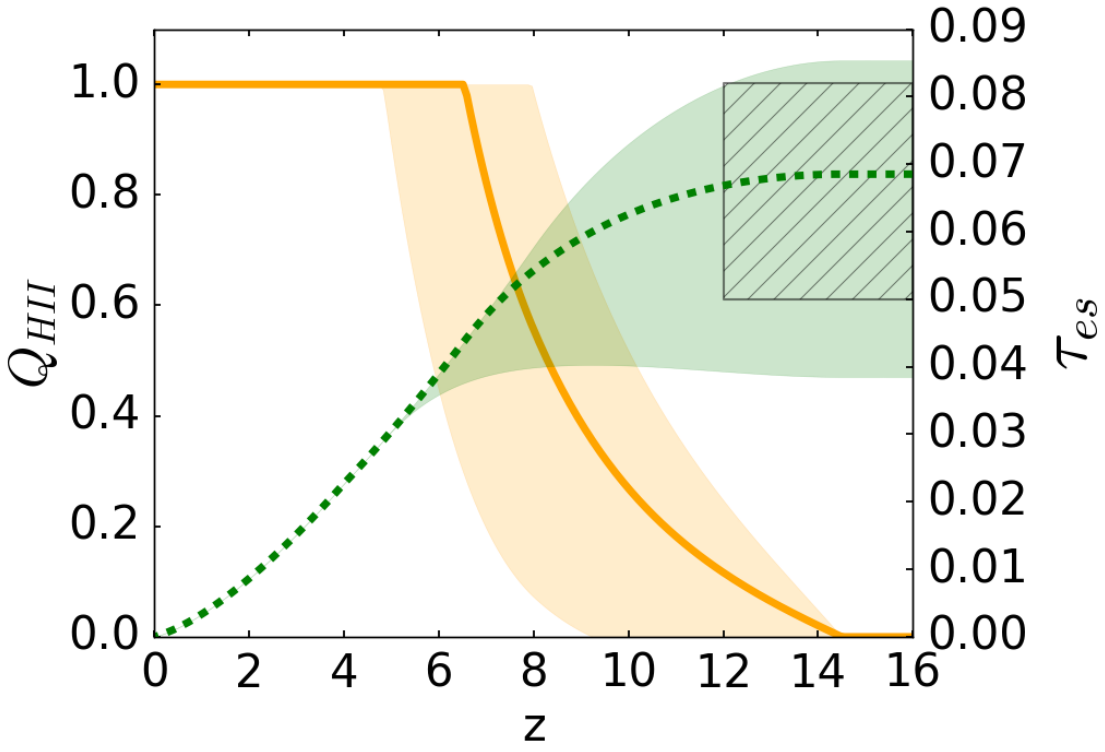

Figure 5.4: Evolution of the fraction of ionized hydrogen from our simulated ionizing emissivity in orange (left axis), and the integrated optical depth to the CMB from this evolution in green (right axis). The error bars for each are the 1σ confidence interval from propagating the ionizing emissivity distribution using a Monte Carlo method. The hatched region represents constraints on the optical depth from (71). Using the ionizing emissivity shown in Figure 5.1, which is dominated by the faint galaxies, we reach 50% ionization at $z \sim 8$, and complete reionization by $z \sim 6.5$. We have a more extended reionization history than that inferred from recent measurements of the UVLF, which increases our optical depth measurement to be in agreement with the most recent CMB measurements.

filling fraction of ionized hydrogen Q_{HII} and it's evolution is constrained by the differential equation

$$\frac{dQ_{HII}}{dt} = \frac{\dot{n}_{ion}}{\bar{n}_H} - \frac{Q_{HII}}{\bar{t}_{rec}}, \tag{5.4}$$

which is the balance of ionizing events and recombination events. Here $\dot{n}_{ion}$ is our measured comoving emissivity from Figure 5.1, $\bar{n}_H$ is the mean comoving hydrogen number density, and $\bar{t}_{rec}$ is the mean recombination rate in the IGM. We linearly interpolate our simulated measurements of the emissivity, and extrapolate to $z \sim 14.5$. Solving this ordinary differential equation, given our evolving emissivity, we get the evolution of Q_{HII} shown in Figure 5.4, right panel. The orange line represents the average history of ionized hydrogen given by the average emissivity measurements, and the shaded regions encapsulate the 1σ uncertainties in the emissivity evolution shown by the error bars in Figure 5.1. The VULCAN is 50% reionized by $z \sim 8$ and completely reionized by $z \sim 6.5$, in excellent agreement with observations of the Lyman alpha forest (23) and the evolving visibility of Lyman alpha emission from galaxies (79). Our reionization is more extended than recent measurements from the UVLF, starting at a redshift of 14.5. We did not measure the UVLF beyond $z \sim 10$, but allowed our emissivity to be extrapolated to $z \sim 14.5$ because our CSFR is flat, as seen in Figure 2.5, right. A flat CSFR implies an equally significant amount of SF is going on from $z \sim 10 - 14.5$, so variations in the ionizing emissivity coming from young stars are minimal.

The other strong observational constraint on reionization is the optical depth to the surface of last scattering. Given $Q_{HII}(z)$, the fraction of ionized hydrogen as a function of redshift, we can calculate the expected optical depth of CMB photons from electron scattering given by the integral

$$\tau_e = \int_0^\infty dz \frac{c(1+z)^2}{H(z)} Q_{HII}(z) \sigma_T \bar{n}_H (1 + \eta(z) Y/4X) \tag{5.5}$$

where σ_T is the Thomson scattering cross section, and η is the ionization state of He, given by 1 for singly ionized and 2 for doubly ionized. We assume that He is singly ionized for $z > 4$ and doubly ionized there after. By integrating Equation 5.5 we get $\tau_{es} = 0.07^{+0.02}_{-0.03}$, shown as the green region in Figure 5.4, right panel, and in excellent agreement with (71), shown as the hatched region representing $\tau_{es} = 0.066 \pm 0.016$. The CMB measurement is a strong constraint, but an integrated quantity, so the agreement validates our integrated

Q_{HII} but not our history of reionization. The optical depth is very sensitive to Q_{HII} at high redshifts, when the physical number densities were much higher. A small number of free electrons at high redshift increases τ_{es} more than an equal number at lower redshifts. So taking SF in the early simulation into account and extrapolating the emissivity out to $z \sim 14.5$, instead of to $z \sim 10$, a difference of ~ 200 Myr, increases τ_{es} by $\sim 20\%$.

Chapter 6

FEEDBACK EFFECTS ON THE CONTRIBUTION OF FAINT GALAXIES TO REIONIZATION

Faint galaxies are a strong contender for the sources that reionized the universe. The star formation histories of faint galaxies, and therefore their production of ionizing photons, is dictated by how efficiently stars are forming in a galaxy. Star formation efficiency in a galaxy is constrained by the amount of available cold, dense gas which can increase via accretion from the cosmic web, or decrease via the creation of stars or stellar feedback driving outflows back into the CGM. Feedback from stars or black holes can also heat the gas which will also decrease star formation rate. At the resolution of our simulation, we do not resolve the formation of individual stars, but instead each star forming event forms a stellar population with a total mass of $6.4 \times 10^4\ M_\odot$. At this resolution, the star formation efficiency is dictated by the subgrid parameters in our simulation. For the VULCAN these parameters were chosen using a unique method which searched parameter space for parameters that could create realistically, present day galaxies, as described in Chapter 2. This parameter search was thorough but still only contained a subsample of galaxies in a particular environment. When we ran the full volume of the VULCAN , containing many different environments, we saw that the most massive galaxies were overproducing stars. An over production of stars in the most massive galaxies is (1) creating unrealistic galaxies and (2) making the high redshift UVLF a power law with no exponential turn over. To alleviate this problem of forming too many stars in the highest mass galaxies, we ran two similar simulations, varying the subgrid parameters. For the first, Romulus, we included blackhole accretion and feedback, and in the second, HighSN, we included more stellar feedback.

By altering the energy deposition for feedback you will alter the star formation histories of the galaxies across all scales, but in a very nonlinear way. The halo mass function for galaxies has a similar shape as the luminosity function, but with deviations at the bright or

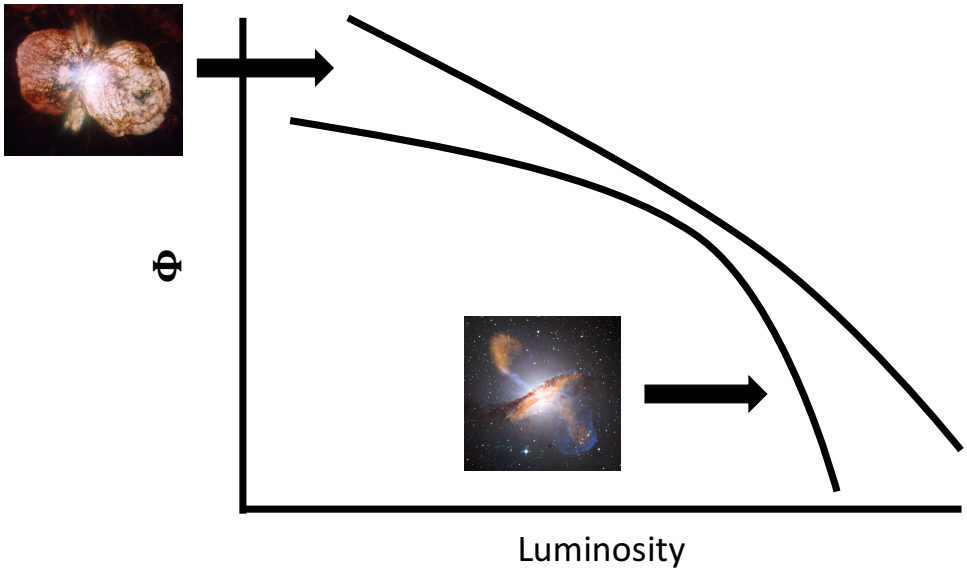

Figure 6.1: **Comparison of the Luminosity Function and Underlying Mass Function:** The underlying halo mass function for galaxies has more high mass halos than luminous halos, and more low mass halos than faint halos. This is interpreted as a decrease in the star formation efficiency at these mass scales. The current theories suggest black hole feedback in the most massive halos, and stellar feedback in low mass halos causes a decrease in the star formation efficiency. By varying these underlying feedback parameters in our simulations we expect a change in the shape of the UVLF.

high mass end, and faint or low mass end, as illustrated in Figure 6.1. There is a deficit of bright halos to populate all the high mass halos, as well as a deficit of faint halos to populate all the low mass halos. This is generally interpreted as the star formation efficiency being lower for these mass scales, such that two similar mass halos can have widely different galaxy luminosities because an evolutionary or environmental effect prevented its gas from turning into stars. At the bright end, this deficit of star formation efficiency is thought to be due to feedback from super massive black holes that formed and evolved with the galaxy. The feedback from their growth is expected to be more effective in higher mass galaxies that presumably have more massive black holes in the center. During the lifetime of a supermassive black hole, it will go through moments where it is accreting gas from the surrounding halo, and in doing so will feed some of the energy from the accreted gas back into the gas in the galaxy, thus heating it up and halting star formation, or driving galactic winds that blow the gas out of the halo. Either way, it is expected to decrease the efficiency of star formation. The deficient star formation at the faint end is thought to be due to feedback from stars, such as supernova or stellar winds. This will also heat the gas and halt star formation, or during a burst of star formation, can also drive galactic winds blowing gas out of the halo. So we expect a variation in the subgrid prescriptions that dictate where stars can form, how much feedback they have on their environment, and including black holes to affect the shape of the UVLF. Specifically, by adding black hole feedback we expect the bright end to have fewer galaxies, and by cranking up the supernova feedback we expect the faint end to have fewer galaxies.

To investigate this theory, we ran two more uniform volume simulations. Romulus, which includes black hole formation and feedback, and HighSN, which includes more feedback from supernova. Romulus also has slightly different star formation parameters, as shown in Table 2.2. The normalization for star formation efficiency is slightly higher, but so is the density threshold required to form a star particle. And once the high mass stars evolve and go supernova, a smaller fraction of the supernova energy is coupled to the gas. In addition to these nonlinear variations, there is also feedback from black holes. Though keep in mind that, at the high redshifts I'm analyzing, the halos in our volume are all relative low mass, and the black holes have not accreted much material or been significantly active. HighSN

maintained the same subgrid parameters as the VULCAN , except for the amount of stellar feedback that couples to the nearby gas. For each supernova event, representing all the stellar feedback from massive stars, twice as much energy couples to the gas.

These variations in the subgrid parameters altered the star formation efficiency in galaxies. For Romulus, the parameter variations are nonlinear and degenerate, but the SMHM comparison in Figure 2.8 shows that Romulus forms galaxies with more stars, at least at these earlier redshifts. The variations for HighSN are a bit more linear, and as expected, Figure 2.8 shows that HighSN forms galaxies with fewer stars compared with the VULCAN . A comparison of the CSFRs, Figure 2.7 shows that the global star formation rate in HighSN is slightly lower than the VULCAN but retains the same shape, and is in broad agreement with observations as well. The CSFRs for Romulus and the VULCAN are broadly similar. So Romulus is slightly more efficient at forming stars, and includes black hold feedback, and HighSN is slightly less efficient at forming stars and includes higher stellar feedback, so how does this affect the UVLF and escape fractions? How does this affect the contribution of faint galaxies to reionization?

6.1 Romulus and HighSN: High z UVLF

To quantify the contribution of faint galaxies to reionization in Romulus and HighSN, I did the same analysis on these two simulations as I did on the VULCAN . For both simulations I calculated the absolute UV magnitudes for all of the galaxies with converged star formation histories. To calculate our completeness, I fit the distribution of UV magnitude and total mass with a KDE. I projected the distribution to lower masses, and populated the distribution with the halo mass function from the simulation. I only included halos that were not dark by putting a threshold of needing at least 8 star particles, a fraction of an SPH kernel, to be included. Even at this threshold, the number of dark halos we have is still high relative to higher resolution simulations (93). If you decrease the number of dark halos to match these higher resolution simulations better, you increase the number of star forming galaxies in the UVLF. So our constraints are a lower limit on the amount of star formation occurring in the faintest galaxy population. We applied the same dust prescription to individual galaxies to dim them and make direct comparisons with observations. We then

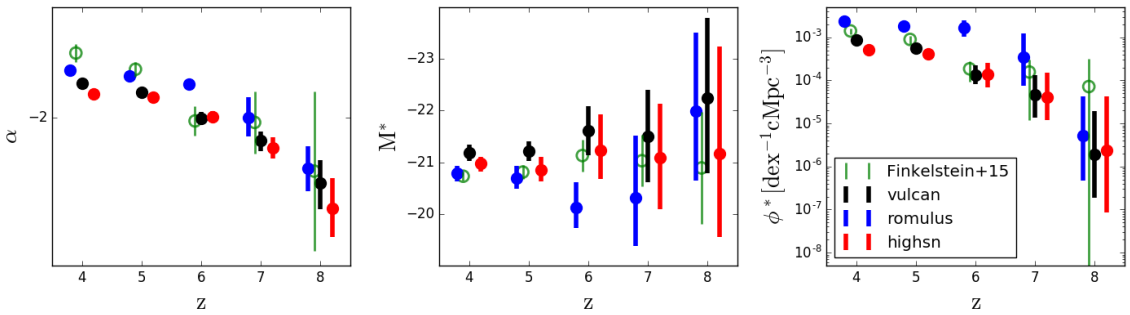

Figure 6.2: **Comparison of the Evolution of the UVLF Shape:** Left is the evolution of the faint end slope α, center is the evolution of the characteristic magnitude M^*, and right is the evolution of the normalization ϕ^*. The black point represent the VULCAN , blue points represent Romulus, red points represent HighSN, and green open circles are observations from (25). A steep faint end slope which gets steeper at higher redshifts is robust to our variations in feedback. The characteristic magnitude is slightly dimmer when raising the stellar feedback or including black holes. In general, however, there is not a significant variation between the volumes.

fit the best fit Schecter function down to $M_{\rm UV} \sim -15$ to make direct comparisons with the VULCAN and observations.

A comparison of the Schecter function parameters and their evolution is shown in Figure 6.2. The Schecter functional fits show that the UVLF measurement is fairly robust to variations in our feedback parameters. In particular, a steep faint end slope that get steeper with redshift, shown in the left hand panel of Figure 6.2, is robust to these variations. We originally thought that increasing supernova feedback might diminish the steepness of the faint end slope, but these faint galaxies are still self regulating and capable of populating the steep halo mass function with a similar number of faint galaxies. Increasing the supernova feedback, as well as including black holes, still gives a steep faint end slope that rises with redshift. The characteristic magnitude is slightly fainter for Romulus and HighSN, shown in the center panel of Figure 6.2, which shows a deficit of brighter galaxies due to the variations in feedback. Still, all the simulated measurements are fairly consistent with observations. It might be that the mass scale at which supernova feedback alters the UVLF is below our resolution limit and therefore also fainter than the observed limits at high redshift. And black holes might become more effective at lower redshifts and show larger variations in the

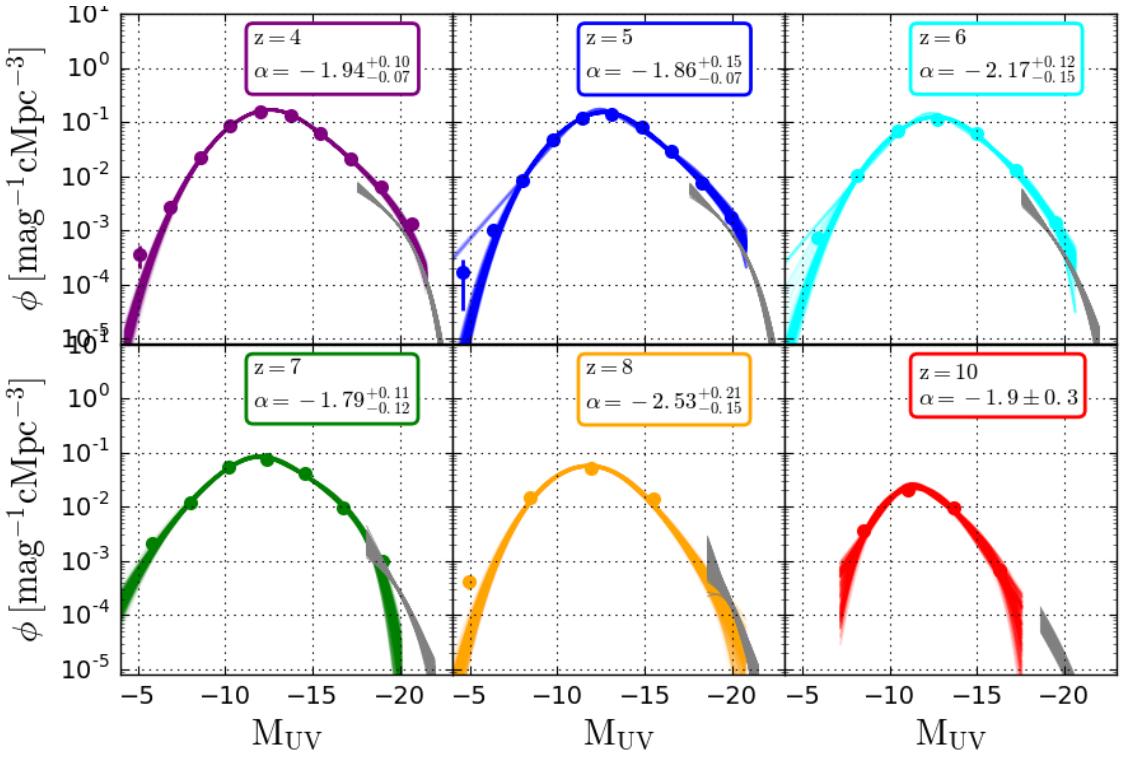

Figure 6.3: **Evolution of UVLF in Romulus:** The histogram of simulated magnitudes is shown as the individual data points, with error bars representing poisson noise from the number of galaxies in the bin. The best fit shechter function to the simulated data is the colored bands. The observed schechter functions from Finkelstein+14 are shown as the grey bands. The redshift and best fit faint end slope are shown in the legend for each subplot. These simulated luminosity functions again show good agreement with observations, especially at higher redshifts. At $z \sim 4$ the UVLF is steeper than the Vulcan due to low mass halos having higher star forming efficiencies.

UVLF when they are closer to their peak activity at $z \sim 2$.

6.1.1 Turn Over in the UVLF

For the Vulcan simulation, integrating the UVLF down to our 50% completeness limit generated enough ionizing photons to reionize the universe. As I show later, the same is not true for Romulus or HighSN. For these simulations we want to include more star formation from the faintest galaxies, and therefore push past our 50% completeness limit. I resisted this previously because, by pushing beyond the 50% completeness limit, results become

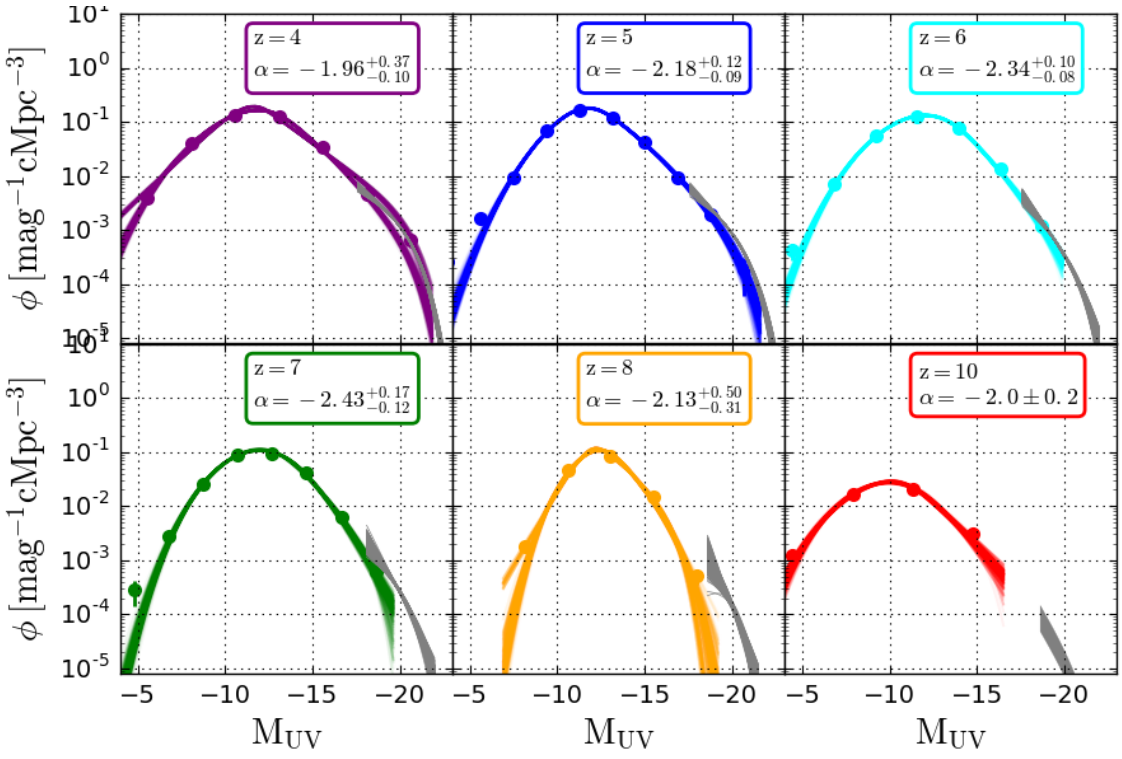

Figure 6.4: **Evolution of UVLF in HighSN:** similar to Figure 6.3 but for HighSN. The histogram of simulated magnitudes is shown as the individual data points, with error bars representing poisson noise from the number of galaxies in the bin. The best fit shechter function to the simulated data is the colored bands. The observed schechter functions from Finkelstein+14 are shown as the grey bands. The redshift and best fit faint end slope are shown in the legend for each subplot. These simulated luminosity functions again show good agreement with observations. It is surprising that raising the stellar feedback for HighSN still produces such steep faint end slopes.

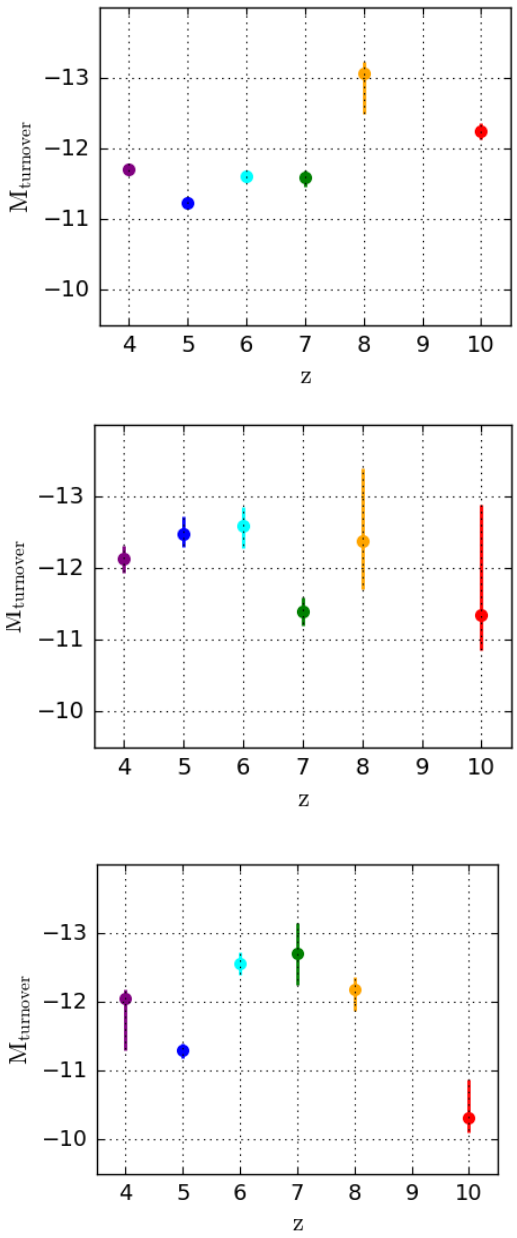

Figure 6.5: **Evolution in the Turn Over in the UVLF:** Fitting the UVLF with the tapered UVLF Equation 6.1, this is the evolution of the $M_{\rm turn}$ parameter, which characterizes the UV magnitude at which star formation becomes inefficient in faint halos so the number densities start to decrease. There is so significant evolution in redshift, or change with feedback variations. $M_{\rm turn}$ lies between ~ -13 to -10. Due to our resolution and completeness, this may just be a bright limit and the true turnover might be fainter.

more uncertain and more dependent on the KDE modeling of my completeness. We push our model past our 50% completeness limit to our 10% completeness limit; past $M_{\rm UV} \sim -15$ to $M_{\rm UV} \sim -10$. By constraining the shape of the UVLF down to $M_{\rm UV} \sim -10$ we resolve the turn over in the UVLF. To fit this different form of the UVLF, we tapered the Schecter Function and used the functional form:

$$\left(\frac{L}{L^*}\right) = 10^{0.4(M^* - M_{\rm UV})} \tag{6.1a}$$

$$\left(\frac{L}{L_{\rm turn}}\right) = 10^{0.4(M_{\rm turn} - M_{\rm UV})} \tag{6.1b}$$

$$\left(\frac{L}{L_{\rm stop}}\right) = 10^{0.4(M_{\rm stop} - M_{\rm UV})} \tag{6.1c}$$

$$dL = 0.4ln(10)\left(\frac{L}{L^*}\right) \tag{6.1d}$$

$$\Phi(M_{\rm UV}) = \Phi^*\left(\frac{L}{L^*}\right)^{\alpha} e^{-\left(\frac{L}{L^*}\right)} dL \tag{6.1e}$$

$$\Phi(M_{\rm UV})_{\rm tapered} = \Phi(M_{\rm UV}) \times (1 - e^{-\left(\frac{L}{L_{\rm turn}}\right)^{\beta}}) \times e^{-\left(\frac{L}{L_{\rm stop}}\right)^{\gamma}} \tag{6.1f}$$

Here I've put it in luminosity space, with the proper conversions to magnitudes, to highlight the functional form. Adding these tapering parameters to the function also changes the shape at the bright end, so comparisons of the resulting Schecter parameters to observations are not as insightful. The one interesting additional shape parameter is the turn over, $M_{\rm turn}$. This represents the UV magnitude at which star formation in galaxies is becoming less efficient, so the number densities of galaxies dimmer than that are tapering off. The evolution of $M_{\rm turn}$ for the Vulcan , Romulus and HighSN are shown in Figure 6.5. $M_{\rm turn}$ lies between -10 and -13. These show no significant evolution with redshift or with feedback prescription. Because we are pushing to our 10% completeness limit, and we over predict the number of dark halos relative to higher resolution simulations, this may be more of a bright limit for the turn over in the UVLF. These values are also consistent with the bright limit from the deepest constraints of the UVLF at $z \sim 6$ from (57).

It is difficult to visualize variations in the UVLF by it's shape, but more interesting variations are seen by integrating the UVLF. Integrating down the UVLF to our 10%

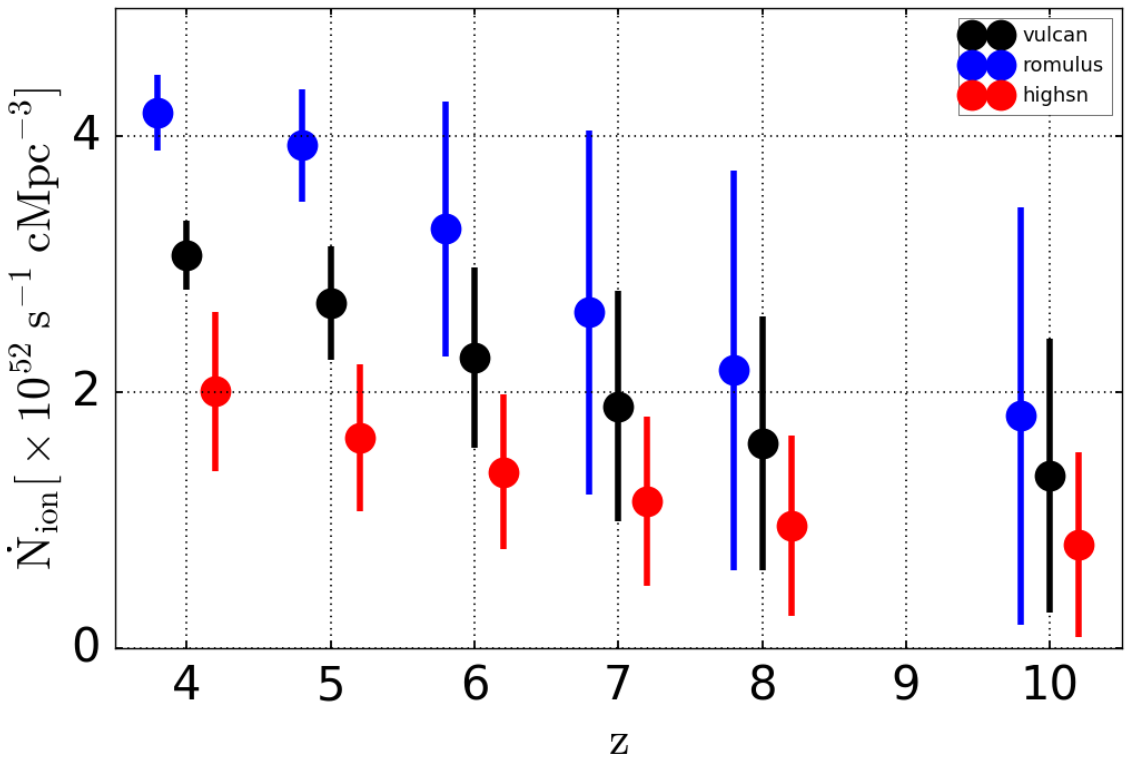

Figure 6.6: **Comparison of the Intrinsic Ionizing Emissivity Evolution** by integrating the UVLF down to $M_{\rm UV} \sim -10$. Black points are the VULCAN , blue points are Romulus, and red points are HighSN. There is a variation of $\sim 50\%$ in the intrinsic ionizing emissivity between the simulations. This is the intrinsic number of ionizing photons being created by the populations of galaxies, so not including $f_{\rm esc}$. Romulus is slightly more efficient at forming stars, and HighSN, as expected, is slightly less efficient at forming stars.

completeness limit, convolved with the conversion from $M_{\rm UV}$ to ionizing emissivity, γ_{ion}, we can get a total ionizing photon production rate as a function of redshift for the three volumes, shown in Figure 6.6. The Schechter function parameters were slightly different but didn't show a noticeable change. Integrating down the UVLF you can see that varying the feedback parameters changes the ionizing production rate by $\sim 50\%$, especially at later times where the results may be diverging. As predicted from the SMHM comparison, the galaxy population in Romulus is slightly more efficient at generating ionizing photons and the galaxy population in HighSN is slightly less efficient at generating ionizing photons.

6.2 Romulus and HighSN: Escape Fractions

Varying the star formation parameters created a population of galaxies with similar UVLF, and showed variations of $\sim 50\%$ in the ionizing photon production rate. However, varying the star formation parameters creates a more drastic difference in the measured escape fractions. For HighSN, raising the supernova feedback decreased the accretion rate of gas onto galaxies as well as drove more gas from the galaxies back into the IGM, out of the halo. This decreases the number of resolution elements in the galaxies, and therefore decreases our sample size of resolved halos at the faint end. The lack of resolved faint halos washed out the relationship we saw in the VULCAN . The resolved halos in HighSN are more massive and, on average, have negligible escape fractions, so the average escape fraction projected to fainter halos is $\sim 0.1\%$, as shown in Figure 6.7. The bright halos in HighSN have similar escape fractions as those in the VULCAN , but a few more bright halos in HighSN scatter to higher escape fractions than we see in the VULCAN , but this does not change the average very much. So larger supernova feedback is increasing the escape fractions for a larger population of brighter galaxies, blowing more holes in the neutral hydrogen distribution, but not enough to change the average escape fraction relationship. Romulus tells a more interesting story.

The inclusion of black holes also washes out the relationship by decreasing the escape fraction for fainter halos and increasing the escape fraction for more of the higher mass halos. This is possibly due to the added dynamics of the gas from the blackhole feedback. In the VULCAN , all of the local gas dynamics in the ISM is dominated by stellar feedback, so

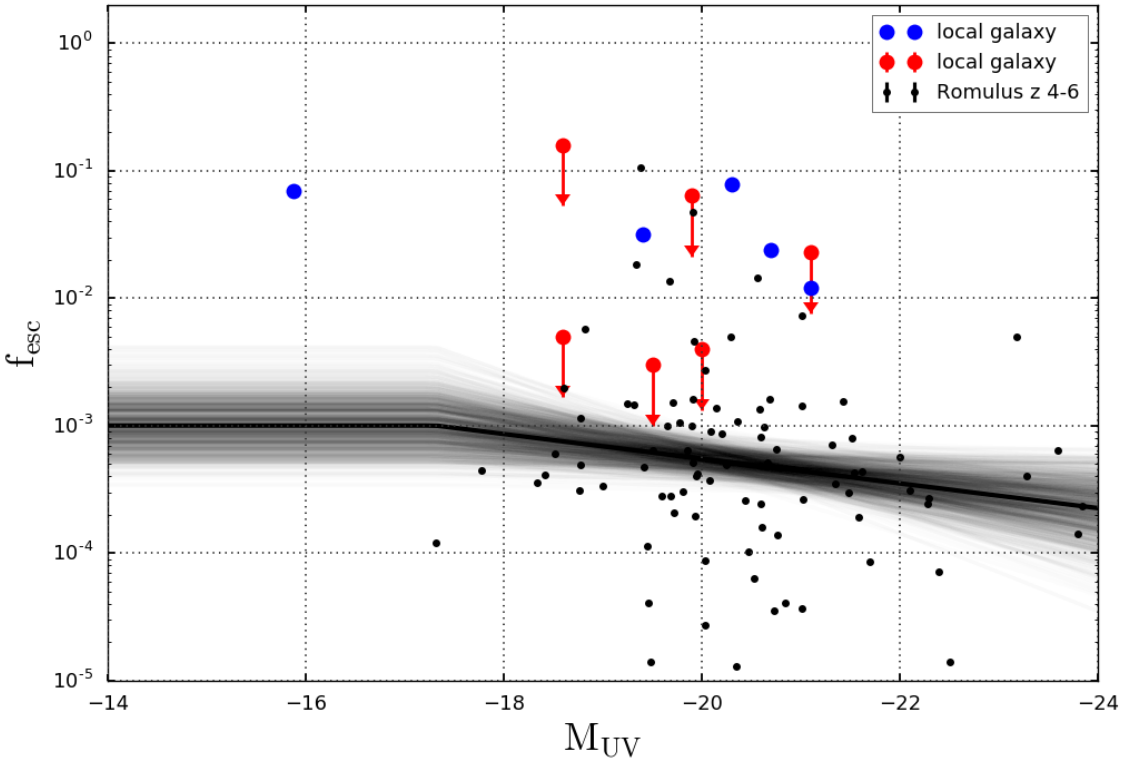

Figure 6.7: **HighSN Escape fractions of galaxies as a function of their absolute UV magnitudes:** Black points are from our simulation; blue and red points are measurements and upper limits from local galaxies (55, Choi+ 16). The solid black line represents the best fit line, and the shaded region shows 1000 samples from the MCMC chain (after the burn in) of the slope and y-intercept from the linear fit. The relationship is capped at the faintest halo that samples the functional fit such that all halos dimmer than $M_{\rm UV} \sim -17$ have an $f_{\rm esc} \sim 0.1\%$. This is significantly lower than the VULCAN . The fainter population of halos in HighSN had slower accretion due to the increase in feedback and therefore higher temperature halo gas. The decreased accretion rates decreased the number of resolution elements in the fainter halos, and pushed them below our resolution threshold. So we do not sample the faint end of the relationship, and therefore all galaxies have very small escape fractions. Similar to Romulus, more of the higher mass halos scatter to higher escape fractions compared with the VULCAN . Higher stellar feed back is playing a role in dynamically moving the gas around more and allowing more of the stellar populations in brighter halos to blister to the surface.

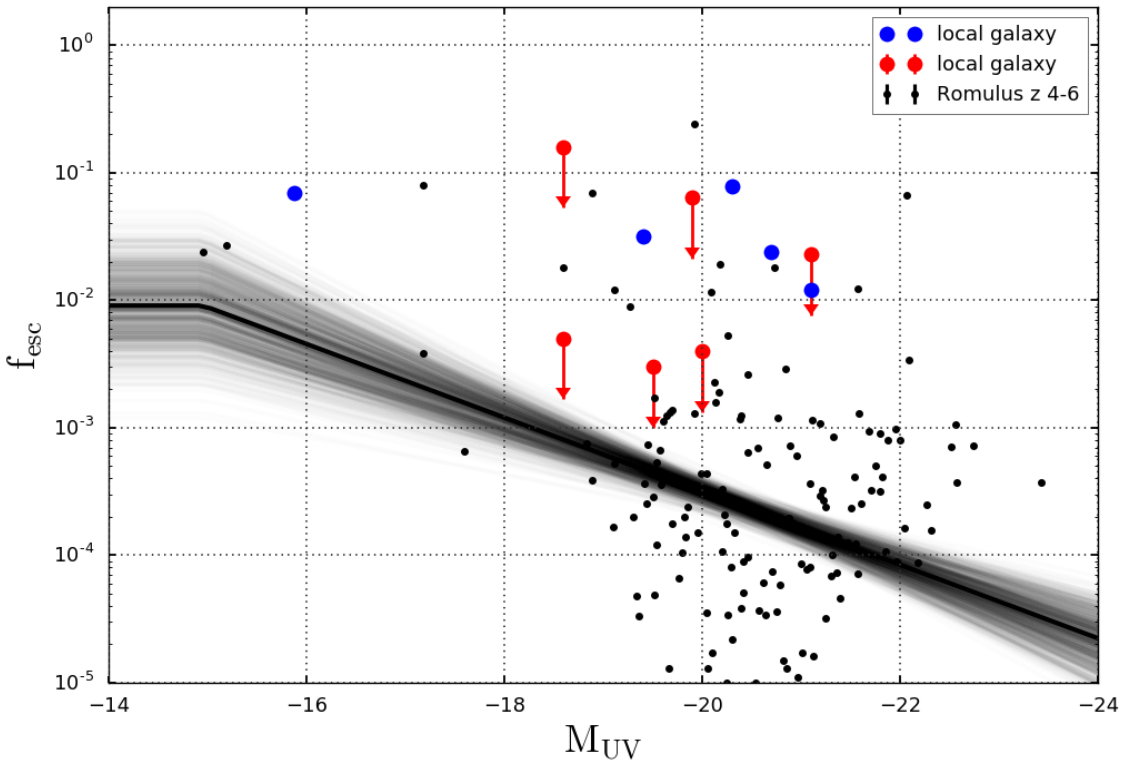

Figure 6.8: **Romulus Escape fractions of galaxies as a function of their absolute UV magnitudes:** Black points are from our simulation; blue and red points are measurements and upper limits from local galaxies (55, Choi+ 16). The solid black line represents the best fit line, and the shaded region shows 1000 samples from the MCMC chain (after the burn in) of the slope and y-intercept from the linear fit. The relationship is capped at the faintest halo that samples the functional fit such that all halos dimmer than $M_{\rm UV} \sim -15$ have an $f_{\rm esc} \sim 1\%$. Fainter, low mass halos tend to have higher escape fractions, and brighter, more massive halos have lower escape fractions. This trend agrees with observations of brighter galaxies having little to no escaping ionizing radiation, and supports the theory that faint, low mass galaxies contribute a significant fraction of the ionizing radiation to reionization. Compared with the VULCAN , fainter halos in Romulus have lower escape fractions, and in general the resolved halos tend to be a bit brighter in the UV due to higher star formation rates. Unlike the Vulcan, some of the brighter galaxies have measurable escape fractions comparable with the observed values. Black hole feed back is playing a role in dynamically moving the gas around allowing more of the stellar populations in brighter halos to blister to the surface, but also covering some of the more dramatic blisters in the faint halos.

bursts of star formation can be correlated with high escape fractions. By stirring up the gas with black hole feedback, now these star formation sites can be enshrouded by neutral gas uncorrelated with a star forming event. So faint halos do not preferentially have high escape fractions. And more higher mass halos have significant escape fractions, again possibly due to black holes stirring up the gas and allowing more stellar populations to blister to the surface.

6.3 Romulus: A Consistent View of Reionization

Similarly to the VULCAN analysis, we convolve the UVLF with the escape fraction relationship to calculate the ionizing emissivity from galaxies over cosmic time. Due to the deficiency of resolved faint halos in the HighSN simulation, and therefore the significant decrease in the escape fractions for faint galaxies, the ionizing emissivity from galaxies in HighSN is too small to be interesting. In Romulus, we also see a decrease in the escape fractions of faint halos, and therefore a decrease in the the resulting ionizing emissivity, shown in Figure 6.9. But Romulus is closer to the observed constraints than HighSN.

In the VULCAN , the average escape fraction for faint galaxies is $\sim 30\%$, in Romulus it is $\sim 1\%$, and for HighSN it is $\sim 0.1\%$. For the VULCAN , we also only integrated down to our 50% completeness limit of $M_{\rm UV} \sim -15$, so there is some underlying star formation in faint halos that was not included and the average ionizing emissivity was a bit high at high redshifts, but with large uncertainties. For Romulus and HighSN, I integrated down to our 10% completeness limit and the average ionizing emissivity was too low. So the escape fraction for faint halos that will reionize the universe at the right rate and time lies somewhere between $\sim 1\% - 30\%$. Given that measurements of the escape fractions of local galaxies lies between $\sim 1\% - 10\%$, this seems like a reasonable expectation of high redshift, little galaxies. Granted, this has to be the average escape fraction, while the systems that have local measurements are those that seem to be going through a star burst, which all faint galaxies will not be experiencing at once.

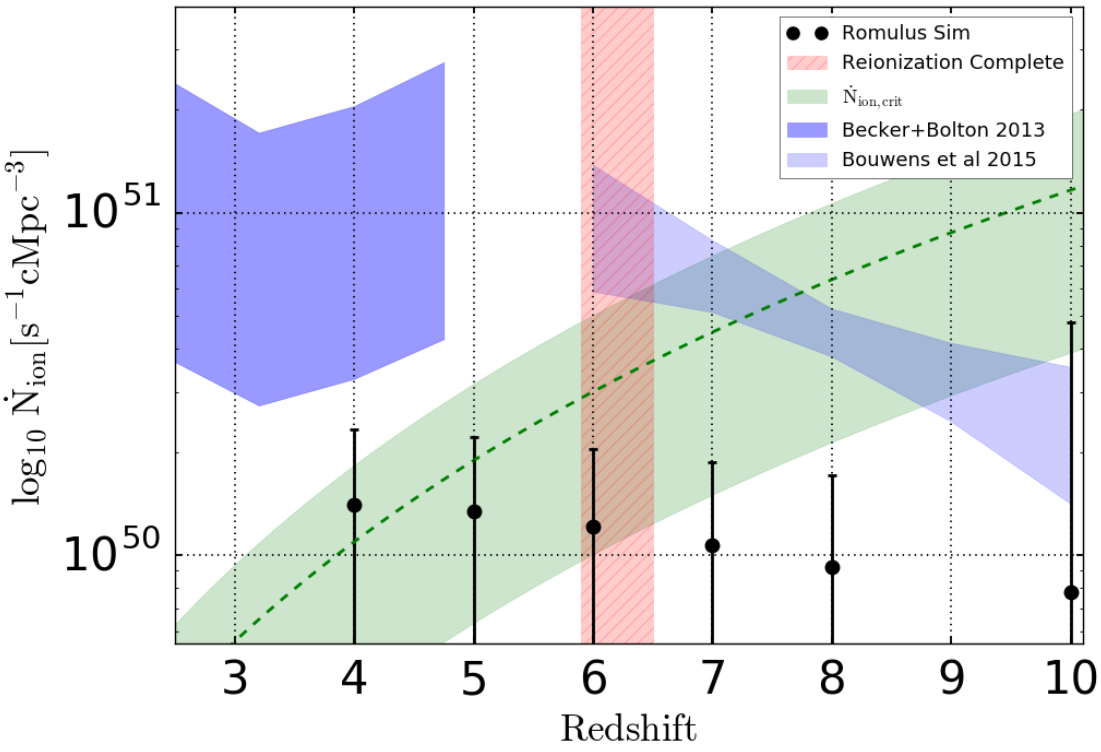

Figure 6.9: **Evolution of the Ionizing Emissivity in Romulus:** The black points are the ionizing emissivity calculated by convolving the simulated UVLF with the simulated relationship of $\gamma_{ion}(M_{\rm UV})$ and $f_{\rm esc}(M_{\rm UV})$, and the error bars are the 1σ confidence interval from propagating the simulated distributions for the UVLF parameters and $f_{\rm esc}(M_{\rm UV})$ using a Monte Carlo method. The ionizing emissivity from Romulus is too low, below the observed constraints. The red band represents when reionization is complete, and the green band represents the minimum ionizing emissivity required to keep the universe ionized once it has been reionized. The simulated ionizing emissivity is low due to the decreased escape fractions for the faint systems. The evolution is very flat because it is dominated by galaxies dimmer than $M_{\rm UV} \sim -17$, whose number density is not evolving significantly, shown both in our simulations and observations. The observed ionizing emissivity can be accounted for during reionization, as well as after up to $z \sim 4$, by our simulated galaxies alone, with high number densities of faint galaxies with high escape fractions.

6.4 Conclusions: Feedback Variations Affecting Contribution of Faint Galaxies to Reionization

The UVLF faint end slope seems to be robust to rather significant variations in the star formation parameters, while escape fractions are more sensitive. Galaxies are efficiently self regulating their star formation across decades in mass allowing the faint end slope to remain steep and get steeper with redshift. The details for understanding how the escape fraction depends on variations in feedback requires a larger population of resolved faint systems. If the escape fraction is fairly low for most galaxies with a shorter lived excursion to higher escape fractions we'll need a larger population of galaxies sampling this noisy distribution. Our relationship for the escape fractions is strongly dependent on the faint halos, of which there are only $\sim$10. In future work, I will measure the escape fractions of lower mass halos at higher resolution. We ran a high resolution zoomed in milky way that has a similar sample size to the VULCAN at high redshift. These are the progenitor, dwarf galaxies that will eventually merge to form the milky way at z=0. These will be UV faint systems with a resolution of 80pc. Compared with the 350pc resolution of the VULCAN , this will allow us to peer into the ISM with more granularity to see how supernova and blackhole feedback is affecting the distribution of neutral hydrogen around star forming regions. We can put better constraints on the escape fractions of faint galaxies.

Chapter 7

CONCLUSIONS

7.1 The Little Galaxies That Could

The sources that reionized the universe are still unknown, but the ionizing photon budget from faint galaxies, below the detection limit of current surveys, may be significant. Observations point to a high number density of faint galaxies at high redshift, and that these faint galaxies, with bursy SFH, may have high escape fractions for ionizing radiation. Here we approached the problem from the theoretical perspective and used a large, uniform volume cosmological simulation, the VULCAN , to constrain the shape of the UVLF and measure $f_{\rm esc}$ for a statistical sample of resolved systems from $z \sim 4-10$. We optimized the subgrid SF parameters to create realistic galaxies at $z = 0$, and are therefore predictive at $z \sim 4-10$, during reionization. The simulation includes a large population of galaxies with realistic SFHs and resolved morphologies, giving us a statistical sample of galaxies to constrain the shape of the UVLF and measure escape fractions. In our simulations, we constrain the shape of the UVLF down to $M_{UV} \sim -15$, two magnitudes fainter than observations, and measure a steeper faint end slope, and therefore a relatively higher number density of faint galaxies, during reionization. This shape and high number density are robust to variations in feedback. Faint galaxies self regulate their star formation at high redshifts even with the inclusion of black holes or twice as much stellar feedback. We test the convergence of our $f_{\rm esc}$ measurements at the resolution of the VULCAN , and measure $f_{\rm esc}$ for the systems passing our strict resolution requirements, down to $M_{\rm UV} \sim -15$. We find a strong correlation of $f_{\rm esc}$ with $M_{\rm UV}$, where bright systems have $f_{\rm esc} < 0.1\%$ and faint systems have $f_{\rm esc} \sim 35\%$. Convolving these findings, we calculate an ionizing emissivity from galaxies that is consistent with observations from $z \sim 4-10$. This simulated emissivity reionizes the universe at the proper rate and completes reionization at $z \sim 6.5$. With this reionization history, the optical depth to the surface of last scattering is $\tau_{es} = 0.07^{+0.02}_{-0.03}$, in excellent

agreement with the most recent Plank results. Therefore, we conclude that faint galaxies as a population, with high number densities and high escape fractions, have the proper ionizing photon budget to reionize the universe in agreement with constraints from observations.

The primary uncertainties in the contribution of faint galaxies to reionization are their number densities, quantified by the faint end slope of the luminosity function, and their escape fractions. The number densities of high redshift, low luminosity galaxies are becoming more constrained with deeper surveys that can probe to fainter magnitudes at high redshift. Even though surveys are observing to fainter limits, reionization models must still project the observed luminosity functions to fainter magnitudes than they observe to accumulate enough photons for reionization. So faint galaxies, which may be numerous at high redshift, are difficult to observe, but escape fractions of high redshift galaxies are impossible to observe due to absorption from intergalactic neutral hydrogen between us and the source galaxy. To approach this problem from a theoretical perspective, we use a high resolution, uniform volume simulation to constrain the UVLF to $\sim$ two magnitudes fainter than observations, and use the detailed 3D distribution of gas and stars in resolved high redshift galaxies to calculate $f_{\rm esc}$ as a function of $M_{\rm UV}$. With these findings we now constrain the ionizing emissivity from galaxies during reionization in our simulation, and compare with observed constraints from the lyman alpha forest and cosmic microwave background.

7.2 Future Work

Having a statistical sample of halos in various environments is important for escape fraction science. Here we used a uniform volume simulation that maximized the box size to diversify the galaxy environments, but also have high enough resolution such that the lower mass systems are resolved. The escape fractions are most intersting for our faintest systems, which is not well populated by our volume. To populate the faint portion of the relationship we ran a high resolution, zoomed in Milky Way simulation. It will have 10x higher resolution than the Vulcan , and the progenitors of the Milky Way will be these faint systems at high redshift. It is this faint part of the relationship that seems more sensitive to feedback variations, so we ran zoomed in simulation varying the feedback as well. This should hopefully shed more light on the escape fractions of faint systems at high redshift, and

whether or not the little galaxies can reionize the universe.

BIBLIOGRAPHY

[1] O. Agertz and A. V. Kravtsov. On the interplay between star formation and feedback in galaxy formation simulations. *ArXiv 1404.2613*, April 2014.

[2] A. Alavi, B. Siana, J. Richard, D. P. Stark, C. Scarlata, H. I. Teplitz, W. R. Freeman, A. Dominguez, M. Rafelski, B. Robertson, and L. Kewley. Ultra-faint Ultraviolet Galaxies at z ˜ 2 behind the Lensing Cluster A1689: The Luminosity Function, Dust Extinction, and Star Formation Rate Density. ApJ, 780:143, January 2014.

[3] M. R. Bate and A. Burkert. Resolution requirements for smoothed particle hydrodynamics calculations with self-gravity. MNRAS, 288:1060–1072, July 1997.

[4] G. D. Becker and J. S. Bolton. New measurements of the ionizing ultraviolet background over 2 ¡ z ¡ 5 and implications for hydrogen reionization. MNRAS, 436:1023–1039, December 2013.

[5] P. S. Behroozi, R. H. Wechsler, and C. Conroy. The Average Star Formation Histories of Galaxies in Dark Matter Halos from z=0-8. *ArXiv e-prints*, July 2012.

[6] P. S. Behroozi, R. H. Wechsler, and C. Conroy. The Average Star Formation Histories of Galaxies in Dark Matter Halos from z = 0-8. ApJ, 770:57, June 2013.

[7] P. S. Behroozi, R. H. Wechsler, and H.-Y. Wu. The ROCKSTAR Phase-space Temporal Halo Finder and the Velocity Offsets of Cluster Cores. ApJ, 762:109, January 2013.

[8] P. S. Behroozi, R. H. Wechsler, H.-Y. Wu, M. T. Busha, A. A. Klypin, and J. R. Primack. Gravitationally Consistent Halo Catalogs and Merger Trees for Precision Cosmology. ApJ, 763:18, January 2013.

[9] A. J. Benson and R. Bower. Galaxy formation spanning cosmic history. MNRAS, 405:1573–1623, July 2010.

[10] J. Bland-Hawthorn and P. R. Maloney. The Escape of Ionizing Photons from the Galaxy. ApJ, 510:L33–L36, January 1999.

[11] J. S. Bolton and M. G. Haehnelt. On the rapid demise of Ly α emitters at redshift z ¿ 7 due to the increasing incidence of optically thick absorption systems. MNRAS, 429:1695–1704, February 2013.

[12] R. J. Bouwens, G. D. Illingworth, P. A. Oesch, J. Caruana, B. Holwerda, R. Smit, and S. Wilkins. Reionization After Planck: The Derived Growth of the Cosmic Ionizing Emissivity Now Matches the Growth of the Galaxy UV Luminosity Density. ApJ, 811:140, October 2015.

[13] R. J. Bouwens, G. D. Illingworth, P. A. Oesch, M. Trenti, I. Labbé, L. Bradley, M. Carollo, P. G. van Dokkum, V. Gonzalez, B. Holwerda, M. Franx, L. Spitler, R. Smit, and D. Magee. UV Luminosity Functions at Redshifts z 4 to z 10: 10,000 Galaxies from HST Legacy Fields. ApJ, 803:34, April 2015.

[14] R. J. Bouwens, G. D. Illingworth, P. A. Oesch, M. Trenti, I. Labbé, M. Franx, M. Stiavelli, C. M. Carollo, P. van Dokkum, and D. Magee. Lower-luminosity Galaxies Could Reionize the Universe: Very Steep Faint-end Slopes to the UV Luminosity Functions at z ¿= 5-8 from the HUDF09 WFC3/IR Observations. ApJ, 752:L5, June 2012.

[15] R. G. Bower, I. Vernon, M. Goldstein, A. J. Benson, C. G. Lacey, C. M. Baugh, S. Cole, and C. S. Frenk. The parameter space of galaxy formation. MNRAS, 407:2017–2045, October 2010.

[16] C. B. Brook, G. Stinson, B. K. Gibson, J. Wadsley, and T. Quinn. MaGICC discs: matching observed galaxy relationships over a wide stellar mass range. MNRAS, 424:1275–1283, August 2012.

[17] A. M. Brooks, A. R. Solomon, F. Governato, J. McCleary, L. A. MacArthur, C. B. A. Brook, P. Jonsson, T. R. Quinn, and J. Wadsley. Interpreting the Evolution of the Size-Luminosity Relation for Disk Galaxies from Redshift 1 to the Present. ApJ, 728:51–+, February 2011.

[18] C. R. Christensen, A. M. Brooks, D. B. Fisher, F. Governato, J. McCleary, T. R. Quinn, S. Shen, and J. Wadsley. Simulating disc galaxy bulges that are consistent with observed scaling relations. MNRAS, 440:L51–L55, May 2014.

[19] C. R. Christensen, T. Quinn, G. Stinson, J. Bellovary, and J. Wadsley. Star Formation and Feedback in Smoothed Particle Hydrodynamic Simulations. II. Resolution Effects. ApJ, 717:121–132, July 2010.

[20] C. Conroy and J. E. Gunn. The Propagation of Uncertainties in Stellar Population Synthesis Modeling. III. Model Calibration, Comparison, and Evaluation. ApJ, 712:833–857, April 2010.

[21] C. Conroy, J. E. Gunn, and M. White. The Propagation of Uncertainties in Stellar Population Synthesis Modeling. I. The Relevance of Uncertain Aspects of Stellar Evolution and the Initial Mass Function to the Derived Physical Properties of Galaxies. ApJ, 699:486–506, July 2009.

[22] D. K. Erb. Feedback in low-mass galaxies in the early Universe. Nature, 523:169–176, July 2015.

[23] X. Fan, V. K. Narayanan, M. A. Strauss, R. L. White, R. H. Becker, L. Pentericci, and H.-W. Rix. Evolution of the Ionizing Background and the Epoch of Reionization from the Spectra of z˜6 Quasars. AJ, 123:1247–1257, March 2002.

[24] A. Ferrara and A. Loeb. Escape fraction of the ionizing radiation from starburst galaxies at high redshifts. MNRAS, 431:2826–2833, May 2013.

[25] S. L. Finkelstein, R. E. Ryan, Jr., C. Papovich, M. Dickinson, M. Song, R. Somerville, H. C. Ferguson, B. Salmon, M. Giavalisco, A. M. Koekemoer, M. L. N. Ashby, P. Behroozi, M. Castellano, J. S. Dunlop, S. M. Faber, G. G. Fazio, A. Fontana, N. A. Grogin, N. Hathi, J. Jaacks, D. D. Kocevski, R. Livermore, R. J. McLure, E. Merlin, B. Mobasher, J. A. Newman, M. Rafelski, V. Tilvi, and S. P. Willner. The Evolution of the Galaxy Rest-Frame Ultraviolet Luminosity Function Over the First Two Billion Years. *ArXiv e-prints*, October 2014.

[26] K. Finlator, S. P. Oh, F. Özel, and R. Davé. Gas clumping in self-consistent reionization models. MNRAS, 427:2464–2479, December 2012.

[27] D. Foreman-Mackey, D. W. Hogg, D. Lang, and J. Goodman. emcee: The MCMC Hammer. PASP, 125:306–312, March 2013.

[28] A. B. Fry, F. Governato, A. Pontzen, T. Quinn, M. Tremmel, L. Anderson, H. Menon, A. M. Brooks, and J. Wadsley. All about baryons: revisiting SIDM predictions at small halo masses. MNRAS, 452:1468–1479, September 2015.

[29] L. Girardi, B. F. Williams, K. M. Gilbert, P. Rosenfield, J. J. Dalcanton, P. Marigo, M. L. Boyer, A. Dolphin, D. R. Weisz, J. Melbourne, K. A. G. Olsen, A. C. Seth, and E. Skillman. The ACS Nearby Galaxy Survey Treasury. IX. Constraining Asymptotic Giant Branch Evolution with Old Metal-poor Galaxies. ApJ, 724:1030–1043, December 2010.

[30] N. Y. Gnedin and J. P. Ostriker. Reionization of the Universe and the Early Production of Metals. ApJ, 486:581–598, September 1997.

[31] F. Governato, C. Brook, L. Mayer, A. Brooks, G. Rhee, J. Wadsley, P. Jonsson, B. Willman, G. Stinson, T. Quinn, and P. Madau. Bulgeless dwarf galaxies and dark matter cores from supernova-driven outflows. Nature, 463:203–206, January 2010.

[32] F. Governato, C. B. Brook, A. M. Brooks, L. Mayer, B. Willman, P. Jonsson, A. M. Stilp, L. Pope, C. Christensen, J. Wadsley, and T. Quinn. Forming a large disc galaxy from a z ¡ 1 major merger. MNRAS, 398:312–320, September 2009.

[33] F. Governato, L. Mayer, J. Wadsley, J. P. Gardner, B. Willman, E. Hayashi, T. Quinn, J. Stadel, and G. Lake. The Formation of a Realistic Disk Galaxy in Λ-dominated Cosmologies. ApJ, 607:688–696, June 2004.

[34] F. Governato, D. Weisz, A. Pontzen, S. Loebman, D. Reed, A. M. Brooks, P. Behroozi, C. Christensen, P. Madau, L. Mayer, S. Shen, M. Walker, T. Quinn, B. W. Keller, and J. Wadsley. Faint dwarfs as a test of DM models: WDM versus CDM. MNRAS, 448:792–803, March 2015.

[35] F. Governato, D. Weisz, A. Pontzen, S. Loebman, D. Reed, A. M. Brooks, P. Behroozi, C. Christensen, P. Madau, L. Mayer, S. Shen, M. Walker, T. Quinn, and J. Wadsley. Faint dwarfs as a test of DM models: WDM vs. CDM. *ArXiv e-prints*, June 2014.

[36] F. Governato, B. Willman, L. Mayer, A. Brooks, G. Stinson, O. Valenzuela, J. Wadsley, and T. Quinn. Forming disc galaxies in ΛCDM simulations. MNRAS, 374:1479–1494, February 2007.

[37] J. P. Grimes, T. Heckman, D. Strickland, W. V. Dixon, K. Sembach, R. Overzier, C. Hoopes, A. Aloisi, and A. Ptak. Feedback in the Local Lyman-break Galaxy Analog Haro 11 as Probed by Far-Ultraviolet and X-Ray Observations. ApJ, 668:891–905, October 2007.

[38] N. A. Grogin, D. D. Kocevski, S. M. Faber, H. C. Ferguson, A. M. Koekemoer, A. G. Riess, V. Acquaviva, D. M. Alexander, O. Almaini, M. L. N. Ashby, M. Barden, E. F. Bell, F. Bournaud, T. M. Brown, K. I. Caputi, S. Casertano, P. Cassata, M. Castellano, P. Challis, R.-R. Chary, E. Cheung, M. Cirasuolo, C. J. Conselice, A. Roshan Cooray, D. J. Croton, E. Daddi, T. Dahlen, R. Davé, D. F. de Mello, A. Dekel, M. Dickinson, T. Dolch, J. L. Donley, J. S. Dunlop, A. A. Dutton, D. Elbaz, G. G. Fazio, A. V. Filippenko, S. L. Finkelstein, A. Fontana, J. P. Gardner, P. M. Garnavich, E. Gawiser, M. Giavalisco, A. Grazian, Y. Guo, N. P. Hathi, B. Häussler, P. F. Hopkins, J.-S. Huang, K.-H. Huang, S. W. Jha, J. S. Kartaltepe, R. P. Kirshner, D. C. Koo, K. Lai, K.-S. Lee, W. Li, J. M. Lotz, R. A. Lucas, P. Madau, P. J. McCarthy, E. J. McGrath, D. H. McIntosh, R. J. McLure, B. Mobasher, L. A. Moustakas, M. Mozena, K. Nandra, J. A. Newman, S.-M. Niemi, K. G. Noeske, C. J. Papovich, L. Pentericci, A. Pope, J. R. Primack, A. Rajan, S. Ravindranath, N. A. Reddy, A. Renzini, H.-W. Rix, A. R. Robaina, S. A. Rodney, D. J. Rosario, P. Rosati, S. Salimbeni, C. Scarlata, B. Siana, L. Simard, J. Smidt, R. S. Somerville, H. Spinrad, A. N. Straughn, L.-G. Strolger, O. Telford, H. I. Teplitz, J. R. Trump, A. van der Wel, C. Villforth, R. H. Wechsler, B. J. Weiner, T. Wiklind, V. Wild, G. Wilson, S. Wuyts, H.-J. Yan, and M. S. Yun.

CANDELS: The Cosmic Assembly Near-infrared Deep Extragalactic Legacy Survey. ApJS, 197:35, December 2011.

[39] Q. Guo, S. White, C. Li, and M. Boylan-Kolchin. How do galaxies populate dark matter haloes? MNRAS, 404:1111–1120, May 2010.

[40] F. Haardt and P. Madau. Radiative Transfer in a Clumpy Universe. IV. New Synthesis Models of the Cosmic UV/X-Ray Background. ApJ, 746:125, February 2012.

[41] T. M. Heckman, K. R. Sembach, G. R. Meurer, C. Leitherer, D. Calzetti, and C. L. Martin. On the Escape of Ionizing Radiation from Starbursts. ApJ, 558:56–62, September 2001.

[42] L. Hernquist and N. Katz. TREESPH - A unification of SPH with the hierarchical tree method. ApJS, 70:419–446, June 1989.

[43] A. M. Hopkins and J. F. Beacom. On the Normalization of the Cosmic Star Formation History. ApJ, 651:142–154, November 2006.

[44] R. M. Hutchings and P. A. Thomas. In-shock cooling in numerical simulations. MNRAS, 319:721–727, December 2000.

[45] Pritish Jetley, Filippo Gioachin, Celso Mendes, Laxmikant V. Kale, and Thomas R. Quinn. Massively parallel cosmological simulations with ChaNGa. In *Proceedings of IEEE International Parallel and Distributed Processing Symposium 2008*, 2008.

[46] S. A. Kassin, A. Brooks, F. Governato, B. J. Weiner, and J. P. Gardner. Kinematic Evolution of Simulated Star-Forming Galaxies. *ArXiv 1406.5187*, June 2014.

[47] N. Katz, D. H. Weinberg, and L. Hernquist. Cosmological Simulations with TreeSPH. ApJS, 105:19–+, July 1996.

[48] G. Kauffmann. Quantitative constraints on starburst cycles in galaxies with stellar masses in the range 10**8-10**10 Msol. *ArXiv 1401.8091*, January 2014.

[49] T. Kaufmann, L. Mayer, J. Wadsley, J. Stadel, and B. Moore. Angular momentum transport and disc morphology in smoothed particle hydrodynamics simulations of galaxy formation. MNRAS, 375:53–67, February 2007.

[50] B. W. Keller, J. Wadsley, S. M. Benincasa, and H. M. P. Couchman. A superbubble feedback model for galaxy simulations. MNRAS, 442:3013–3025, August 2014.

[51] J.-h. Kim, T. Abel, O. Agertz, G. L. Bryan, D. Ceverino, C. Christensen, C. Conroy, A. Dekel, N. Y. Gnedin, N. J. Goldbaum, J. Guedes, O. Hahn, A. Hobbs, P. F. Hopkins, C. B. Hummels, F. Iannuzzi, D. Keres, A. Klypin, A. V. Kravtsov, M. R. Krumholz, M. Kuhlen, S. N. Leitner, P. Madau, L. Mayer, C. E. Moody, K. Nagamine, M. L. Norman, J. Onorbe, B. W. O'Shea, A. Pillepich, J. R. Primack, T. Quinn, J. I. Read, B. E. Robertson, M. Rocha, D. H. Rudd, S. Shen, B. D. Smith, A. S. Szalay, R. Teyssier, R. Thompson, K. Todoroki, M. J. Turk, J. W. Wadsley, J. H. Wise, A. Zolotov, and f. t. AGORA Collaboration29. The AGORA High-resolution Galaxy Simulations Comparison Project. ApJS, 210:14, January 2014.

[52] T. Kimm and R. Cen. Escape Fraction of Ionizing Photons during Reionization: Effects due to Supernova Feedback and Runaway OB Stars. ApJ, 788:121, June 2014.

[53] P. Kroupa. On the variation of the initial mass function. MNRAS, 322:231–246, April 2001.

[54] M. Kuhlen and C.-A. Faucher-Giguère. Concordance models of reionization: implications for faint galaxies and escape fraction evolution. MNRAS, 423:862–876, June 2012.

[55] E. Leitet, N. Bergvall, M. Hayes, S. Linné, and E. Zackrisson. Escape of Lyman continuum radiation from local galaxies. Detection of leakage from the young starburst Tol 1247-232. A&A, 553:A106, May 2013.

[56] C. Leitherer, H. C. Ferguson, T. M. Heckman, and J. D. Lowenthal. The Lyman Continuum in Starburst Galaxies Observed with the Hopkins Ultraviolet Telescope. ApJ, 454:L19, November 1995.

[57] R. C. Livermore, S. L. Finkelstein, and J. M. Lotz. Directly Observing the Galaxies Likely Responsible for Reionization. *ArXiv e-prints*, April 2016.

[58] X. Ma, D. Kasen, P. F. Hopkins, C.-A. Faucher-Giguère, E. Quataert, D. Kereš, and N. Murray. The difficulty of getting high escape fractions of ionizing photons from high-redshift galaxies: a view from the FIRE cosmological simulations. MNRAS, 453:960–975, October 2015.

[59] F. Mannucci, G. Cresci, R. Maiolino, A. Marconi, G. Pastorini, L. Pozzetti, A. Gnerucci, G. Risaliti, R. Schneider, M. Lehnert, and M. Salvati. LSD: Lyman-break galaxies Stellar populations and Dynamics - I. Mass, metallicity and gas at z ˜ 3.1. MNRAS, 398:1915–1931, October 2009.

[60] P. Marigo, L. Girardi, A. Bressan, M. A. T. Groenewegen, L. Silva, and G. L. Granato. Evolution of asymptotic giant branch stars. II. Optical to far-infrared isochrones with improved TP-AGB models. A&A, 482:883–905, May 2008.

[61] L. Mayer, F. Governato, and T. Kaufmann. The formation of disk galaxies in computer simulations. *Advanced Science Letters*, 1:7–27, June 2008.

[62] H. Menon, L. Wesolowski, G. Zheng, P. Jetley, L. Kale, T. Quinn, and F. Governato. Adaptive techniques for clustered N-body cosmological simulations. *Computational Astrophysics and Cosmology*, 2:1, March 2015.

[63] G. R. Meurer, T. M. Heckman, and D. Calzetti. Dust Absorption and the Ultraviolet Luminosity Density at z ˜ 3 as Calibrated by Local Starburst Galaxies. ApJ, 521:64–80, August 1999.

[64] F. Munshi, F. Governato, A. M. Brooks, C. Christensen, S. Shen, S. Loebman, B. Moster, T. Quinn, and J. Wadsley. Reproducing the Stellar Mass/Halo Mass Relation in Simulated ΛCDM Galaxies: Theory versus Observational Estimates. ApJ, 766:56, March 2013.

[65] J. F. Navarro and M. Steinmetz. The Effects of a Photoionizing Ultraviolet Background on the Formation of Disk Galaxies. ApJ, 478:13–+, March 1997.

[66] D. Obreschkow and K. Glazebrook. Fundamental Mass-Spin-Morphology Relation Of Spiral Galaxies. ApJ, 784:26, March 2014.

[67] S.-H. Oh, C. Brook, F. Governato, E. Brinks, L. Mayer, W. J. G. de Blok, A. Brooks, and F. Walter. The Central Slope of Dark Matter Cores in Dwarf Galaxies: Simulations versus THINGS. AJ, 142:24, July 2011.

[68] S.-H. Oh, W. J. G. de Blok, E. Brinks, F. Walter, and R. C. Kennicutt, Jr. Dark and Luminous Matter in THINGS Dwarf Galaxies. AJ, 141:193, June 2011.

[69] A. H. Pawlik, J. Schaye, and E. van Scherpenzeel. Keeping the Universe ionized: photoheating and the clumping factor of the high-redshift intergalactic medium. MNRAS, 394:1812–1824, April 2009.

[70] Planck Collaboration, P. A. R. Ade, N. Aghanim, C. Armitage-Caplan, M. Arnaud, M. Ashdown, F. Atrio-Barandela, J. Aumont, C. Baccigalupi, A. J. Banday, and et al. Planck 2013 results. XVI. Cosmological parameters. *ArXiv e-prints*, March 2013.

[71] Planck Collaboration, P. A. R. Ade, N. Aghanim, M. Arnaud, M. Ashdown, J. Aumont, C. Baccigalupi, A. J. Banday, R. B. Barreiro, J. G. Bartlett, and et al. Planck 2015 results. XIII. Cosmological parameters. *ArXiv e-prints*, February 2015.

[72] A. Pontzen, F. Governato, M. Pettini, C. M. Booth, G. Stinson, J. Wadsley, A. Brooks, T. Quinn, and M. Haehnelt. Damped Lyman α systems in galaxy formation simulations. MNRAS, 390:1349–1371, November 2008.

[73] A. Pontzen, R. Roskar, G. Stinson, and R. Woods. pynbody: N-Body/SPH analysis for python, May 2013. Astrophysics Source Code Library.

[74] Thomas R. Quinn, Pritish Jetley, Laxmikant V. Kale, and Filippo Gioachin. N - body Simulations with ChaNGa. In Laxmikant V. Kale and Bhatele Abhinav, editors, *Parallel Science and Engineering Applications: The Charm++ Approach*. Taylor & Francis Group, CRC Press, November 2013.

[75] N. A. Reddy and C. C. Steidel. A Steep Faint-End Slope of the UV Luminosity Function at z ˜ 2-3: Implications for the Global Stellar Mass Density and Star Formation in Low-Mass Halos. ApJ, 692:778–803, February 2009.

[76] B. W. Ritchie and P. A. Thomas. Multiphase smoothed-particle hydrodynamics. MNRAS, 323:743–756, May 2001.

[77] J. Schaye, R. A. Crain, R. G. Bower, M. Furlong, M. Schaller, T. Theuns, C. Dalla Vecchia, C. S. Frenk, I. G. McCarthy, J. C. Helly, A. Jenkins, Y. M. Rosas-Guevara, S. D. M. White, M. Baes, C. M. Booth, P. Camps, J. F. Navarro, Y. Qu, A. Rahmati, T. Sawala, P. A. Thomas, and J. Trayford. The EAGLE project: Simulating the evolution and assembly of galaxies and their environments. *ArXiv e-prints*, July 2014.

[78] P. Schechter. An analytic expression for the luminosity function for galaxies. ApJ, 203:297–306, January 1976.

[79] M. A. Schenker, R. S. Ellis, N. P. Konidaris, and D. P. Stark. Line-emitting Galaxies beyond a Redshift of 7: An Improved Method for Estimating the Evolving Neutrality of the Intergalactic Medium. ApJ, 795:20, November 2014.

[80] S. Shen, J. Wadsley, and G. Stinson. The enrichment of the intergalactic medium with adiabatic feedback - I. Metal cooling and metal diffusion. MNRAS, 407:1581–1596, September 2010.

[81] J. M. Shull, B. D. Smith, and C. W. Danforth. The Baryon Census in a Multiphase Intergalactic Medium: 30% of the Baryons May Still be Missing. ApJ, 759:23, November 2012.

[82] R. Smit, R. J. Bouwens, M. Franx, G. D. Illingworth, I. Labbé, P. A. Oesch, and P. G. van Dokkum. The Star Formation Rate Function for Redshift z ˜ 4-7 Galaxies: Evidence for a Uniform Buildup of Star-forming Galaxies during the First 3 Gyr of Cosmic Time. ApJ, 756:14, September 2012.

[83] V. Springel and L. Hernquist. Cosmological smoothed particle hydrodynamics simulations: the entropy equation. MNRAS, 333:649–664, July 2002.

[84] J. Stadel. PhD Thesis: Cosmological N-Body Simulations and their Analysis. In *PhD Thesis: Cosmological N-Body Simulations and their Analysis*, 2001.

[85] G. Stinson, A. Seth, N. Katz, J. Wadsley, F. Governato, and T. Quinn. Star formation and feedback in smoothed particle hydrodynamic simulations - I. Isolated galaxies. MNRAS, 373:1074–1090, December 2006.

[86] B. Strömgren. The Physical State of Interstellar Hydrogen. ApJ, 89:526, May 1939.

[87] E. Tolstoy, V. Hill, and M. Tosi. Star-Formation Histories, Abundances, and Kinematics of Dwarf Galaxies in the Local Group. *ARAA*, 47:371–425, September 2009.

[88] A. van der Wel, A. N. Straughn, H.-W. Rix, S. L. Finkelstein, A. M. Koekemoer, B. J. Weiner, S. Wuyts, E. F. Bell, S. M. Faber, J. R. Trump, D. C. Koo, H. C. Ferguson, C. Scarlata, N. P. Hathi, J. S. Dunlop, J. A. Newman, M. Dickinson, K. Jahnke, B. W. Salmon, D. F. de Mello, D. D. Kocevski, K. Lai, N. A. Grogin, S. A. Rodney, Y. Guo, E. J. McGrath, K.-S. Lee, G. Barro, K.-H. Huang, A. G. Riess, M. L. N. Ashby, and S. P. Willner. Extreme Emission-line Galaxies in CANDELS: Broadband-selected, Starbursting Dwarf Galaxies at z ¡ 1. ApJ, 742:111, December 2011.

[89] M. Vogelsberger, S. Genel, V. Springel, P. Torrey, D. Sijacki, D. Xu, G. F. Snyder, D. Nelson, and L. Hernquist. Introducing the Illustris Project: Simulating the coevolution of dark and visible matter in the Universe. *ArXiv e-prints*, May 2014.

[90] J. W. Wadsley, J. Stadel, and T. Quinn. Gasoline: a flexible, parallel implementation of TreeSPH. *New Astronomy*, 9:137–158, February 2004.

[91] D. R. Weisz, A. E. Dolphin, E. D. Skillman, J. Holtzman, K. M. Gilbert, J. J. Dalcanton, and B. F. Williams. The Star Formation Histories of Local Group Dwarf Galaxies II. Searching For Signatures of Reionization. *ArXiv 1405.3281*, May 2014.

[92] J. H. Wise, T. Abel, M. J. Turk, M. L. Norman, and B. D. Smith. The birth of a galaxy - II. The role of radiation pressure. MNRAS, 427:311–326, November 2012.

[93] J. H. Wise and R. Cen. Ionizing Photon Escape Fractions From High-Redshift Dwarf Galaxies. ApJ, 693:984–999, March 2009.

[94] B. Yue, A. Ferrara, E. Vanzella, and R. Salvaterra. Ultra-faint high-redshift galaxies in the Frontier Fields. MNRAS, 443:L20–L24, September 2014.

VITA

Lauren Anderson was born and raised in Ontario, California. She attended University of California, Berkeley where she received a Bachelor of Arts degree in Physics and Astronomy in 2008. After working as a post-baccalaureate researcher at the Lawrence Berkeley National Laboratory in Berkeley, California, Lauren moved to Seattle in 2009 to begin her graduate studies in the Astronomy department at the University of Washington. She completed his Masters of Science degree in 2010, and completed her doctorate in 2016.